Neutron-Induced Partial Gamma-Ray Cross-Section Measurements on Uranium

by

Anthony Lloyd Hutcheson

Department of Physics
Duke University

Date: _____

Approved:

_____
Werner Tornow, Supervisor

_____
Calvin R. Howell

_____
Richard G. Palmer

_____
Anton P. Tonchev

_____
Ying K. Wu

Dissertation submitted in partial fulfillment of the
requirements for the degree of Doctor of Philosophy
in the Department of Physics
in the Graduate School of
Duke University

2008

ABSTRACT

Neutron-Induced Partial Gamma-Ray Cross-Section Measurements on Uranium

by

Anthony Lloyd Hutcheson

Department of Physics
Duke University

Date: _____

Approved:

_____
Werner Tornow, Supervisor

_____
Calvin R. Howell

_____
Richard G. Palmer

_____
Anton P. Tonchev

_____
Ying K. Wu

An abstract of a dissertation submitted in partial fulfillment of the requirements for the degree of Doctor of Philosophy in the Department of Physics in the Graduate School of Duke University

2008

Abstract

Precision measurements of ^{238}U$(n, n'\gamma)$ and ^{235,238}U$(n, 2n\gamma)$ partial cross sections have been performed at Triangle Universities Nuclear Laboratory (TUNL) to improve crucial data for the National Nuclear Security Administration's (NNSA) Stockpile Stewardship Program. Accurate neutron-induced reaction cross-section data are required for many practical applications, including nuclear energy and reactor technology, nuclear transmutation, and explosive nuclear devices. Due to the cessation of underground nuclear testing in the early 1990s, understanding of the performance of nuclear devices is increasingly dependent on precise model calculations which are, in turn, themselves reliant on accurate reaction data to serve as benchmarks for model codes. Direct measurement of (n, n') and $(n, 2n)$ reaction cross sections for uranium is extremely difficult due to large neutron background from fission and very close nuclear level spacing. Previous direct measurements of the cross sections are incomplete and/or discrepant over the energy range of interest. However, the $(n, n'\gamma)$ and $(n, 2n\gamma)$ partial γ-ray cross-section data obtained in the present work can be combined with model calculations to infer total (n, n') and $(n, 2n)$ reaction-channel cross sections.

A pulsed and monoenergetic neutron beam was used in combination with high-resolution γ-ray spectroscopy to measure these partial cross sections for incident neutron energies between 5 and 14 MeV. Gamma-ray yields were measured with high-purity germanium (HPGe) clover and planar detectors. Neutron fluxes were determined from the well-measured $2^+ \rightarrow 0^+$ transition in ^{56}Fe to be on the order of 10^4 n$\cdot$cm$^{-2}\cdot$s^{-1}. Detector efficiency and attenuation of γ rays in the target were simulated using the MCNPX Monte-Carlo radiation transport code.

Measured partial cross sections were compared with previous measurements and

calculations from GNASH and TALYS Hauser-Feshbach statistical-model codes. Results are generally in good agreement with existing data and provide cross-section data for transitions in energy regions where none previously existed. Total reaction-channel cross sections are inferred from statistical-model calculations and compared with existing direct measurement data.

Contents

List of Figures

List of Tables

Acknowledgements

This dissertation would not have been possible without the help of many people. First and foremost, I am indebted to my advisor, Dr. Werner Tornow, for his guidence and support through these past few years of study. He exemplifies the model of a responsible, successful researcher, and I am grateful to him for giving me the opportunity to learn from him. I would also like to express my gratitude to Dr. Anton Tonchev for the time and patience spent mentoring me on the various aspects of the discipline and for having an open door when I had yet another random question. I am grateful to the other members of my committee, Drs. Calvin Howell, Richard Palmer, and Ying Wu, for agreeing to serve on my thesis committee.

I have been priviledged to work with a number of skilled and knowledgeable researchers as a part of the NNSA group at TUNL. I would like to thank Dr. John Kelley for hours spent explaining the various aspects of our electronics, data acquisition system, and data analysis. I am grateful to Dr. Hugon Karwowski for innumerable helpful comments and discussions to help a young scientist find his path. I am thankful to Dr. Calvin Howell for maintaining TUNL as a fantastic research environment in his role as laboratory director and for his help understanding the beam pulsing system. I would also like to thank Dr. Alex Crowell for his aid when I inevitably had a problem with a computer code or script.

I am thankful for the opportunity to work with a number of collaborators from different universities and national laboratories as part of my study. In particular, I'd like to thank my collaborators at Los Alamos National Laboratory, Drs. Nik Fotiades and Ron Nelson, and at Lawrence Livermore National Laboratory, Drs. John Becker, Rob Macri, and Dugersuren Dashdorj, for their help and guidence throughout this study. I would like to thank Drs. Ron Pedroni and Gary Weisel for time spent

covering shifts in the lab and giving me a chance to sleep once in a while. I am indebted to Dr. Toshihiko Kawano at LANL and Paul Garrett at the University of Guelph for their help with theoretical modeling.

I would like to thank the TUNL technical and support staff, Richard O'Quinn, John Dunham, Paul Carter, Brett Carlin and Patrick Mulkey. Without their knowledge and hard work, this research would have never made it off the ground. I am also eternally grateful to Donna Ruger, the unofficial "den mother" of physics graduate students at Duke, for being there to help with all the little problems that inevitably crop up.

I am thankful to Dr. Elaine Kwan, Samantha Hammond, and Chris Angell for their friendship during my time here. The odd coffee break and lunchtime discussion did wonders to maintain my sanity. I am grateful to my officemate, Mary Kidd, for the short conversation here and there that made my day a bit more pleasant. I would also like to thank my support system of friends outside of work: Patty, Alyssa, Heather, Katie, Beth, Meg, Stacey, and Anne. You each brightened even the particularly hard days, and I am eternally thankful for it.

I am forever grateful to my family for their love and support thoughout this journey. I would like to thank my parents, Tony and Janet Hutcheson, for their steadfast support and encouragement my entire life and for helping cultivate in me a spirit of curiousity. I thank my siblings, Trudie and Jarrod, for keeping my ego in check when needed and for lifting my spirits when that was needed, too. I am grateful to my children, Zoe and Maeve, who I firmly believe to be my greatest contribution to this world, for their unconditional love and for making me a better person. Lastly, I am forever indebted to my wife, Mary, for her love, patience, and support through these years. Words are insufficient to express my love and gratitude. You make my life complete.

Finally, I thank God for all the blessings listed above, for creating a universe worth studying, and give us the ability to do so. Life would be rather boring otherwise.

Chapter 1

Introduction

The research described in this dissertation entails the measurement of partial cross sections for $(n, n'\gamma)$ and $(n, 2n\gamma)$ reactions on ^{235,238}U using the pulsed and monoenergetic neutron beam at Triangle Universities Nuclear Laboratory. As opposed to the total reaction cross section, which is proportional to the probability of any interaction in a given reaction channel to take place, a partial cross section measures the probability for a specific interaction between two discrete nuclear levels. The goals of these measurements are to produce accurate cross sections that are of importance both for radiochemical diagnostic purposes and for benchmarking nuclear reaction models and to demonstrate the effectiveness of using high-resolution γ-ray spectroscopy coupled with theoretical modeling to determine neutron inelastic scattering cross sections for actinides where direct measurement proves to be difficult. These measurements are of added interest because previous measurements of the total reaction cross sections were confined to narrow neutron energy ranges, are few in number, and/or are inconsistent over particular energy ranges. The current status of total reaction cross-section data for ^{238}U(n, n') and ^{235,238}U$(n, 2n)$ is depicted in Figures 1.1, 1.2, and 1.3.

The remainder of this chapter will flesh out the motivation for these measurements. Chapter 2 describes the theoretical considerations for nuclear reactions, and a brief outline of the model calculations utilized is given in Chapter 3. Chapter 4 addresses the experimental setup and techniques used in these measurements while Chapter 5 details the steps taken to analyze the data obtained during these measurements. Experimental results are presented in Chapter 6.

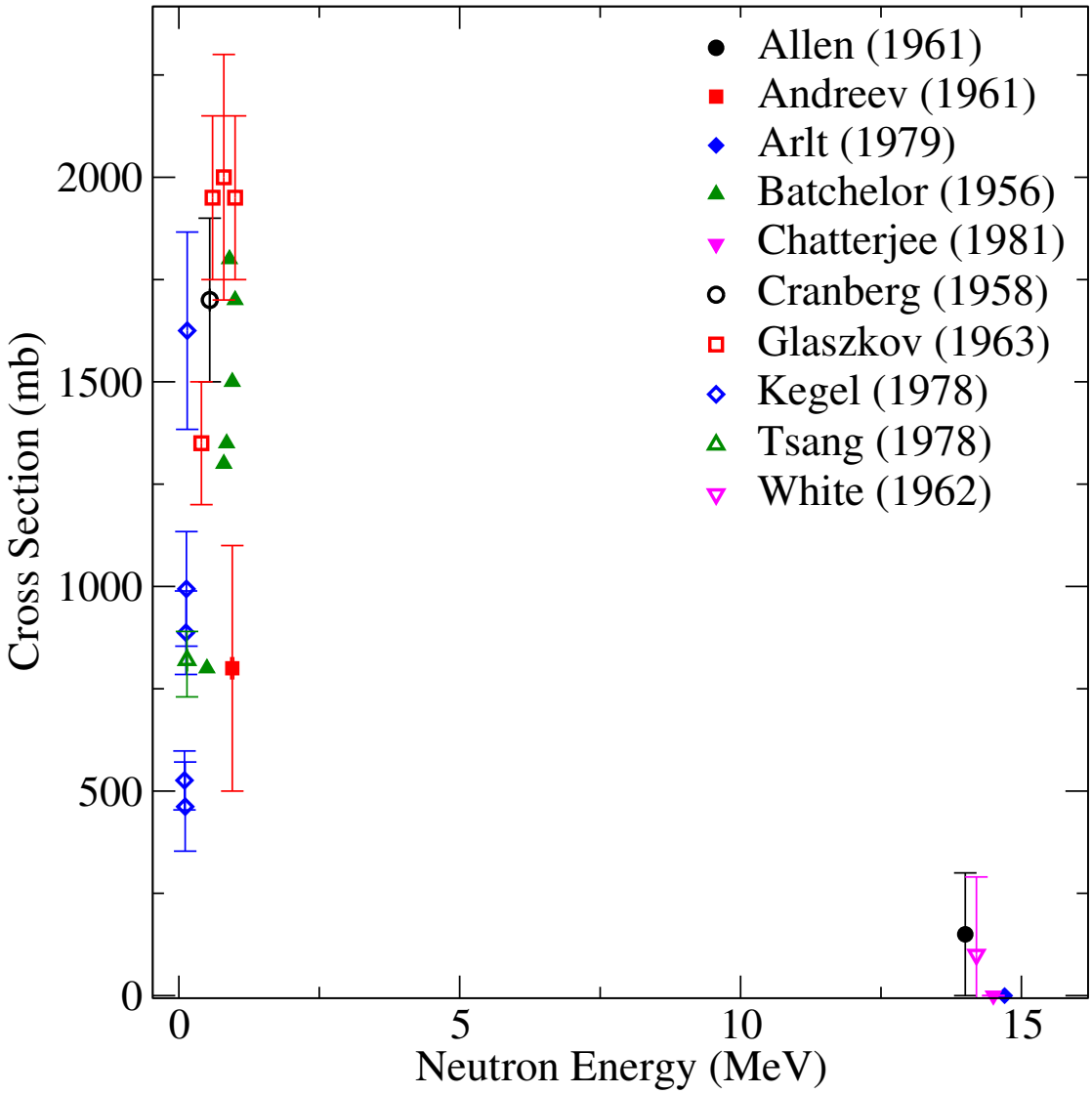

Figure 1.1: Previous cross-section measurements for $^{238}\mathrm{U}(n,n')$ (Ref.[1]-[10]).

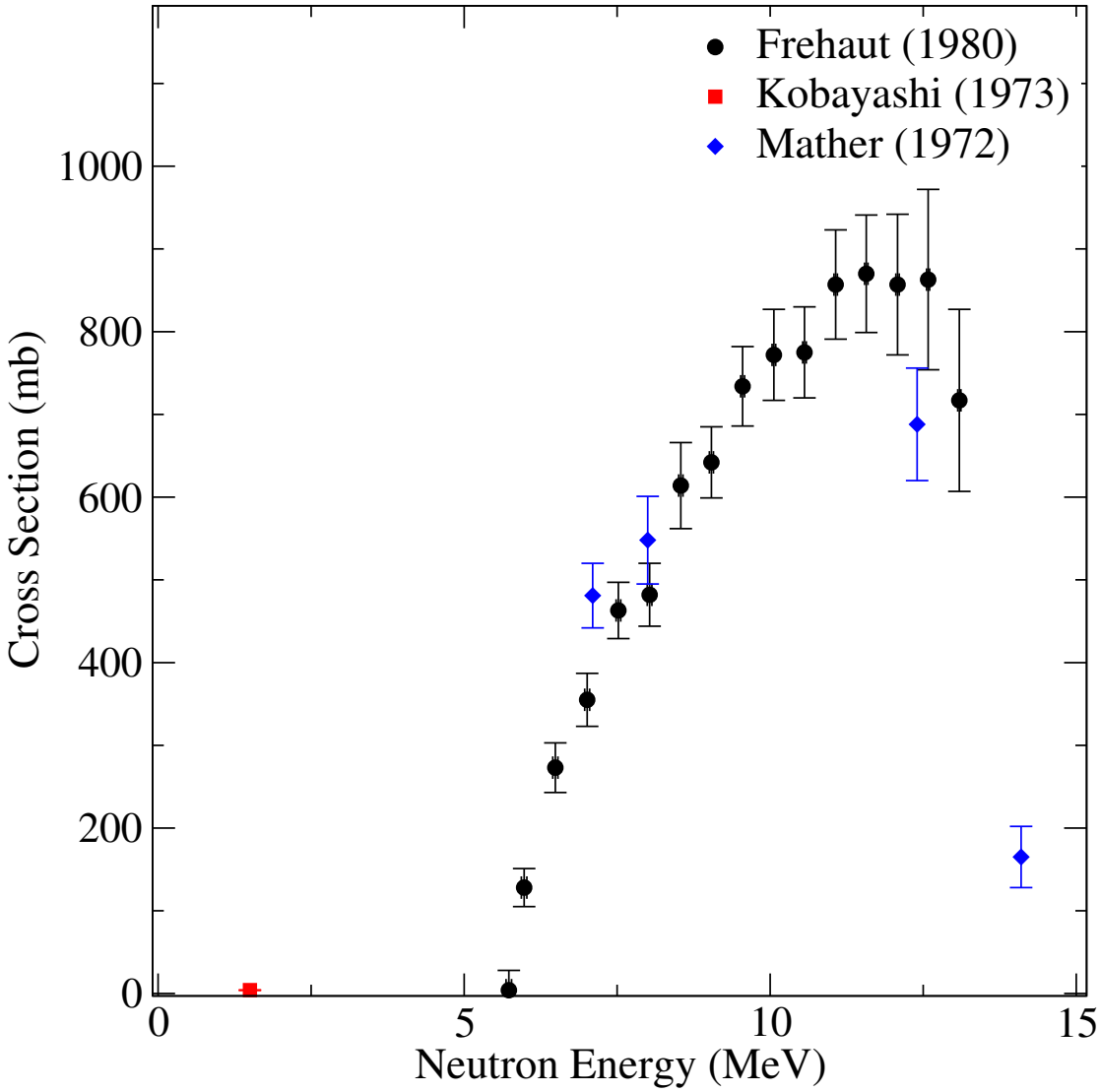

Figure 1.2: Previous cross-section measurements for $^{235}\mathrm{U}(n, 2n)$ (Ref.[11]-[13]).

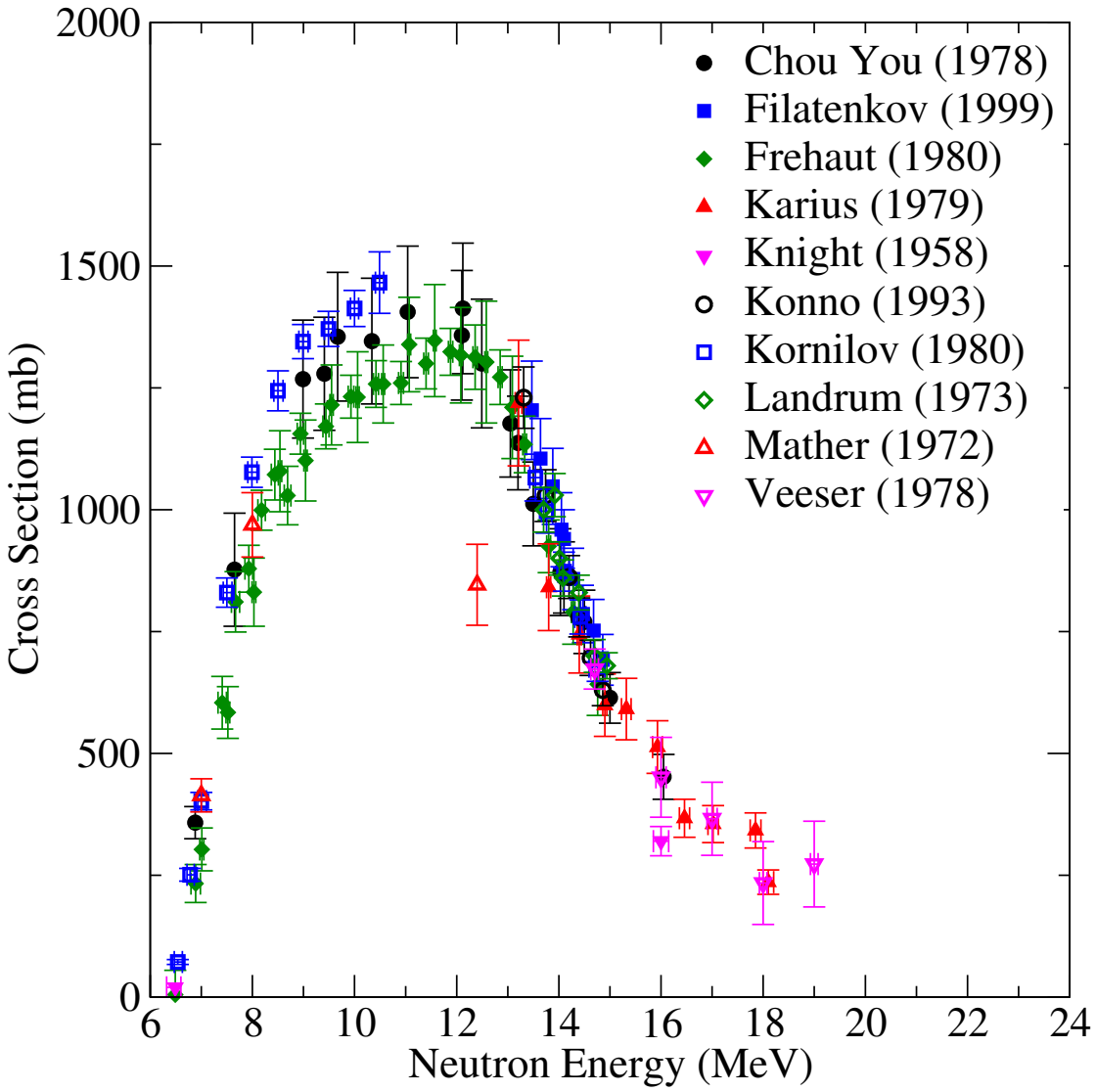

Figure 1.3: Previous cross-section measurements for $^{238}\mathrm{U}(n, 2n)$ (Ref.[11, 13]-[21]).

1.1 Motivation

Since its discovery by James Chadwick in 1932, the neutron has played an integral part in the understanding of the structure of the nucleus and of the mechanisms involved in nuclear reactions. Its charge neutrality allows it to interact with the nucleus at distances and energies that charged particles of the same energy cannot. Neutrons are of particular importance in the fields of nuclear energy and nuclear weaponry [22]. They serve as the catalyst for fission and the propagating factor in controlled and explosive chain reactions. Neutron reactions can also serve diagnostic tools to determine the neutron fluence produced by an event, either by prompt detection or by analyzing the product nuclei afterwards. In order to understand and effectively utilize these many roles of the neutron, precise nuclear reaction data is required.

In addition, precise knowledge of nuclear reactions is vital for nuclear model calculations. Accurate modeling of reactions is important both for designing nuclear reactors and, particularly since the moratorium placed on nuclear testing in 1992, in understanding the performance of nuclear weapons. These model codes rely on accurate reaction data in order to produce correct results. Inaccurate benchmarking data leads to erroneous model predictions, extremely so in nonlinear physical processes like nuclear explosions.

Uranium is an important nuclear fuel for reactors as well as nuclear weapons. ^{235}U, which makes up only about 0.72% of natural uranium, is the only naturally occurring element of significant quantity that is fissile, meaning it is capable of sustaining a chain reaction of nuclear fission. The more abundant ^{238}U, while fissionable, is not fissile and thus not directly usable as a nuclear fuel. It is, however, capable of serving as a source material for the production of fissile ^{239}Pu in nuclear reactors by neutron capture followed by two beta decays. It is also existent in nuclear weapons as a tamper material and in both weapons and reactors simply as a contaminant due to

its large natural abundance (99.28%). As an integral part of such nuclear devices, it is clearly important to have a precise understanding of the nuclear reactions that are undergone by uranium.

Nuclear fission, the process by which a nucleus can split into two lighter nuclei and produce several fast neutrons, can be induced by an energetic neutron incident on a uranium nucleus. However, depending on the kinetic energy of the neutron, fission must compete with other possible reaction channels. For neutron energies between 1 and 5 MeV, the dominant energy range for neutrons produced in fission, there is a significant probability that the neutron will inelastically scatter off of the uranium nucleus instead of inducing fission. Above around 6 MeV, the competing reaction channel for $(n, 2n)$ opens up. Knowledge of the cross sections for (n, n') and $(n, 2n)$ reactions on uranium therefore provides valuable information on the neutron energies present in nuclear devices.

Direct measurements of inelastic scattering cross sections for uranium are difficult at best. Neutron counting experiments suffer from large background due to fast neutrons produced in neutron-induced fission and very close level spacing in the uranium nucleus that are difficult to resolve with neutron detection while activation techniques to measure $(n, 2n)$ cross sections are hampered by isotopes with long half-lives such as ^{234}U ($t_{\frac{1}{2}} = 2.5$ x 10^5 y). Therefore, the somewhat indirect technique of measuring partial γ-ray cross sections is used to deduce total reaction cross sections. Product nuclei from inelastic scattering reactions are typically left in an excited state that decays by way of prompt γ-ray emission. Transitions in low-lying states typically account for the majority of decays and can be used to infer reaction cross sections fairly accurately, and model calculations can be used to account for the unmeasured decays. The formalism for connecting total reaction cross sections to partial cross sections is discussed in Chapter 2.

Chapter 2

Theoretical Background

2.1 Theoretical Basics

When a projectile approaches a target nucleus sufficiently close to interact via nuclear forces, a nuclear reaction occurs [23]. This process may be written in the notation

$$x + A \rightarrow B + y \tag{2.1}$$

or, equivalently,

$$A(x, y)B \tag{2.2}$$

for incident projectile x, target nucleus A, residual nucleus B, and emitted product y. A given projectile and target nucleus may interact in a variety of ways depending on the energetics of the reaction, resulting in different reaction products. These different reaction possibilities are referred to as reaction channels. The Q value of the reaction channel determines whether that particular channel is accessible at the given projectile energy. The Q value of a reaction is defined to be the difference between the initial and final mass energies:

$$Q = (m_A + m_x - m_B - m_y) \cdot c^2 \tag{2.3}$$

For a positive Q value, the reaction is termed exothermic, and mass energy difference is released as kinetic energy of the reaction products. For negative Q value, the reaction is endothermic, and the incident projectile must have sufficient kinetic energy to make up the mass energy difference. This energy, known as the threshold energy, can be calculated for neutral projectiles in the lab frame of reference to be

$$E_{thresh} = -Q \cdot \frac{m_B + m_y}{m_B + m_y - m_x} \tag{2.4}$$

In the case of charged projectiles, E_{thresh} must be higher in order to overcome Coulomb repulsion. The cross section $\sigma_{x,y}$ of a given reaction is a measure of the probability for the reaction to occur. The cross section of a given reaction is a function of the incident projectile energy and is generally given in units of barns, where $1\text{ b} = 10^{-28}\text{ m}^2$.

2.2 Nuclear Level Densities

When a nuclear reaction occurs, the target nucleus may be excited into higher levels. These levels have an associated width Γ and spacing D between adjacent levels. At low energies, discrete levels may be excited ($\Gamma < D$), and reaction channels passing through these levels may be treated individually. As excitation energy increases, however, the level spacing decreases while widths increase until eventually levels overlap ($\Gamma > D$). In this continuum region, individual levels can no longer be resolved, and statistical treatments must be employed. In this case, the level density $\rho(E)$ is introduced and defined for excitation energy E as

$$\rho(E) = \frac{dN(E)}{dE}, \tag{2.5}$$

where $N(E)$ is the number of levels with excitation energy less than or equal to E. An empirical formula proposed by Gilbert and Cameron [24] allows the level density to be obtained from observation of the distribution of low-energy, discrete levels. At low energies up to a cutoff energy E_c, the Constant Temperature Model (CTM) is assumed

$$\rho_{CTM}(E) = \frac{e^{\frac{E-E_c}{T}}}{T}, \tag{2.6}$$

where E_c and the nuclear temperature T are parameters that are adjusted to fit the experimental data for discrete levels. Above the cutoff energy, the Fermi Gas Model

is used, which is based on the assumption of equidistant level spacing:

$$\rho_{FGM}(E) = \frac{e^{2\sqrt{a(E-\Delta)}}}{12\sqrt{2}a^{1/4}\sigma_c(E-\Delta)^{5/4}}, \tag{2.7}$$

where the level-density parameter a, pairing energy Δ, and spin cut-off paramter σ_c^2 are treated as free parameters. At the cut-off energy E_c, boundary conditions are applied such that

$$\rho_{CTM}(E_c) = \rho_{FGM}(E_c) \tag{2.8}$$

and

$$\frac{1}{T} = \frac{d}{dU}\ln\,\rho_{FGM}(E_c), \quad (U = E - \Delta). \tag{2.9}$$

2.3 Reaction Mechanisms

Nuclear reactions can be classified into three main types based on the reaction mechanisms: direct, compound, and preequilibrium [27]. These mechanisms and the associated theoretical models are discussed in the following subsections.

2.3.1 Direct Reactions

A direct reaction takes place on a relatively short time scale (on the order of 10^{-22} s), roughly the time it takes the projectile to traverse the target nucleus. A direct reaction is primarily a surface reaction, where the projectile interacts with very few nucleons of the target nucleus and no intermediate state is created. This type of reaction is most likely to occur for light target nuclei and/or high projectile energies where the de Broglie wavelength of the projectile is sufficiently small to interact with a nucleon-sized object rather than a nucleus-sized object. Emitted products from direct reactions tend to have a highly anisotropic, forward-peaked angular distribution. The mechanism of the direct reaction can be described by assuming that all individual

nucleon-nuclear interactions may be represented by a one-body complex potential $U(r)$. This phenomenological potential is called the optical-model potential and is taken to be of the form

$$U(r) = V(r) + iW(r), \tag{2.10}$$

where the real part of the potential, $V(r)$, is responsible for the refraction of the incident projectile flux while the imaginary part, $W(r)$, reflects the absorption of incident projectile flux. These terms can be subdivided into terms accounting for Coulomb, volume, surface, and spin-orbit interactions. That is,

$$V(r) = V_c(r) - V_{vol} \cdot f_V(r) - (\frac{\hbar}{m_\pi c})^2 (\vec{l} \cdot \vec{s}) \frac{V_{spin}}{r} \frac{d}{dr} f_V(r) \tag{2.11}$$

and

$$W(r) = -W_{vol} \cdot f_W(r) - W_{surf} \cdot g_W(r), \tag{2.12}$$

where V_{vol}, W_{vol}, W_{surf}, and V_{spin} are potential well depths that are adjusted to fit experimental data. For the Coulomb term $V_c(r)$, the potential form describing a uniformly charged sphere is used:

$$V_c(r) = \begin{cases} (\frac{3R_c^2 - r^2}{R_c^2}) \cdot \frac{Z_A Z_x e^2}{2R_c}, & r \leq R_c \\ \\ \frac{Z_A Z_x e^2}{r}, & r > R_c, \end{cases} \tag{2.13}$$

where R_c is the Coulomb radius and Z_x and Z_A are, respectively, the charge of the incident projectile and target nucleus. The volume term $f_j(r)$ is taken to be of the Wood-Saxon potential form:

$$f_j(r) = \frac{1}{1 + exp[(r - R_j)/a_j]}, \qquad j = V, W, \tag{2.14}$$

where $R_j = r_j A^{1/3}$ is the nuclear radius and a_j is the diffuseness parameter, a measure of the skin thickness of the nucleus ($a_j < R_j$). The surface term $g_W(r)$ is chosen as

proportional to the derivative of the volume term and is of the form:

$$g_W(r) = -4 \cdot a_W \frac{d}{dr} f_W(r). \tag{2.15}$$

A schematic representation of the optical potential is shown in Figure 2.1. When the optical potential is inserted into the Schrödinger equation, the wavefunction can be expanded into partial waves and, in the case of elastic scattering, solved exactly or, in the case of inelastic scattering, approximately using methods such as coupled-channel equations or the distorted wave Born approximation (DWBA). In addition to enabling the calculation of cross sections for direct reactions, optical-model potentials allow for the calculation of transmission coefficients, ratios of projectile flux transmitted through the potential barrier of a nucleus to the incident projectile flux, which are a critical component of the Hauser-Feshbach statistical analysis of compound reaction cross sections.

2.3.2 Compound Reactions

On the opposite end of the spectrum from direct reactions are compound reactions. Compound reactions are relatively slow (on the order of 10^{-14} to 10^{-18} s) and are favored for heavier nuclei and/or low projectile energies. In these processes, the incident projectile is captured by the nucleus to create an intermediate excited state which decays via gamma and/or particle emission. The Bohr independence hypothesis states that the formation and decay of the compound nucleus in such a process are independent of each other [29]. During the formation of the compound nucleus, the excitation energy provided by the captured projectile is shared between all the nucleons until it reaches a statistical equilibrium, and all "memory" of the process of formation is lost. The nucleus relaxes via nucleon evaporation, emitting particles that display a Maxwellian energy distribution and are angularly distributed symmetrically about 90° with respect to the direction of the incident projectile's velocity,

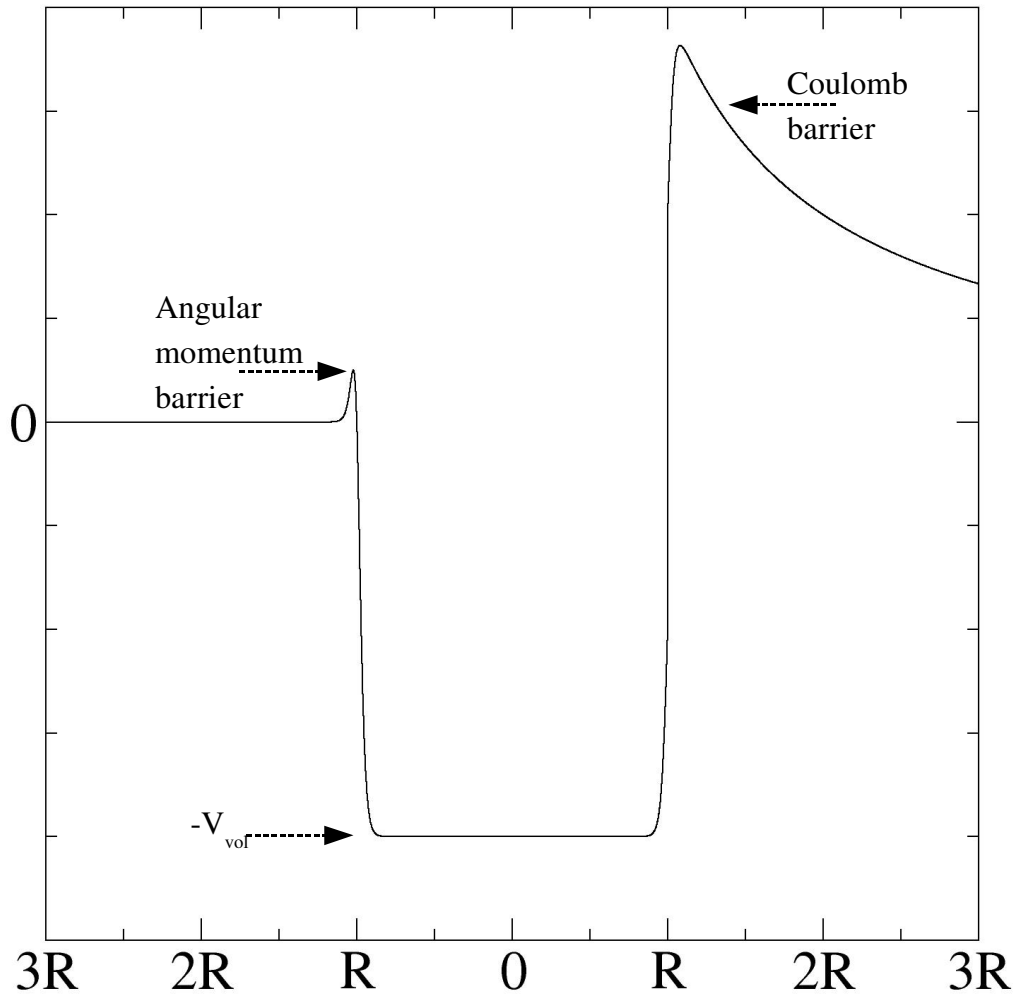

Figure 2.1: Schematic plot of optical model potential seen by neutral projectile (left) and charged projectile (right). Potential is given as a function of radial distance r.

until the energy of the nucleus is below the threshold for particle emission, after which it decays via γ-ray emission to the ground state. Because of the Bohr independence hypothesis, one can write an expression for the cross section $\sigma_{x,y}$ for a reaction leading from channel x to channel y in terms of σ_x, the cross section for the formation of the compound nucleus, and Γ_y/Γ, the branching ratio for the decay of the nucleus to channel y:

$$\sigma_{x,y} = \sigma_x \frac{\Gamma_y}{\Gamma}, \tag{2.16}$$

where Γ_y is the decay width for channel y and Γ is the total decay width. The compound nucleus formation cross section for a given orbital angular momentum l is given by

$$\sigma_x = \frac{\pi}{k_x^2}(2l+1)T_x, \tag{2.17}$$

where k_x and T_x are, respectively, the wave number and transmission coefficient for the incident channel. At low energies, reactions may pass through discrete states in the compound nucleus. In this case, the reaction cross section may be expressed in terms of Breit-Wigner resonances:

$$\sigma_{x,y} = \frac{\pi}{k_x^2}\frac{2j+1}{(2l+1)(2s+1)}\sum_{\eta}\frac{\Gamma_{\eta,x}\Gamma_{\eta,y}}{(E-E_\eta)^2+\Gamma_\eta^2/4}, \tag{2.18}$$

where $\Gamma_{\eta,x}$ and $\Gamma_{\eta,y}$ are, respectively, the partial widths of resonance η in the initial and final channels, E_η is the energy of the resonance, and Γ_η is the total width of the resonance given by the sum over the partial widths $\Gamma_{\eta,s}$:

$$\Gamma_\eta = \sum_s \Gamma_{\eta,s}. \tag{2.19}$$

The majority of compound nucleus reactions, however, excites states of higher energy where the width of the states are greater than the spacing between them. In this unresolved continuum of states, energy-averaged cross sections must be used.

Hauser-Feshbach Theory

The Hauser-Feshbach theory allows one to calculate compound reaction cross sections involving a large number of states [30]. The basic formula describing the cross section for a reaction leading from channel x to y is

$$\sigma_{x,y}^{HF} = \frac{\pi}{k_x^2} \sum_{j\Pi} \frac{2j+1}{(2s_x+1)(2s_A+1)} \frac{T_x(E_x)T_y(E_y)}{\sum_n T_n(E_n)}, \tag{2.20}$$

where s_x and s_A are the spins of the incident projectile and target nucleus, respectively, and j and Π are the total angular momentum and parity of the compound state. The transmission coefficents depend on angular momenta, and parity is conserved. This formula assumes the Bohr independence hypothesis and therefore excludes effects from correlations between incoming and outgoing channels. There are three basic methods for modifying the Hauser-Feshbach formula to account for these correlations: namely, the Hofmann-Richert-Tepel-Weidenmüller (HRTW), Moldauer, and Gaussian orthogonal ensemble (GOE) approaches.

The HRTW approach

The HRTW method assumes that the main effect of correlations between incoming and outgoing channels is in the elastic channel [31, 32]. Thus, it is convenient to write the cross section (neglecting spin weighting factors) in terms of effective transmission coefficients V_i in the form

$$\sigma_{x,y} = \frac{\pi}{k_x^2} \frac{V_x V_y}{\sum_n V_n} [1 + \delta_{xy}(W_x - 1)], \tag{2.21}$$

where W_x is a width correction factor that accounts for the correlations in the elastic channel. By using flux conservation

$$\sum_y \sigma_{x,y} = \frac{\pi}{k_x^2} T_x \tag{2.22}$$

one arrives at an expression for the effective transmission coefficients:

$$V_x = \frac{T_x}{1 + \frac{(W_x - 1)V_x}{\sum_n V_n}}. \tag{2.23}$$

Thus, if W_x is known, one can calculate V_x iteratively. Hofmann *et al.* [33] give the empirical expression

$$W_x = 1 + \frac{2}{1 + T_x^F} + 87 \left(\frac{T_x - \bar{T}}{\sum_n T_n} \right)^2 \left(\frac{T_x}{\sum_n T_n} \right)^5, \tag{2.24}$$

where

$$\bar{T} = \frac{\sum_n T_n^2}{\sum_n T_n} \tag{2.25}$$

and

$$F = 4 \left(\frac{\bar{T}}{\sum_n T_n} \right) \left(1 + \frac{T_x}{\sum_n T_n} \right) \left(1 + \frac{3\bar{T}}{\sum_n T_n} \right)^{-1}. \tag{2.26}$$

The Moldauer approach

An alternative approach is to define, for each outgoing channel y, a width correction factor $W_{x,y}$ such that

$$\sigma_{x,y} = \sigma_{x,y}^{HF} W_{x,y} = \frac{\pi}{k_x^2} \frac{T_x T_y}{\sum_n T_n} W_{x,y}, \tag{2.27}$$

where spin weighting factors have again been neglected for this compact form. In this case, an expression for the width correction factor can be found in terms of the transmission coefficients assuming T_i is small [34]. By assuming a χ^2 law with ν degress of freedom, $W_{x,y}$ can be calculated from a Porter-Thomas distribution [35] to be

$$W_{x,y} = \left(1 + \frac{2\delta_{xy}}{\nu_x} \right) \int_0^\infty \prod_n \left(1 + \frac{2T_n z}{\nu_n \sum_i T_i} \right)^{-(\delta_{xn} + \delta_{yn} + \nu_n/2)} dz, \tag{2.28}$$

where, for a mean level spacing D,

$$T_i = \frac{2\pi \langle \Gamma_i \rangle}{D}, \qquad \langle \Gamma_i \rangle << D. \tag{2.29}$$

Moldauer [36] proposes the following expression for ν obtained via Monte-Carlo calculations:

$$\nu_i = 1.78 + (T_i^{1.212} - 0.78) e^{-0.228 \sum_n T_n} \tag{2.30}$$

The GOE approach

In the Gaussian orthogonal ensemble, reaction cross sections are defined in terms of scattering matrix elements:

$$\sigma_{x,y} = \frac{\pi}{k_x^2} \left[\left\langle |S_{xy}|^2 \right\rangle - |\langle S_{xy} \rangle|^2 \right]. \tag{2.31}$$

Evaluation of this variance term results in a complicated triple integral given by Verbaarschot *et al.* in Ref. [37]. Unlike the HRTW and Moldauer methods, the GOE method does not require empirical parametrizations; however, the complicated nature of the triple integral can lead to calculation times that are impractical for cross section calculations. Numerical methods for evaluating this integral are provided by Hilaire *et al.* [38].

2.3.3 Preequilibrium Reactions

Intermediate to direct and compound reactions are preequilibrium reactions. In these reactions, particle emission from the compound nucleus takes place before statistical equilibrium has been achieved. The process can be understood semi-classically by assuming the equilibration process in the compound nucleus to take place via a cascade of two-body nucleon-nucleon interactions which create increasingly complex particle-hole states characterized by their exciton number n which is simply equal to

the sum of the number of excited particles p and holes h in the composite nuclear state [39]. At each stage, interactions are constrained by the following selection rules:

$$\Delta p = 0, \pm 1 \qquad \Delta h = 0, \pm 1 \qquad \Delta n = 0, \pm 2. \tag{2.32}$$

This process is shown schematically in Figure 2.2. There are two possible interaction chains considered in the cascade: a "Q chain" sequence where all particles (including the incident particle) are bound, and a "P chain" sequence where either the incident particle or one of the excited nucleons has enough energy to reach an unbound state. Both processes are considered together in the semi-classical exciton model. If the cross section for the formation of the compound nucleus is σ_c, the probability of particle emission at stage n is P_n, and the probability for the transition from stage n to stage $n+1$ is $\lambda_{n,n+1}$, then the cross section for pre-equilibrium emission may be written as:

$$\begin{aligned} \sigma_{PE} &= \sigma_C \lambda_{12} P_2 + \sigma_C \lambda_{12} \lambda_{23} P_3 + ... \\ &= \sigma_C \textstyle\sum_n P_{n+1} \prod_{k=1}^{n+1} \lambda_{k,k+1}. \end{aligned} \tag{2.33}$$

In the exciton model, the equiprobability of all states with the same configuration and total energy as well as the equiprobability of all possible processes is assumed at each stage. These assumptions allow one to calculate the pre-equilibrium cross section in terms of state densities $\rho_{p,h}$. If a preequilibrium particle ν is emitted with energy ϵ_ν, the cross section for pre-equilibrium emission is given by the expression [27]

$$\sigma_{PE}(\epsilon_\nu) = \sigma_C \sum_n \frac{\Gamma^{\uparrow}_{n+1}(\epsilon_\nu, E, p, h)}{\Gamma_{n+1}} \prod_{k=1}^{n+1} \frac{\Gamma^{\downarrow}_k}{\Gamma_k}, \tag{2.34}$$

where the escape width $\Gamma^{\uparrow}_{n+1}(\epsilon_\nu, E, p, h)$ for a particle with energy ϵ_ν is given in terms of the inverse process cross section $\sigma_{inv}(\epsilon_\nu)$ by

$$\Gamma^{\uparrow}_n(\epsilon_\nu, E, p, h) = \frac{\sigma_{inv}(\epsilon_\nu)(2s_\nu + 1) m_\nu \epsilon_\nu}{\pi^2 \hbar^2} \left(\frac{\rho_{p-1,h}(E - \epsilon_\nu)}{\rho_{p,h}(E - \epsilon_\nu)} \right), \tag{2.35}$$

(a) Q chain

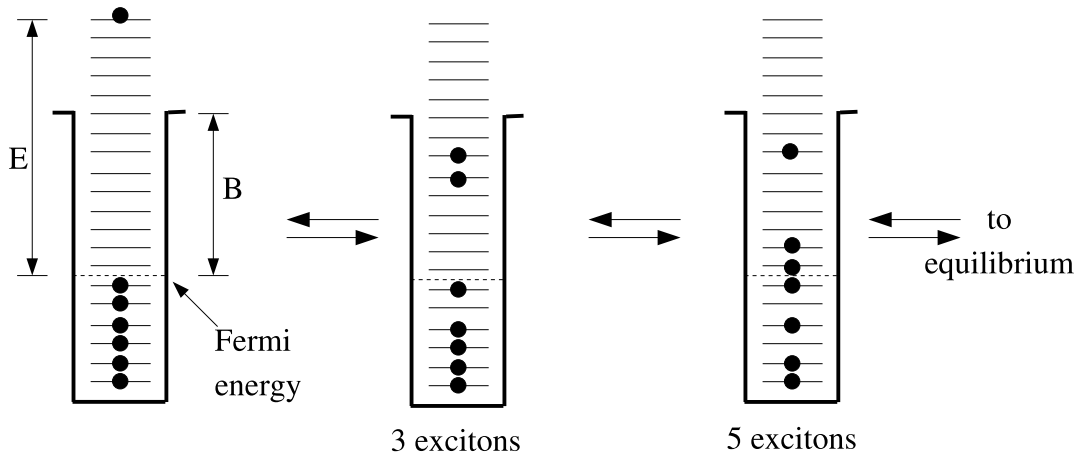

(b) P chain

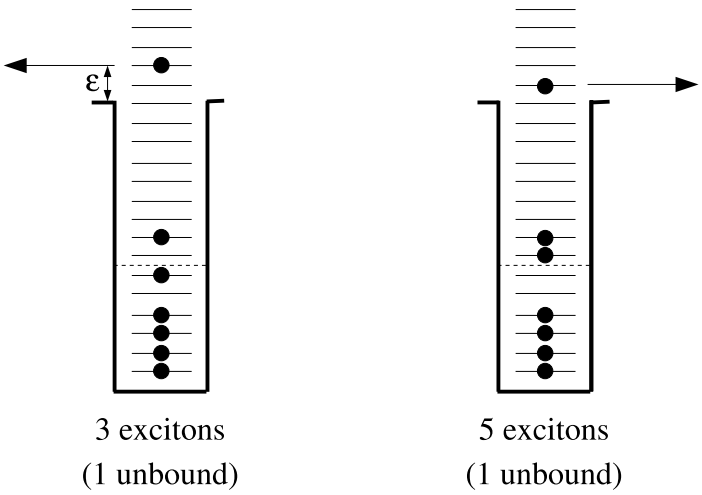

Figure 2.2: Schematic representation of the first few stages of a nucleon-induced reaction. E is the incident particle energy measured above the Fermi energy; B is the average nucleon binding energy [27].

the spreading width $\Gamma_n^{\downarrow}$ is given by

$$\Gamma_n^{\downarrow} \approx \Gamma_{n,n+2} = \frac{27\pi KE}{8\epsilon_F^3(n+1)}, \qquad K = 400 - 700 \text{ MeV}, \tag{2.36}$$

and the total width Γ_n is

$$\Gamma_n = \Gamma_n^{\downarrow} + \sum_{\nu} \int_0^{\epsilon_\nu^{max}} \Gamma_n^{\uparrow}(\epsilon_\nu, E, p, h) d\epsilon_\nu. \tag{2.37}$$

The exciton model provides a reasonable reproduction of experimental data but does not accurately reproduce the angular distribution of emitted particles nor the spin distribution of levels in the residual nucleus. Quantum mechanical treatments of the preequilibrium process have posited, the most widely used of which is the Feshbach-Kerman-Koonin (FKK) theory [28]. Unlike the exciton model, which makes no distinction between P and Q chain processes, FKK theory distinguishes between multistep compound reactions, which involve states of the Q chain, and multistep direct reactions, which involve states of the P chain. Preequilibrium emission may take place directly from the P chain or indirectly from the Q chain by transitioning from the nth stage of the chain to either the nth, $(n+1)$th, or $(n-1)$th stage of the P chain. As is implied by their name, continuum-state neutrons in multistep direct reactions retain more "memory" of their forward momentum, resulting in a more forward-peaked angular distribution, and generally populate lower-spin levels than multistep compound reactions.

2.4 Fission

For heavy compound nuclei, one must consider the possible decay channel of fission. Fission can be understood by considering the collective properties of the nucleus; Bohr and Wheeler explain the process in terms of the liquid-drop model of the nucleus [25].

Excitation energy in a nucleus allows modes of motion that give rise to collective deformation. Generally, the surface tension-like effect of the strong nuclear force restores the nucleus to sphericity. However, for heavy nuclei with large nuclear charge, the Coulomb repulsion is able to counteract the restorative force more strongly, and deformations are more easily achieved. At a critical deformation, the nucleus fissions into two neutron-rich fragments that deexcite via prompt neutron emission in order to dispose of the neutron excess. This critical deformation point corresponds to a maximum in potential energy of the nucleus as a function of deformation. This is shown schematically in Figure 2.3.

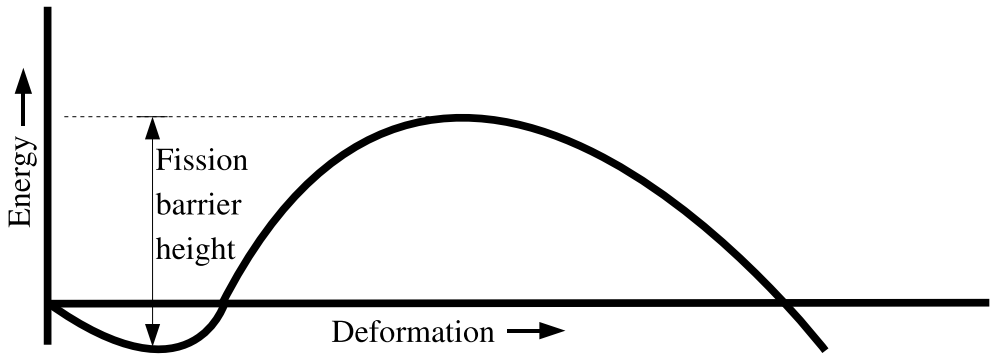

Figure 2.3: Schematic representation of potential energy of a nucleus as a function of deformation.

Fission is treated in Hauser-Feshbach formalism via the transmission coefficients provided by the Hill-Wheeler expression [26]:

$$T(E) = \frac{1}{1 + e^{-2\pi\left(\frac{\Delta\epsilon(E)}{\hbar\omega}\right)}}, \tag{2.38}$$

where $\Delta\epsilon(E)$ is the energy deficit relative to the top of the barrier and ω is the frequency of a harmonic oscillator in a potential well equal to the negative of the barrier potential-energy function.

2.5 Gamma-ray Emission

An important channel for nuclear deexcitation is the emission of electromagnetic radiation in the form of γ rays [27]. Gamma emission may compete with particle emission for nuclear excitation energy above particle separation threshold and generally dominates below (with the notable exception of energies where fission cross sections are large). Classically, electromagnetic radiation may be expanded in terms of multipole moments. Quantum mechanically, emitted photons may be associated with electromagnetic multipoles based on their angular momentum and parity. A nucleus may decay from an initial state with angular momentum J_i and parity π_i to a state with J_f and π_f by emitting a γ ray with angular momentum L such that

$$|J_i - J_f| \leq L \leq J_i + J_f, \qquad (L \neq 0). \tag{2.39}$$

If there is no change in parity between states ($\pi_i = \pi_f$), the emitted photon must have even parity, and it may be associated with an electric multipole if L is even or a magnetic multiple if L is odd. Likewise, a photon of odd parity must result from a transition between states that changes parity ($\pi_i \neq \pi_f$), and it may be associated with an odd-L electric or even-L magnetic multipole. By assuming the radiation results from the transition of a single proton between states, Weisskopf estimates the transition probabilities for the lower order multipoles to be [40]:

$$\begin{array}{ll} \lambda(E1) = 1.0 \times 10^{14} A^{2/3} E_\gamma^3 & \lambda(M1) = 5.6 \times 10^{13} E_\gamma^3 \\ \lambda(E2) = 7.3 \times 10^{7} A^{4/3} E_\gamma^5 & \lambda(M2) = 3.5 \times 10^{7} A^{2/3} E_\gamma^5 \\ \lambda(E3) = 34 A^2 E_\gamma^7 & \lambda(M3) = 16 A^{4/3} E_\gamma^7. \end{array} \tag{2.40}$$

2.5.1 Strength Functions

As for other decay channels, γ-decay channel cross sections are calculated in statistical models by their transmission coefficients. For a multipole transition of species X and

order L, the transmission coefficient is given by [41]

$$T_{XL}(E_\gamma) = 2\pi E_\gamma^{(2L+1)} f_{XL}(E_\gamma), \tag{2.41}$$

where $f_{XL}(E_\gamma)$ is the γ-ray strength function. The simplest model for $f_{XL}(E_\gamma)$ is the single-particle model used to calculate the estimates given in Equation 2.40. This model is sufficient for transitions of multipolarity M2, E3, or higher but overestimates the strength function for lower orders, particularly in the case of E1 transitions [42]. A more accurate description is found by relating the strength function for emission with the inverse process, photoabsorption [43, 44]. The Brink-Axel expression gives the form

$$f_{XL}(E_\gamma) = \frac{1}{(2L+1)(\pi\hbar c)^2} \frac{\sigma_{XL} E_\gamma \Gamma_{XL}^2}{(E_\gamma^2 - E_{XL}^2)^2 + E_\gamma^2 \Gamma_{XL}^2}, \tag{2.42}$$

where σ_{XL}, Γ_{XL}, and E_{XL} are, respectively, the strength, width, and energy of the multipole's associated giant resonance in photoabsorption. This Lorenzian form describes experimental data much more accurately than the single particle model for low-order transition but, in the case of E1 transitions, is inadequate at or below neutron separation energies. In this case, Kopecky and Uhl [41] suggest the generalized Lorentzian of the form

$$f_{E1}(E_\gamma, T) = \frac{1}{3(\pi\hbar c)^2} \left[\frac{E_\gamma \tilde{\Gamma}(E_\gamma)}{(E_\gamma^2 - E_{E1}^2)^2 + E_\gamma^2 \tilde{\Gamma}(E_\gamma)^2} + \frac{0.7\Gamma_{E1} 4\pi^2 T^2}{E_{E1}^3} \right] \sigma_{E1} \Gamma_{E1}, \tag{2.43}$$

where $\tilde{\Gamma}(E_\gamma)$ is the energy depending damping width which is given by [45]

$$\tilde{\Gamma}(E_\gamma) = \Gamma_{E1} \frac{E_\gamma^2 + 4\pi T^2}{E_{E1}^2} \tag{2.44}$$

and T is the nuclear temperature given by

$$T = \sqrt{\frac{E_n + S_n - \Delta - E_\gamma}{a(S_n)}}, \tag{2.45}$$

where E_n, S_n, Δ, and $a(S_n)$ are the incident neutron energy, separation energy, pairing correction, and level-density parameter, respectively.

2.5.2 Angular Distribution

In general, γ rays are not emitted from an excited nucleus isotropically but have some angular distribution characterized by the multipolarity of the transition. The γ-ray angular distribution with respect to the axis defined by the incident particle trajectory may be written as a superposition of Legendre polynomials [46]:

$$W(\theta) = 1 + \sum_{k=2(even)} \rho_k A_k P_k(\cos(\theta)). \tag{2.46}$$

The sum is over even orders of the Legendre polynomials because, due to the assumption of the Bohr independence hypothesis, there is nothing to distinguish forward of 90° from the backward direction. The angular distribution coefficient A_k has the form

$$A_k = \frac{1}{1+\delta^2}\left[F_k(L,L,J_f,J_i) + 2\delta F_k(L,L',J_f,J_i) + \delta^2 F_k(L',L',J_f,J_i)\right], \tag{2.47}$$

where δ is the mixing ratio between the competing L and L' multipoles and the F_k's are the Ferentz-Rosenzweig coefficients given in terms of Clebsch-Gordon and Racah W-coefficients by the expression [47]

$$\begin{aligned} F_k(L,L',J_f,J_i) &= (-1)^{J_f-J_i-1}\sqrt{(2J_i+1)(2L+1)(2L'+1)} \\ &\quad \times \langle L1L'(-1)|k0\rangle\, W(LL'J_iJ_i;kJ_f). \end{aligned} \tag{2.48}$$

The coefficient ρ_k in Equation 2.46 accounts for the statistical distribution of spin substates in the excited nucleus and can be written as

$$\rho_k = \sqrt{(2J_i+1)} \sum_{m=-J_i}^{J_i} (-1)^{J_i-m} \langle J_i m J_i(-m)|k0\rangle\, P(m), \tag{2.49}$$

where $P(m)$ is the normalized population of substate m. It is generally assumed that $P(m)$ is described by a Gaussian distribution centered about $m = 0$ [48]:

$$P(m) = \frac{e^{-\frac{m^2}{2\sigma^2}}}{\sum_{m=-J_i}^{J_i} e^{-\frac{m^2}{2\sigma^2}}}, \tag{2.50}$$

where the width parameter σ is a measure of the degree of spin alignment in the nucleus.

2.5.3 Internal Conversion

A competing decay channel for electromagnetic transitions in excited nuclei is internal conversion, where the electromagnetic fields of the nucleus interact with an atomic electron, providing it with sufficient energy to escape the atom. This process can be associated with an internal conversion coefficient which is simply the ratio of the probability for internal conversion to the probability for γ emission [23]:

$$a = \frac{\lambda_e}{\lambda_\gamma}. \tag{2.51}$$

The internal conversion coefficient increases rapidly with nuclear charge ($\propto Z^3$) and transition multipolarity and decreases rapidly with transition energy. It also provides a channel for $L = 0$ transitions which are forbidden for γ-ray emission. (See Equation 2.39.)

Chapter 3

Model Calculations

Partial cross sections for $^{238}\mathrm{U}(n, n'\gamma)$ and $^{235,238}\mathrm{U}(n, 2n\gamma)$ reactions were calculated using the statistical Hauser-Feshbach model described in Section 2.3.2 as implemented in the GNASH [49] and TALYS [50] reaction codes. The general prescription for both of these codes is to assume reactions occur in a series of binary reactions where, for each step in the reaction chain, particle and γ-ray emission is calculated. These calculations are bound by laws of conservation for energy, spin, and parity. Overviews of the GNASH and TALYS codes are given in Sections 3.1 and 3.2, respectively. A flowchart of the two codes is shown in Figure 3.1.

The Gaussian width parameter σ found in Equation 2.50 was calculated utilizing the AVALANCHE code [51, 52]. For these calculations, the Gaussian assumption was relaxed to allow separate σ_k values to be calculated for $k = 2, 4$. Section 3.3 provides a brief overview of the code.

3.1 GNASH

The GNASH nuclear reaction computer code implements Hauser-Feshbach theory in an open-ended sequence of nuclear reactions. It is expected to be most accurate for incident particle energies ranging from 1 keV to 50 MeV. Allowed incident particle types are neutrons, protons, deuteron, triton, ^{3}He, and alphas. Allowed decay channels include all incident particles as well as γ rays. Input data for nuclear structure, optical-model transmission coefficients, and ground state values (spin, parity, and mass) are introduced via separate files (namely, TAPE8, TAPE10, and TAPE13, respectively). An additional INPUT file is used to direct calculations and allows for

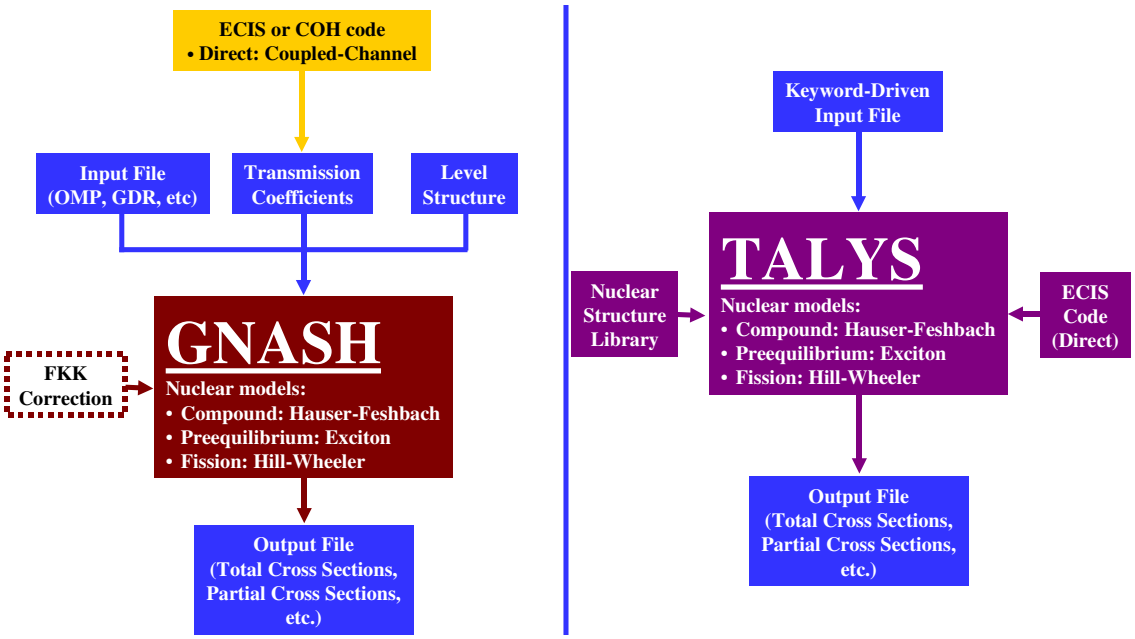

Figure 3.1: Flowchart of GNASH and TALYS codes.

the modification of parameters as needed to tune results to experimental data. An example INPUT file is given in Appendix A.1. For the strongly deformed actinide nuclei, transmission coefficients are calculated externally using coupled-channel optical-model calculations implemented in the ECIS-97 code [53] which uses an iterative sequence of calculations to solve the coupled equations assuming the coupling terms are not too strong. Level densities were calculated using the Gilbert-Cameron model; the generalized Lorentzian form of the giant-resonance model given by Kopecky and Uhl was utilized to obtain γ-ray strengh functions. Compound nucleus cross sections are corrected for width fluctuation, preequilibrium, and direct-reaction effects. The Moldauer model was used to correct for width fluctuation. Calculation of preequilibrium corrections were performed utilizing the semi-classical exciton model as formulated by Kalbach in the PRECO code [54]. Fission transmission coefficients are determined using the Hill-Wheeler expression. Up to three uncoupled fission barriers may be used in GNASH. An OUTPUT file is generated containing the primary output information of absolute angle-integrated particle and γ-ray spectra as

well as discrete level excitation and deexcitation cross sections. Absolute reaction cross sections are obtained by integrating and summing calculated spectra. GNASH calculation results are compared with experimental data in Chapter 6.

3.2 TALYS

TALYS is a nuclear reaction program which implements a suite of nuclear reaction models into a single code. It is capable of calculating nuclear reactions involving neutrons, γ rays, protons, deuterons, tritons, ^{3}He, and alphas for incident neutron energies between 1 keV and 200 MeV. Nuclear structure and model parameters are implemented through an internal reference library based on the Reference Input Parameter Library [56]. Direct reaction and transmission coefficient calculations are obtained via the ECIS-97 code which is implemented as a subroutine in TALYS. Compound reaction cross sections are calculated using the Hauser-Feshbach formalism with the option of three different width correction models: Moldauer, HRTW, or GOE. For these calculations, the Moldauer model was chosen. Preequilibrium corrections are implemented using phenomonological calculations based on Kalbach's systematics. Kopecky and Uhl's generalized Lorentzian formalism was used to calculate γ-ray transmission coefficients while the Hill-Wheeler expression was used to calculate the T_i's for fission. Cross sections can be calculated using a simplified input file listing only the species of the projectile, target element, target mass, and incident projectile energy; however, the inclusion of keywords in the input file allows the user to vary nuclear models and parameters in order to tune calculations to experimental data as well as to control which cross sections are generated in the output file. TALYS has been extensively tested by comparison with experimental data [50]. An example input file is given in Appendix A.2. TALYS calculation results are compared with experimental data in Chapter 6.

3.3 AVALANCHE

The set of routines that make up the AVALANCHE code were developed in order to calculate side-feeding intensities and spin state orientation parameters for residual nuclei in compound nucleus reactions. Reactions are assumed to take place in a chain of binary reactions. Two main programs make up the AVALANCHE code: AVA_FUS and AVA_CAS. The AVA_FUS code calculates initial feeding flow and orientation parameters for the formation of the compound nucleus. The input file contains information on the target and projectile mass, spin, and parities, the binding energy of the projectile particle in the compound nucleus, the incident projectile energy, and the transmission coefficients. The output of this routine is then input into the AVA_CAS code along with a separate input file containing the mass and charge of the parent nucleus, the mass, charge, spin, and binding energy of emitted particles, and optical-model and nuclear level-density parameters. The Gilbert-Cameron formula is used to calculate level densities. The generalized Lorenztian formalism is used for E1 strength function calculations while E2 and M1 strength functions are calculated using single-particle approximations. Discrete nuclear levels and transmission coefficients are implemented via separate external files. The AVA_CAS program must be run separately for each step in the reaction chain. A flowchart of the process is shown in Figure 3.2 for calculation of $^{235}\mathrm{U}(n, 2n\gamma)$. Example input files for both AVA_FUS and AVA_CAS are given in Appendix A.3. Angular distributions obtained using orientation parameters calculated with AVALANCHE are given in Chapter 6.

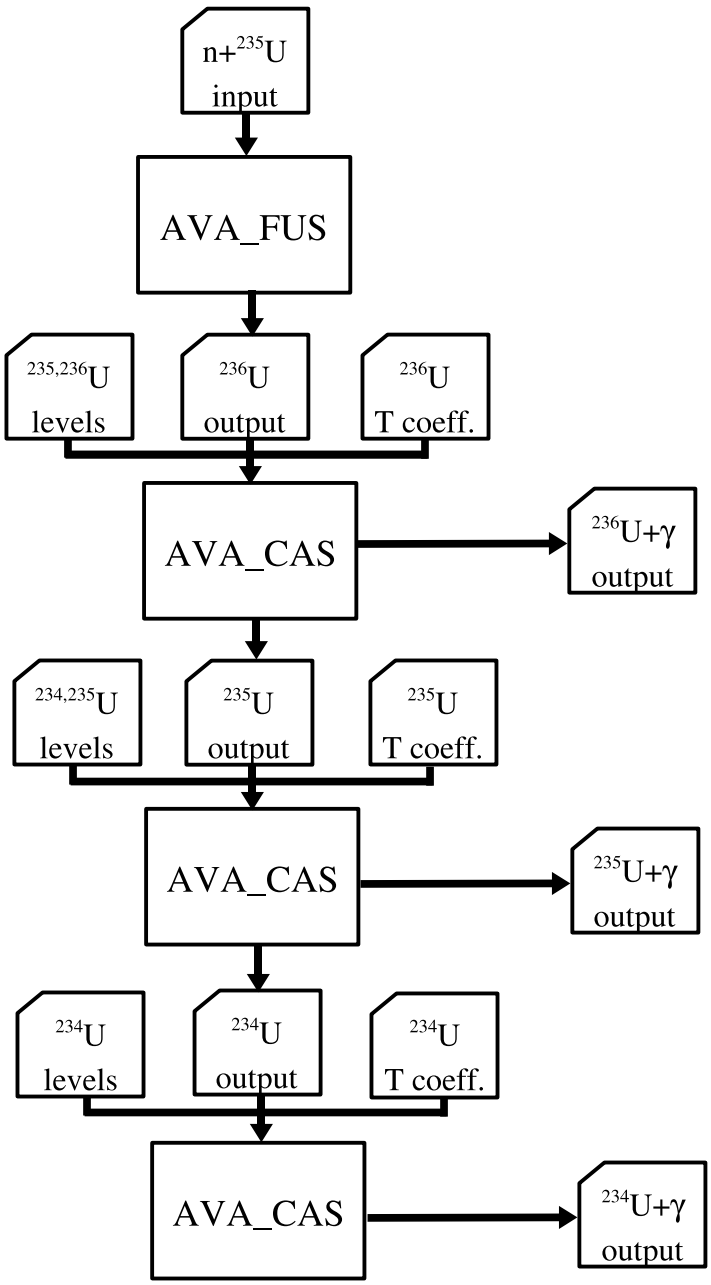

Figure 3.2: Flowchart of the AVALANCHE code for $^{235}\mathrm{U}(n, 2n\gamma)$ calculation.

Chapter 4

Experimental Details

In this experiment, $^{235,238}\mathrm{U}(n, xn\gamma)$ partial cross sections were measured for incident neutron energies ranging from 5 to 14 MeV. Uranium targets were bombarded with pulsed, nearly monoenergetic neutrons, and a combination of high-purity germanium (HPGe) clover and planar detectors were used to measure the emitted gamma rays from the excited nucleus. Simultaneous bombardment of a natural iron foil and measurement of resultant gamma rays emitted enabled relative cross-section normalization. The measurements were performed over a span of four years and represent about 1100 hours of beam time. A floor plan of the TUNL accelerator bay and target rooms is provided for reference in Figure 4.1.

4.1 Deuteron Beam Production and Transport

Fast neutrons used in this experiment were produced via the $^{2}\mathrm{H}(d, n)^{3}\mathrm{He}$ reaction by bombarding a deuterium gas cell with an accelerated beam of deuterons. Section 4.2.1 will describe this reaction in more detail. The following sections will be concerned with the production, acceleration, and transport of the deuteron beam.

4.1.1 Negative Ion Source

The deuteron beam utilized in the source reaction is produced by the Direct Extraction Negative Ion Source (DENIS II), a duoplasmatron source located in the low-energy end of the accelerator bay. A continuous beam of ions is extracted from the source head which is held at -50 V with respect to ground and accelerated toward ground potential, resulting in a ion beam with an energy of 50 keV.

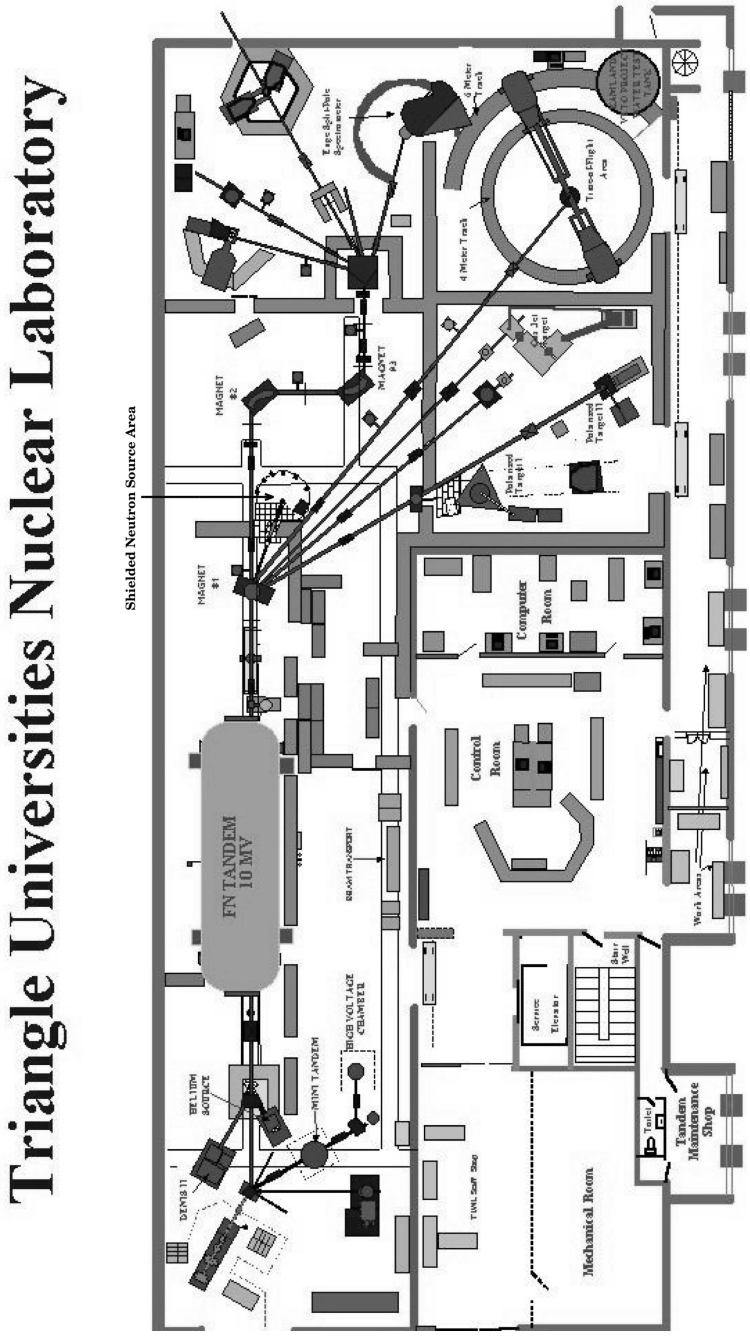

Figure 4.1: Floor plan for Triangle Universities Nuclear Laboratory.

The beam source is shown schematically in Figure 4.2. A filament is comprised of a nickel wire mesh rolled and coated with a carbonate with a low work function with respect to the thermionic emission of electrons. Gas is injected into the evacuated region around the filament to a pressure of around 10^{-2} torr. Current is raised in the filament until an arc discharge between the filament and the anode is struck and maintained. A solenoidal magnetic field produced by the source magnet constrains the radial motion of the electrons in the arc. Electrons accelerate toward the anode and collide with atoms in the gas, producing a plasma of negative and positive ions depending on whether the atom captures the electron or loses an electron due to collision. The dense core of the plasma primarily consists of positive ions while the negative ions inhabit a less dense halo around the core. Therefore, the aperture of the anode is offset from the center in order to select out the negative ions for extraction. Due to the large pressure gradient across the opening, ions are drawn through the aperture and a second plasma forms on the other side. It is from these two plasmas that the duoplasmatron gets its name. Negative ions are separated out of the second plasma by applying a voltage difference between the anode and the extractor electrode. These extracted ions are then focused by an electrostatic lens and accelerated to 50 keV before entering the beam transport system.

DENIS II is capable of producing a variety of negative ion beams depending on the species of gas injected into the source head. For example, proton beams are produced by injecting hydrogen. In order to produce the deuteron beams used in this experiment, deuterium gas was injected (mixed with hydrogen to keep the deuteron current low enough to safely inject into the tandem while maintaining the correct pressure).

As the low-energy portion of the transport system is designed to transport beams from a variety of sources to the tandem accelerator, an inflection magnet is used to

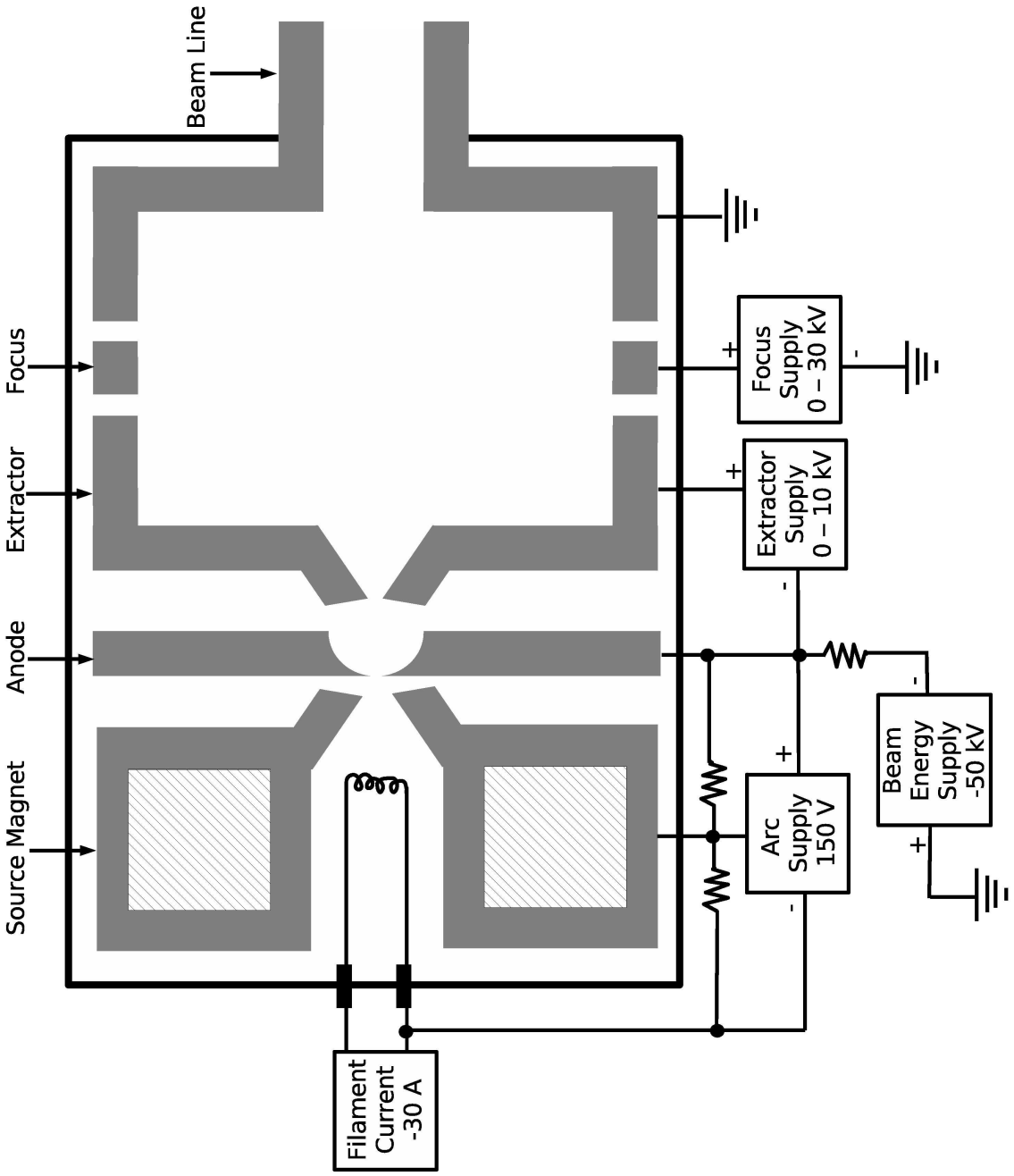

Figure 4.2: Direct extraction negative ion source (DENIS II).

direct the incoming beam down the correct trajectory to enter the accelerator as well as to select out the correct species of ion for transport. Upon exiting DENIS II, the 50 keV deuteron ion beam is bent by the inflection magnet, steered by a combination of electromagnetic steerers, and focused by electrostatic and magnetic quadrupole lenses.

4.1.2 Beam Pulsing

Before entering the tandem accelerator, the ion beam can be pulsed using a combination of two electrostatic choppers and a single double-drift buncher [57]. This system, in combination with the DENIS II source, can provide up to 3 μA of pulsed deuteron current with a pulse width of 2 ns and a repetition rate of 2.5 MHz or smaller (by factors of two).

The main chopper consists of two parallel conducting plates across which is applied a sinusoidal voltage of 2.5 MHz. The resulting oscillating electric field sweeps away portions of the ion beam leaving only those ions that pass the plates at the zero crossings of the voltage. This process throws away approximately 80% of the dc beam current. The resulting beam packets have a repetition rate of 5 MHz due to the fact that there are two zero crossings per sinusoidal period. The second, auxiliary chopper consists of two parallel conducting plates situated at 90° with respect to the plates of the main chopper. A variable frequency square wave voltage phased to the main chopper is applied across these plates and allows the user to further control the frequency of the beam packets. For the purposes of this experiment, the auxiliary chopper was used to throw away every other beam packet, resulting in an overall beam current reduction of 90%.

The bunching system consists of two double-drift bunchers [58]. A double-drift buncher is comprised of three coaxial conducting cylinders separated by two acceler-

ation gaps. The two outer cylinders are grounded while the center is driven with a sinusoidal voltage. The phase of this voltage is timed with the chopping system such that the front edge of the beam packet is slowed while the rear edge is accelerated. The resulting velocity distribution of the ions in the packet is such that the ion pulse is optimally compressed when it reaches the target area. The components of the first buncher are of such length as to be sufficient to bunch deuterons while bunching of protons requires the use of both double-drift bunchers.

4.1.3 Tandem Accelerator and Beyond

After being properly pulsed, ion beams are accelerated by way of the model FN Tandem Van de Graaff accelerator. A centralized terminal electrode is housed within a large steel tank filled with an insulating gas to help prevent electrical discharges and is charged to a large positive voltage via two charging chains. Negatively-charged ions passing through an evacuated tube in the tank are accelerated toward the terminal. Ions pass through a thin carbon foil located in the terminal which strips electrons away, resulting in the ions gaining a net positive charge. The positive charge of the terminal then accelerates these ions away toward the accelerator exit. The resulting beam energy is equal to the 50 keV injection energy plus twice the terminal voltage times the positive charge of the ion. The tandem accelerator is shown schematically in Figure 4.3.

The Pelletron chain charging system uses two chains constructed of tubular conducting metal pellets connected by nylon links to charge a centralized terminal electrode. The pellets are charged inductively by a negatively-charged inductor electrode situated near the chains drive pulley. The positively-charged links are driven toward the electrode where the charge passes into the terminal pulley, resulting in a net positive charge on the terminal. A negatively-charged suppressor electrode located

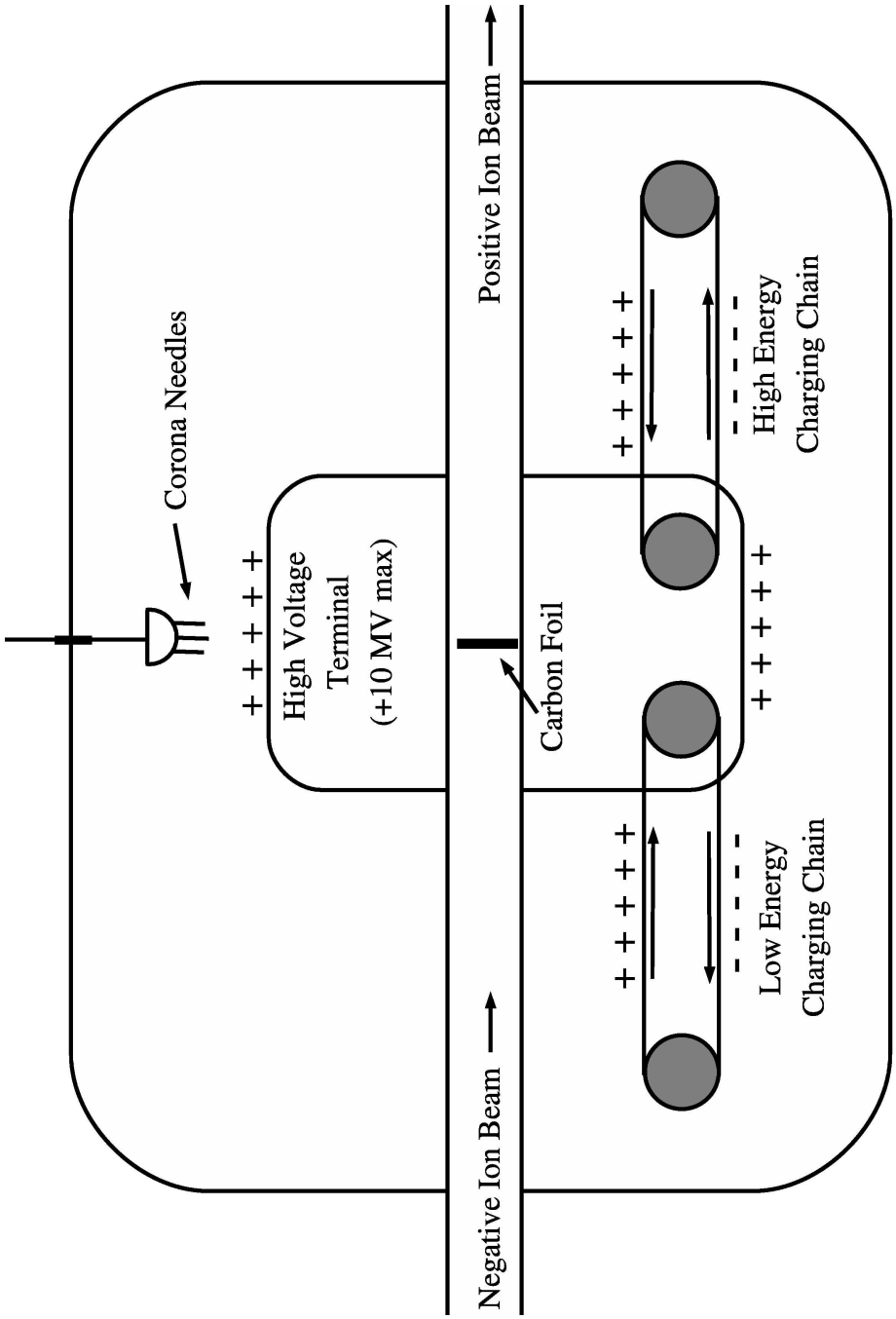

Figure 4.3: Schematic for tandem Van de Graaff accelerator.

in the terminal prevents arcing as the charge passes onto the terminal pulley.

After exiting the accelerator, the ion beam is steered by an analyzing magnet into one of various beam lines at angles ranging from 20° to 70°. The field strength of this magnet is set to select out ions of a given charge and energy. In order to preserve a stable terminal voltage and thus constant beam energy, charge deposited and removed from the accelerator terminal is regulated by way of a feedback system. Sharp metal needles called corona needles are mounted on a movable arm directly opposite the terminal such that they can be extended toward or pulled away from the terminal. The needles are used to remove charge from the terminal via corona discharge. By varying the resistance of the corona circuit, varying amounts of charge may be drawn away from the terminal. Control slits located downstream from the analyzing magnet provide a feedback signal for the corona circuit. A current imbalance on either slit will produce an error signal that causes the corona circuit to draw more or less charge in order to maintain a stable beam. For this experiment, the deuteron beam was bent through the analyzing magnet to the 20° beam line. From there, the beam passes through a magnetic steerer, a beam profile monitor, and two collimators before reaching the deuterium gas cell.

4.2 Neutron Source and Collimation

4.2.1 Neutron Source

The pulsed deuteron beam is used to produce pulsed neutron beams ranging from 4 to 20 MeV via the $^{2}\mathrm{H}(d,n)^{3}\mathrm{He}$ reaction. A gas cell pressurized with 99.99% pure deuterium gas is located at the end of the beam line. A schematic of the cell is shown in Figure 4.4. The gas pressure in this cell can be varied to achieve various energy spreads and neutron fluxes. At the majority of the neutron energies used in this experiment, the gas cell was pressurized to 7.8 atm, though lower pressures

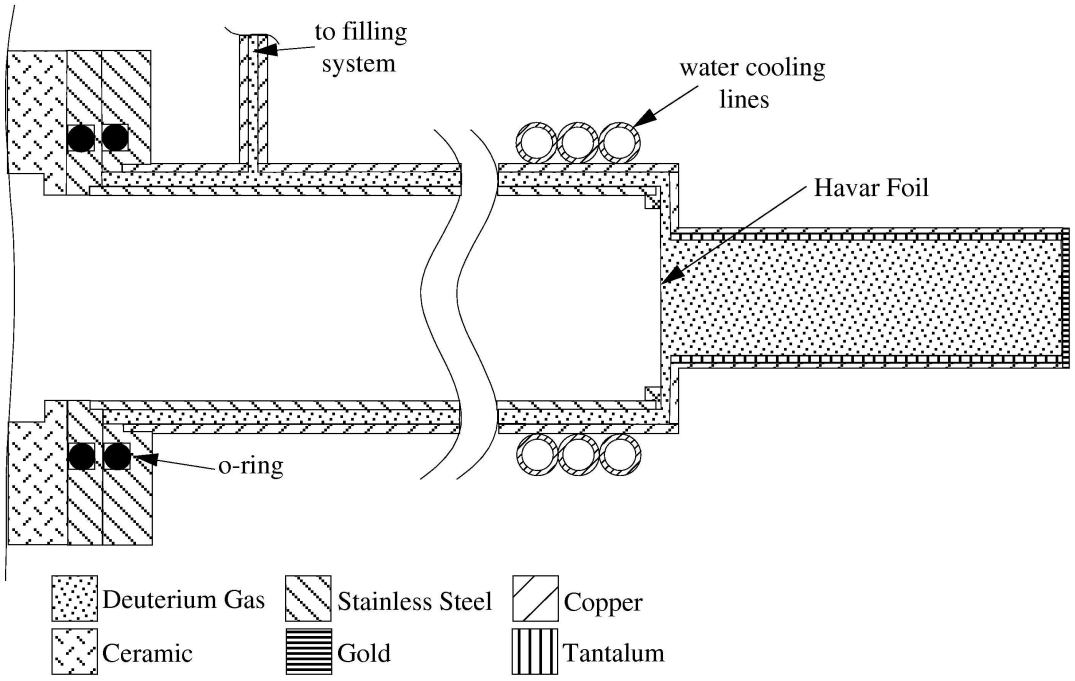

Figure 4.4: Schematic for deuterium gas cell.

were sometimes used at lower neutron energies in order to achieve a smaller neutron energy spread. For a list of the gas-cell pressures used at each neutron energy and the associated energy spread, see Table 4.1. Deuteron ions enter the cell through a 0.25 mil (6.35 μm) Havar foil which separates the deuterium gas from the vacuum of the beam line. The downstream end of the gas cell is capped by a 0.051 cm gold beam stop which is silver-soldered onto the body of the gas cell. The body is a 3 cm long copper cylinder with a diameter of 1 cm. The cell is cooled by 10° C distilled water circulated through copper coils wrapped around the cell as well as by two compressed air jets directed at either end of the cell. The assembly is electrically isolated from the beam line so that charge accumulated on the beam stop could be collected and sent to a beam-current integrator (BCI) which generated a pulse per fixed amount of charge. This signal is sent to a scaler to be counted.

The ^{2}H$(d,n)^3$He reaction is a good choice for a neutron source reaction due to the

E_n (MeV)	HWHM (MeV)	Gas Pressure (atm)
5	0.50	4.9
6	0.55	7.8
8	0.35	7.8
10	0.25	7.4
11	0.23	7.8
12	0.21	7.8
14	0.17	7.8

Table 4.1: Gas-cell pressure used and associated energy half width at half maximum (HWHM) for each incident neutron energy.

relatively large cross section for the production of forward-angle neutrons at energies between 7 and 20 MeV [59]. The most energetic neutrons produced by this reaction are emitted at forward angles with both the neutron energy and cross section for production rapidly diminishing as the angle is increased from 0°. Additionally, the reactions Q-value of 3.26 MeV allows for good energy separation between lower-energy neutrons produced by the breakup of incident deuterons on the gold beam stop of the gas cell (threshold 2.22 MeV) and three- and four-body breakup in the deuterium gas (thresholds 4.45 MeV and 8.90 MeV, respectively).

4.2.2 Shielding and Collimation

Despite the strong forward-angle preference of the ^{2}H$(d,n)^3$He reaction, fast neutrons and gamma rays are produced at all angles in the deuterium gas cell. Therefore, the neutron source must be shielded and the neutron beam collimated in order to reduce direct and accidental background. The Shielded Neutron Source Area (SNSA) is shown schematically in Figure 4.7. Detectors in the area are protected from neutrons and γ rays produced in the gas cell by a multi-layered shielding wall composed of paraffin, concrete, lead, and various other heavy metals.

A double-truncated collimator, 117 cm long and made from tapered copper (79 cm

long) and polyethylene bars (38 cm long), is fitted inside an opening in the shielding wall along the beam axis with the throat of the collimator located 33.5 cm from the center of the gas cell and is shown schematically in Figure 4.5. The collimator is

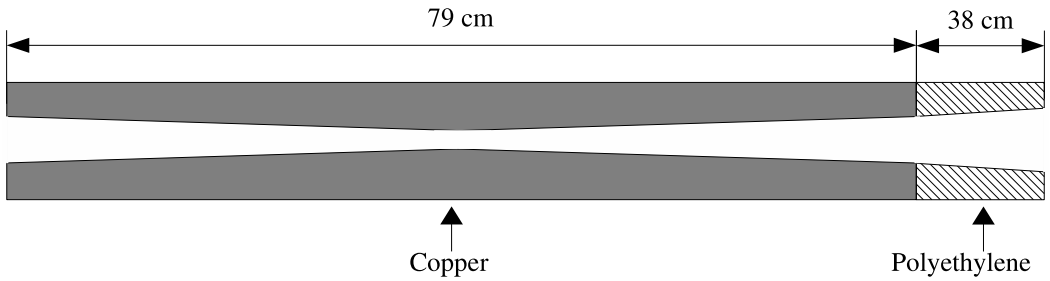

Figure 4.5: Double-truncated copper collimator. (Not to scale.)

designed to minimize the amount of forward-scattered neutrons from the collimator walls while allowing the target to be exposed to a spatially homogenous field of unscattered neutrons.

After installation of the collimator, the beam profile was measured for 8 MeV neutrons at the target position (74.5 cm from the shielding wall). As the width of the neutron beam profile determines the closest distance the detectors can be positioned from the target, its precise determination is very important. A thin plastic scintillator detector (2.5 cm x 3.8 cm x 0.3 cm) with high enough electronic threshold to avoid counting gamma rays was scanned through the beam to perform the profile measurements. Counts for each detector position were accumulated for an identical amount of charge deposited by the incident deuteron beam in the deuterium gas cell in order to account for beam fluctuations during the measurement. The raw counts were corrected for edge effects (lower count rates observed when the scintillator is positioned at the edge of the circular neutron beam) and angle effects (the change in effective geometric cross section of the plastic scintillator as it moves off-axis). The results of the profile measurements are shown in Figure 4.6. The beam profile was

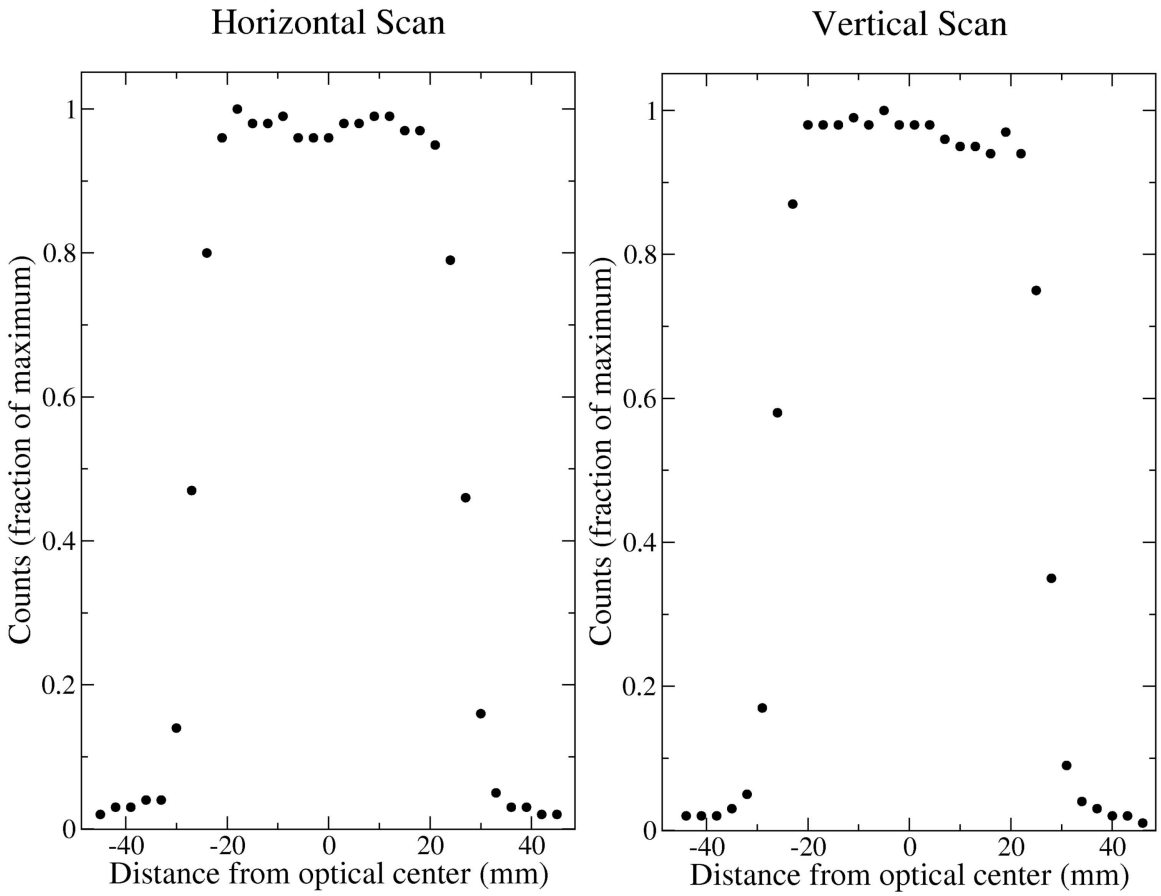

Figure 4.6: Neutron beam profile scan at target position.

measured in 3 mm steps in the horizontal and vertical directions from the optical center. As the figure shows, the beam is very well defined and drops off sharply at the edges, making it possible to safely position detectors very close to the beam.

Additional profile measurements were taken for various deuteron beam tunes. For significant changes in the tune, measurable differences in the beam profile were observed. Such differences are particularly significant when the target size is comparable in size to the flat region of the beam profile. As a result, efforts were made to maintain a similar tune throughout the experiment.

4.3 Experimental Setup

A schematic of the experimental setup is shown in Figure 4.7. The collimated, pulsed beam of monoenergetic neutrons is incident on a target located at the pivot point of the detector array. Gamma rays emitted from the targets are measured using a set of clover and planer HPGe detectors, each equipped with a bismuth germinate (BGO) suppression shield and NaI nose cone. The detectors are mounted on movable stands that rotate about the target position in the horizontal plane and allow measurements at lab angles ranging from 0° to 140°. Additionally, the standss can move radially, allowing the front face of the detector to be positioned between 0 and 26 cm from the target. Two different targets were used for this experiment: a 6.8583 g rectangular ^{238}U foil (3.65 cm x 5.20 cm x 0.02 cm) and a 1.57 g rectangular ^{235}U foil (2.60 cm x 2.60 cm x 0.013 cm). Both targets were backed by rectangular foils of 99.5% pure natural iron foils of thickness 0.0038 cm and 0.01 cm respectively. For the purposes of this experiment, the detector shields served only as passive shielding. A variety of detector combinations and positions were utilized during the course of this experiment and can be found in Tables 4.2 and 4.3.

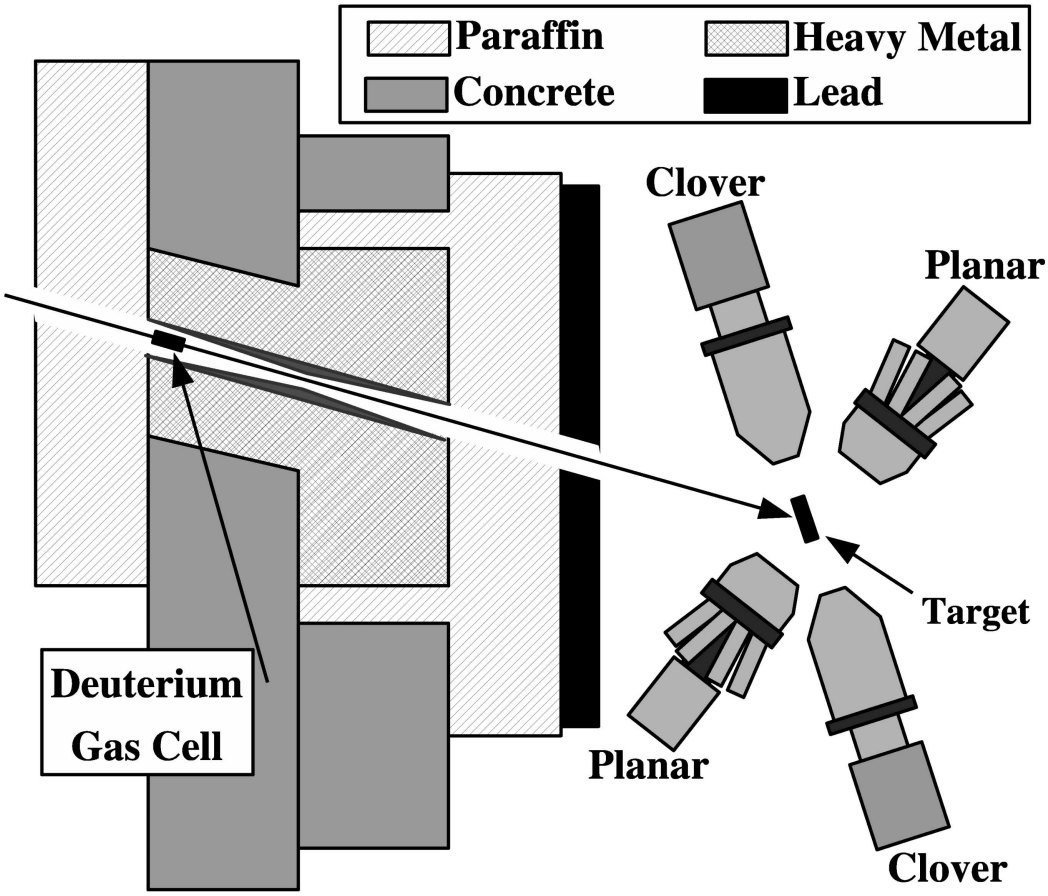

Figure 4.7: Shielded neutron source area (SNSA) setup.

E_n (MeV)	Detector type	Angles w.r.t beam axis	Distance to target
8(a)	Planar	75°	10.1 cm
	Planar	115°	10.1 cm
	Clover	45°	16.0 cm
	Clover	135°	15.6 cm
8(b)	Planar	59°	12.3 cm
	Planar	125°	14.0 cm
	Clover	55°	14.6 cm
	Clover	141°	18.6 cm
10(a)	Planar	115°	10.9 cm
	Clover	45°	16.6 cm
	Clover	135°	14.8 cm
10(b)	Planar	59°	13.0 cm
	Planar	125°	13.7 cm
	Clover	55°	14.2 cm
	Clover	141°	18.6 cm
11	Planar	75°	10.1 cm
	Planar	115°	10.1 cm
	Clover	45°	16.0 cm
	Clover	135°	15.6 cm
12(a)	Planar	75°	10.1 cm
	Planar	115°	10.1 cm
	Clover	45°	16.0 cm
	Clover	135°	15.6 cm
12(b)	Planar	59°	13.0 cm
	Planar	125°	13.7 cm
	Clover	55°	14.2 cm
	Clover	141°	18.6 cm
14	Planar	75°	10.1 cm
	Planar	115°	10.1 cm
	Clover	45°	16.0 cm
	Clover	135°	15.6 cm

Table 4.2: Detector configurations used for ^{235}U measurements.

E_n (MeV)	Detector type	Angles w.r.t beam axis	Distance to target
5	Planar	133°	16.9 cm
	Planar	45°	18.1 cm
	Clover	95°	14.7 cm
6	Clover	125°	20 cm
	Planar	90°	10 cm
8	Planar	90°	9.1 cm
	Clover	90°	11.1 cm
10(a)	Planar	115°	10.9 cm
	Clover	45°	16.6 cm
	Clover	135°	14.8 cm
10(b)	Planar	63°	8.2 cm
	Clover	90°	11.2 cm
12	Planar	133°	16.9 cm
	Planar	45°	18.1 cm
	Clover	95°	14.7 cm
14	Planar	90°	9.1 cm
	Clover	90°	11.1 cm

Table 4.3: Detector configurations used for ^{238}U measurements.

4.4 Detectors

All detectors used to measure gamma rays were semiconductor diode detectors composed of high-purity germanium. This form of detector is described quite well in *Radiation Detection and Measurements* by Glenn F. Knoll [60]. Unlike a conductor in which electrons may move freely through the material, electrons in a semiconductor must overcome a bandgap between the materials valence and conduction bands in order to migrate through the crystal. Unlike insulators, the bandgap in a semiconductor is small, typically about 4 eV or less. In germanium, this bandgap is 0.7 eV. Any electron that is promoted to the conduction band leaves behind a hole in the valence band practically equivalent to a positively charged particle. In the absence of an electric field, the electron-hole pairs eventually recombine. In a pure semiconductor, the number of free electrons must be equal to the number of holes. However, in

practice, there are always impurites present in a semiconductor material, and these impurities can provide either extra conduction electrons or extra holes. The former case, where the electrons are the majority charge carriers, is referred to as an n-type semiconductor, while the latter is called a p-type semiconductor. It can be shown that, if a junction is created between an n-type and p-type semiconductor, conduction electrons and holes will diffuse across the junction from regions of high concentration to low and create a depletion region. If the density of majority charge carriers in the n-type material equals that in the p-type, the depletion region extends symmetrically into both materials. In practice, however, one material has a lower majority charge density than the other, and the depletion region extends farther into that material. In this depletion region, an electric field exists that sweeps any electrons created in the junction toward the n-type material and any holes created toward the p-type material. The concentration of free charges in this region is therefore depleted (hence the name), and any electron-hole pairs created by photons interacting with the material via photoelectric absorption, Compton scattering, or pair production produce an electric current that is easily detected. In order to measure penetrating radiation such as gamma rays effectively, it is advantageous to make this depletion region as large as possible. This can be achieved by applying a reverse voltage bias across the junction which enhances the electric field present in the region and by lowering the impurity doping level in one material with respect to the other. The width d of the depletion region can then be shown to be:

$$d = (\frac{2\epsilon V}{eN})^{\frac{1}{2}}, \tag{4.1}$$

where ϵ is the dielectric constant of the material, V is the applied reverse bias, e is the electronic charge, and N is the net impurity concentration in the material of low dopant concentration. For very low N, the depletion region extends almost completely into the bulk material, and thus the material with high dopant concentration

(referred to as the rectifying material) can be made quite thin.

There are two main methods for achieving a low net impurity concentration in germanium. The first is to compensate for the impurities by adding an equivalent amount of dopants of the opposite type. The process of lithium ion drifting has been developed to create compensated materials this way [61]. While the impurity concentration cannot in practice be exactly balanced, the net impurity level can be made quite low. However, lithium ion drifted materials must be maintained at low temperatures in order to prevent lithium precipitation. The second method involves creating ultrapure germanium crystal [62]. Germanium is locally heated to produce a molten zone which is passed from one end of the material to the other. Impurities, which are more soluble in liquid germanium than solid, pass into the molten zone and are transferred to one end of the crystal which is then removed. Unlike lithium drifted materials, high-purity germanium may be allowed to warm to room temperature between uses and is thus operationally more convenient.

Because of the relatively small bandgap in germanium, electrons promoted to the conduction band by thermal energy at room temperature produce a large noise current. In order to maintain good energy resolution, the crystal must be operated at a much lower temperature. This is achieved by maintaining thermal contact between the germanium and an insulated dewar of liquid nitrogen.

The main advantage of using germanium detectors for gamma-ray spectroscopy is the energy resolution. Resolutions of around 0.1-1% are capable with germanium detectors compared with 5-10% for NaI(Tl) scintillator detectors. The improved gamma-ray energy separation provided by this energy resolution is very important for targets with complicated decay schemes in which many gamma rays may be emitted.

Among the drawbacks of semiconductor diode detectors is the susceptibility of the

detector to radiation damage. Nonionizing transfers of energy to the atoms of the semiconductor can lead to defects in the crystal lattice that can trap charge carriers and lead to an increase in signal noise and the degregation of energy resolution. This damage is relatively minor for gamma rays or beta particles but can be quite significant for fast neutrons or heavy charged particles. For this reason, great care must be taken to shield the crystal from radiation damage in order to maintain the integrity of the detector.

The linear charge pulse obtained from a germanium crystal is generally too small to be effectively processed without preliminary amplification. For this reason, all germanium detectors used in this experiment were equipped with preamplifiers (commonly shortened to preamps) capable of converting the linear charge pulse from the germanium crystal into a linear tail pulse with amplitudes that are typically on the millivolt scale and decay time on the order of 50 μs. It is this tail pulse that is processed by the detection electronics described in Section 4.5.

4.4.1 Planar Detectors

Gamma rays in the 50-300 keV energy range were measured using ORTEC planar HPGe detectors. A schematic of a planar detector configuration is shown in Figure 4.8. A thin high-purity germanium disk is sandwiched between heavily doped n^+- and p^+-type contact surfaces. Depending on the type of the bulk germanium disk, one contact serves as a rectifying agent while the other suppresses leakage current due to minority carrier motion. The planar detectors used in this experiment had an active diameter of 38 mm and a thickness of 13 mm. A thin beryllium window (0.25 mm) in front of the crystal maintained the vacuum around the crystal while minimizing the attenuation of gamma rays entering the detector.

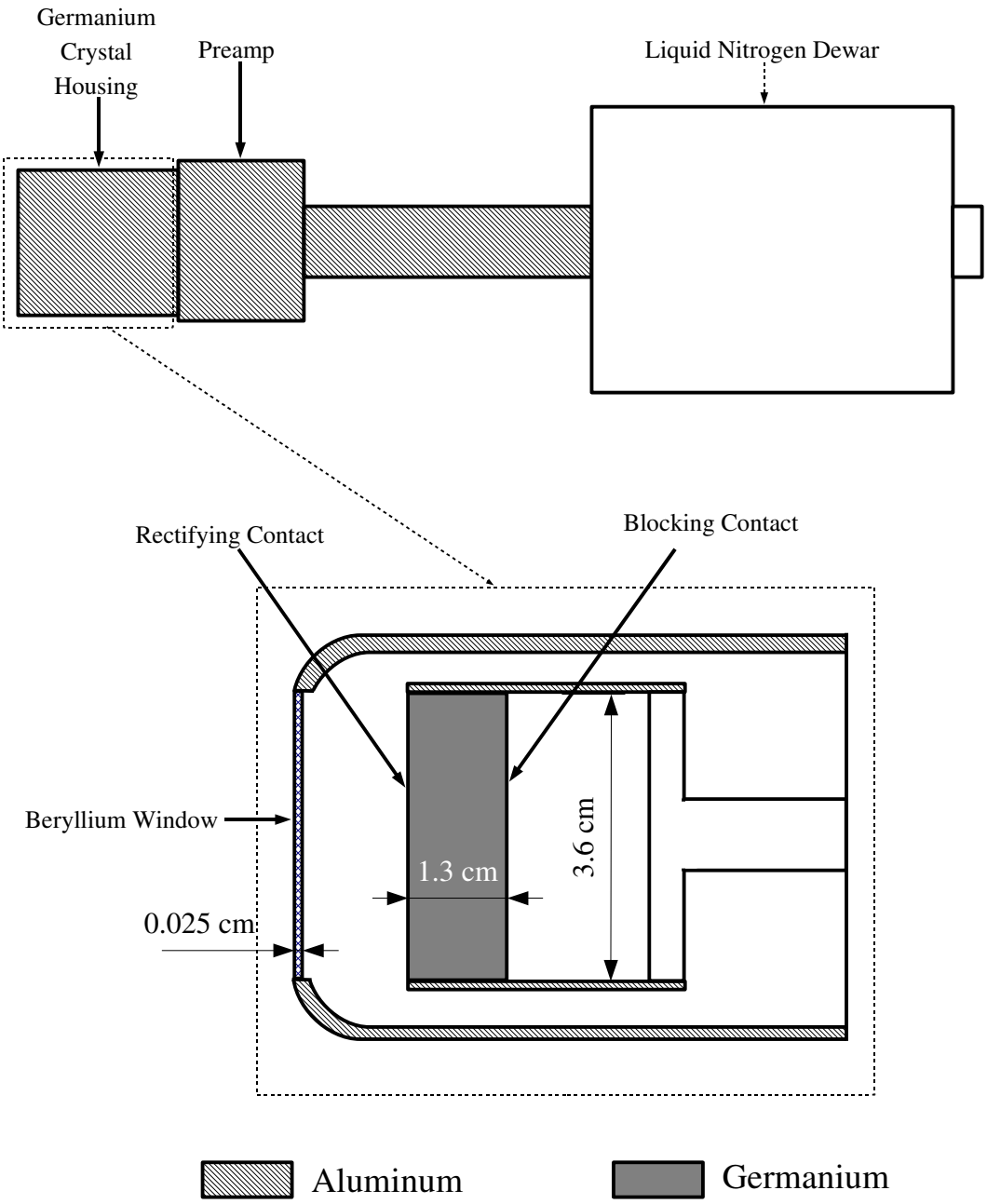

Figure 4.8: Schematic of HPGe planar detector.

4.4.2 Clover Detectors

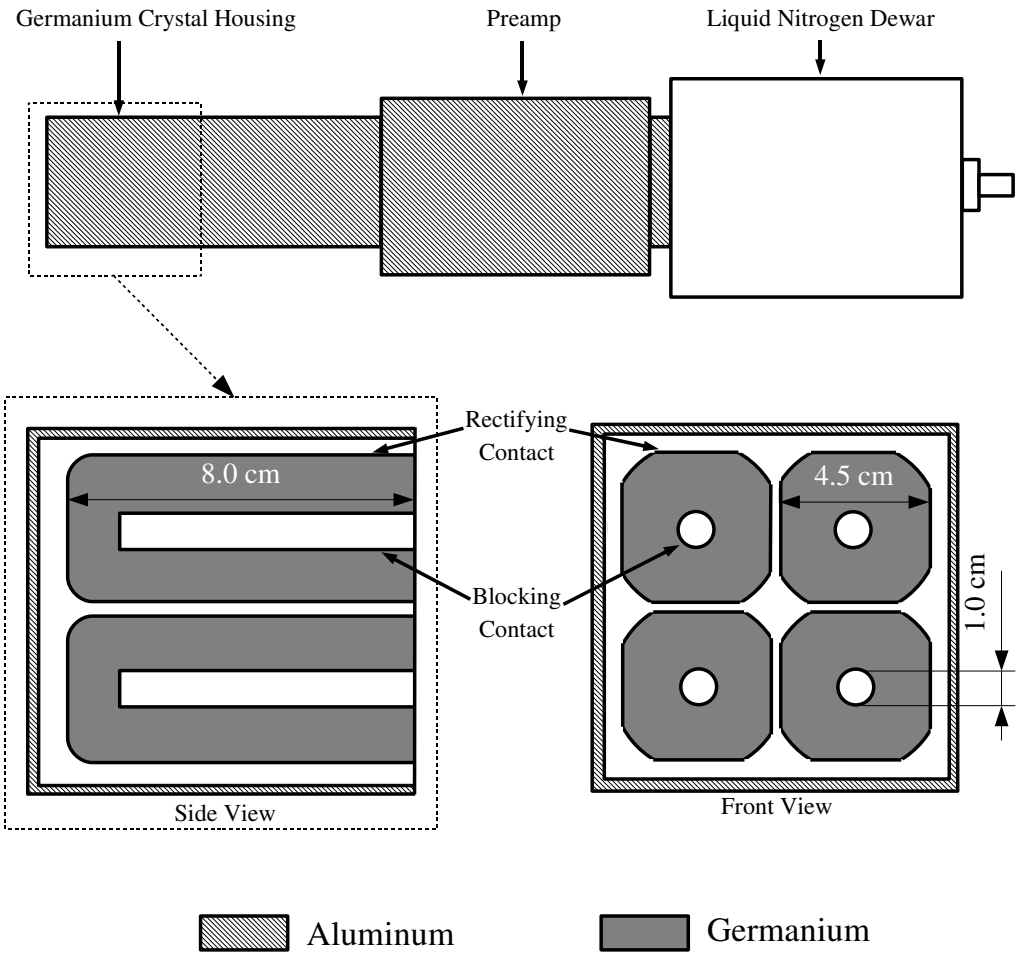

Figure 4.9: Schematic of HPGe clover detector.

Gamma rays between 300 and 2000 keV were measured using Canberra segmented clover HPGe detectors. The configuration of these detectors is shown in Figure 4.9. Four bulletized coaxial germanium crystals with a diameter of 5.0 cm and length of 8.0 cm are arranged in a clover orientation with a crystal separation of 0.6 mm. The rectifying contact is fabricated on the outer surface of each crystal while the inner cylindrical contact is made by drilling out the core of the crystal and placing

a blocking contact on the inner surface. It is important for the outer contact to be the rectifying one as the depletion region will then grow inward as voltage is applied and will require less reverse bias to be fully depleted than if it had to grow from the inside out. Each crystal can operate as a separate detector and thus allowed a single clover detector to account for two independent measurements each of two separate angular positions.

4.5 Detection Electronics and Data Acquisition

Output signals from germanium detectors consist of linear charge pulses in which information about the detected gamma ray is carried in the amplitude of the pulse. This linear pulse is not immediately useful for analytical purposes and must be converted to a more accessible form with the use of detection electronics. Electronics standards such as NIM (Nuclear Instrumentation Module) and VME (VERSAmodule Eurocard) allow for the construction of signal processing electronics that can manipulate linear analog pulses from detectors to obtain energy and timing information in a way that is easily reproducible.

A simplified detection electronics scheme is shown in Figure 4.10. The linear tail pulse signals from the detectors preamp are fed into a linear amplifier module which allows adjustments to pole zero in order to eliminate tail pileup. The amplified outputs of this module are shaped Gaussian signals with shaping time adjusted to maximize signal-to-noise in order to preserve good energy resolution. The amplified signals are sent to a 12-bit analog-to-digital converter (ADC) which integrates the pulses and outputs digital values that can be read into the data-acquisition system to provide an energy spectrum of detected gamma rays.

A direct, unamplified output from the linear amp is fed into a timing filter amplifier (TFA) which produces an amplified fast linear output which is sent to a constant

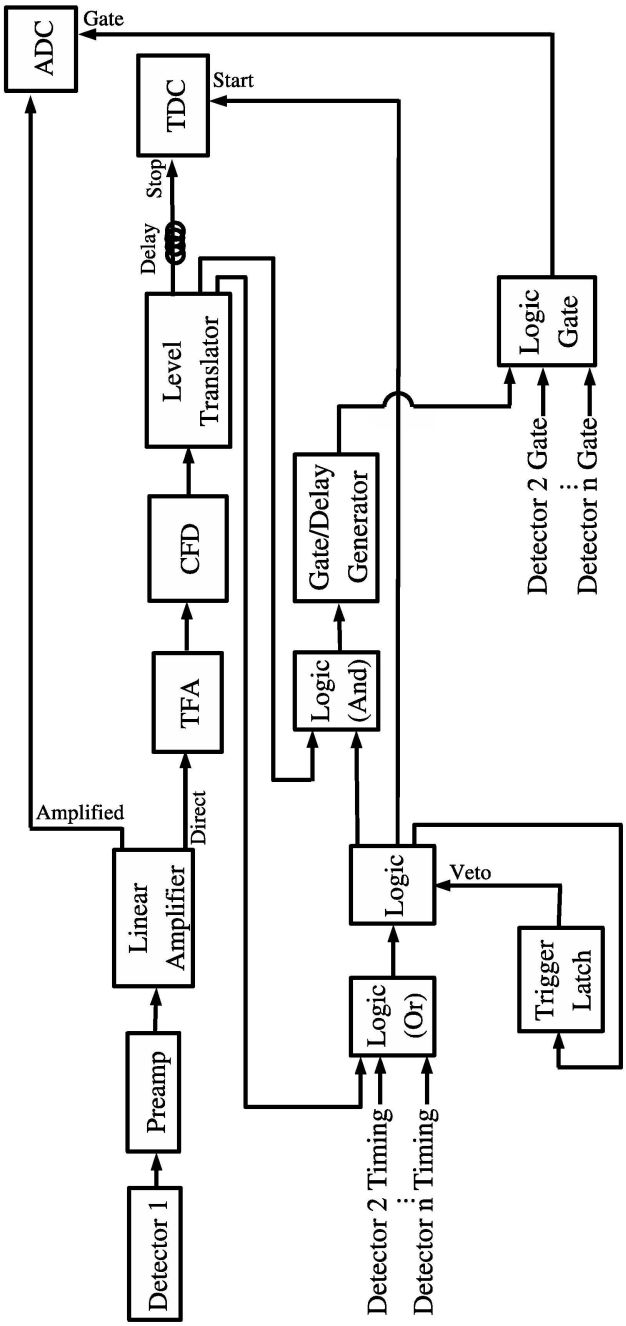

Figure 4.10: Simplified detection electronics scheme.

fraction discriminator (CFD). The CFD outputs a logic signal for pulses with amplitudes that exceed a preset threshold level. The logic signal is then sent to a level translator where it is fanned out to three separate outputs. The first output is sent through some delay (typically around 200 ns) before being sent to a time-to-digital converter (TDC). A TDC converts the difference between start and stop pulses into a digital value that can be read into the data-acquisition system to provide a timing spectrum for detected gamma rays. The delayed signal acts as a stop signal. The second output from the level translator is sent to a logic module with the CFD outputs from the other detectors to form a logical OR signal referred to as the master gate signal. This master gate signal is then sent to the logic unit of the veto system. If the signal does not encounter a busy signal, a logic signal referred to as the master gate live signal is sent to a specialized trigger latch module which signals the I/O module to begin readout. The amount of time necessary for the computer to acknowledge event readout is around 3 μs. Once the computer acknowledges event readout, a second signal is sent from the I/O module to the latch module to produce a veto busy signal which inhibits further master gate live signals until event readout is complete, at which time the latch is opened. The time required to complete event readout varies but was typically found to be around 45 μs for this experiment. A copy of successful master gate live signals is sent to the TDC to act as a start signal. A second copy is sent to a logic unit to form a logical AND with a third output from the level translator. The output from this logic unit is sent to a gate/delay generator to produce a gate signal which is then sent to a logic gate unit to form a logical AND with gate signals from the other detectors. The signal produced by this unit is sent to the gate input of the ADC. This gate signal ensures that only events which have the proper timing and which do not occur while the computer is busy will be read into the ADC.

This experiment utilized the Spectrodaq/SpecTCL data-acquisition program developed at National Superconducting Cyclotron Laboratory at Michigan State University. Events are read into event files which are saved to disk, enabling offline analysis at a later time. In addition, real time 1- and 2-dimensional histograms of incoming data may be viewed during data acquisition. Event files produced during an hour of data acquisition were generally on the order of 500 Mb in size.

Chapter 5

Data Analysis

Data obtained from SpecTCL was histogramed in 2 x 2 matrices of energy versus time-of-flight spectra for each detector in ASCII format. These matrices were then converted to line compressed format and analyzed using the Tv spectra- and matrix-analysis program [63]. Typical γ-ray spectra produced in these measurements contain hundreds of peaks resulting from natural background radiation, neutron-induced reactions in detection and shielding materials, and natural decay of the uranium targets as well as from prompt neutron-induced reactions of interest in the target. In the following sections, the process of identifying the neutron-induced peaks of interest will be considered before moving on to the discussion of the extraction of partial cross sections from peak yields.

5.1 Time-of-Flight Technique

Prompt neutron-induced events were differentiated from accidental background events as well as events resulting from γ rays and break-up neutrons produced in the deuterium gas cell using time-of-flight techniques. For neutrons with kinetic energy E_n, the neutron velocity v_n can be calculated classically as

$$v_n = \sqrt{\frac{2E_n}{m_n}}, \tag{5.1}$$

where $m_n \approx 939.565$ MeV is the neutron rest mass. (A classical calculation of the neutron velocity is reasonable since, for the cross section measurements discussed in this dissertation, $E_n << m_n c^2$.) Therefore, for a flight path distance d, the time of

flight Δt of a neutron relative to a γ ray emitted from the same source is given by

$$\Delta t = \frac{d}{v_n} - \frac{d}{c} = \frac{d}{c}\left(\sqrt{\frac{m_n c^2}{2E_n}} - 1\right), \tag{5.2}$$

where the speed of light $c \approx 3 \times 10^8 \frac{\mathrm{m}}{\mathrm{s}}$. An example time-of-flight spectrum for clover data is shown in Figure 5.1. Time-of-flight spectra are generated by the TDC where the start signal is provided by an event in the detector while the stop signal comes from a delayed signal from a capacitive pickoff unit located just before the deuterium

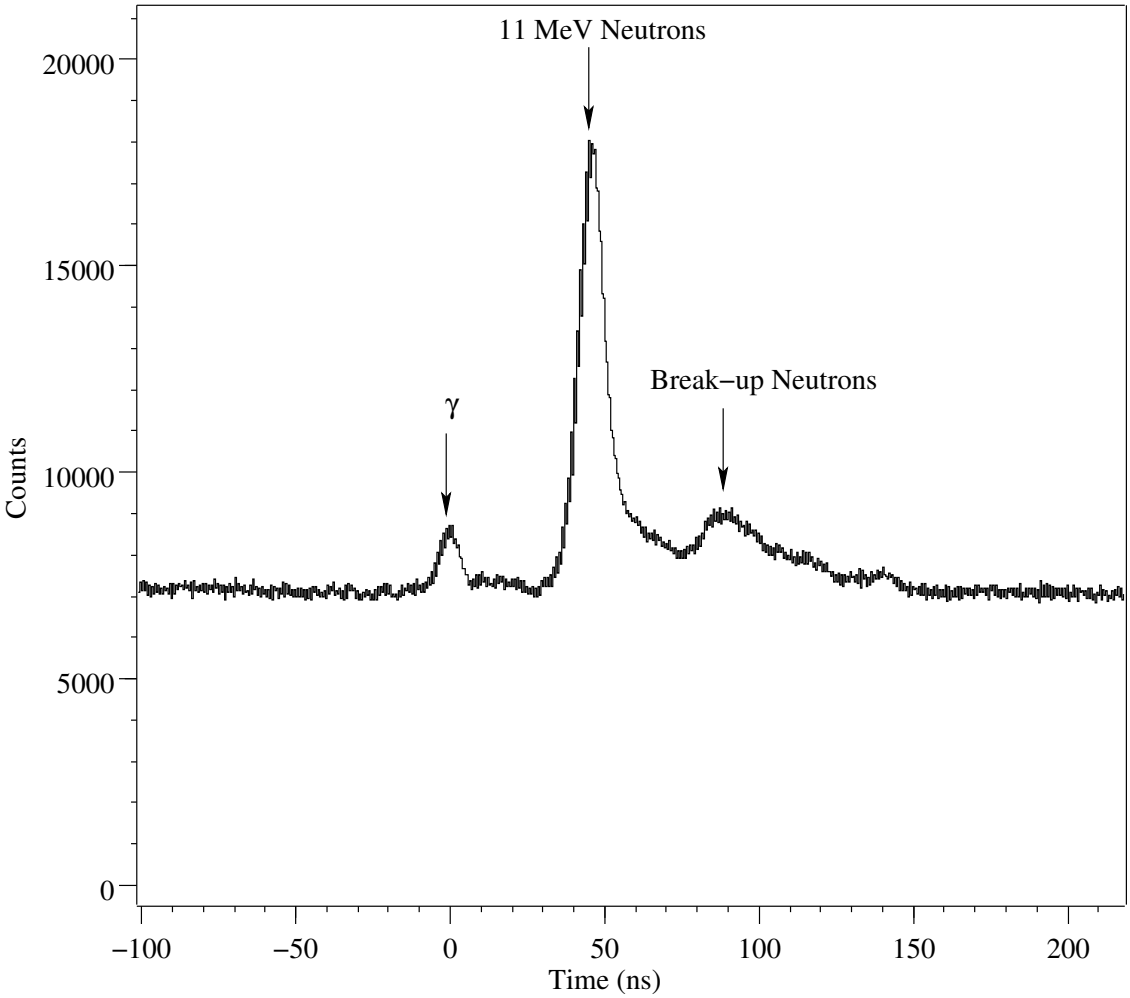

Figure 5.1: Time-of-flight spectrum with clover detector for 11 MeV neutrons. Time is relative to γ-ray peak.

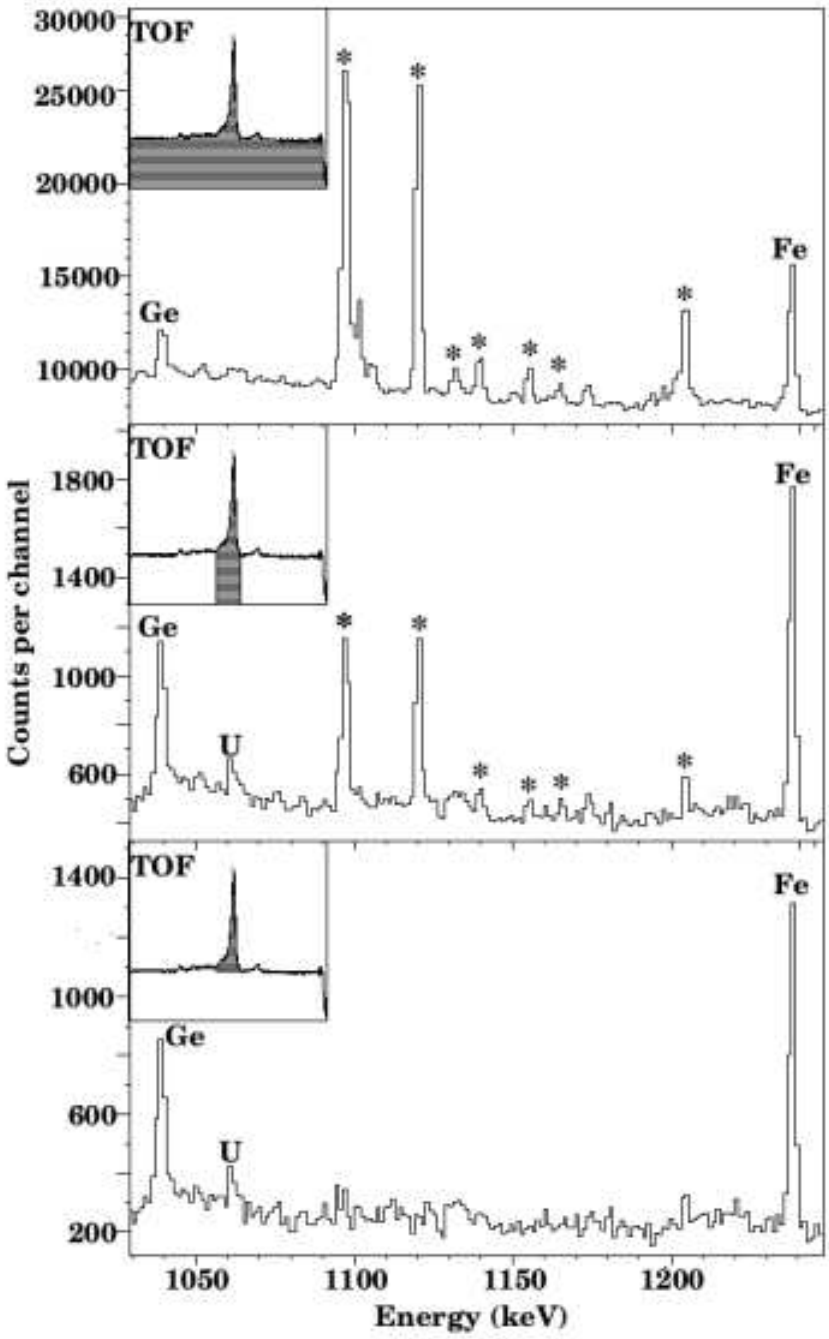

Figure 5.2: Clover detector γ-ray spectra for a ^{238}U/^{56}Fe sample irradiated with 10 MeV neutrons with different time-of-flight cuts. Accidental background peaks are labeled with asterisks.

gas cell. Events not time-correlated with neutron beam pulses appear as a flat background in the time spectrum. Beam-correlated events appear as prompt peaks above the flat background with the full width at half maximum (FWHM) dominated by the timing resolution of the detector ($\sim$ 10 ns for germanium detectors). Timing gates are placed around the monoenergetic neutron peak and, separately, around an equal number of channels in the flat accidental background area before the γ-ray peak (where no beam-correlated events can take place) to produce "prompt" and "accidental" γ-ray spectra which can be subtracted to remove accidental background peaks. Figure 5.2 demonstrates the process of accidental background subtraction using time-of-flight cuts.

5.2 Energy Calibration

Gamma-ray spectra were energy calibrated in Tv using standard gamma-ray sources with peaks of well-known energy. A linear fit to source peaks was performed to produce a global calibration for each detector; example fits for clover and planar detectors are shown in Figures 5.3 and 5.4, respectively. Individual calibrations were performed for each incident neutron energy in order to compensate for small variations in amplifier gain between runs. Calibration sources used and the residual of the linear fit to the accepted energies of source peaks are listed in Tables 5.1 and 5.2 for clover and planar detectors, respectively.

5.3 Peak Identification

Time-of-flight techniques described in Section 5.1 help simplify the task of peak identification by removing peaks resulting from accidental background; however, due to the short flight path between the detectors and target (typically $\sim$ 10-15 cm), these techniques are unable to distiguish between γ rays emitted from the target and

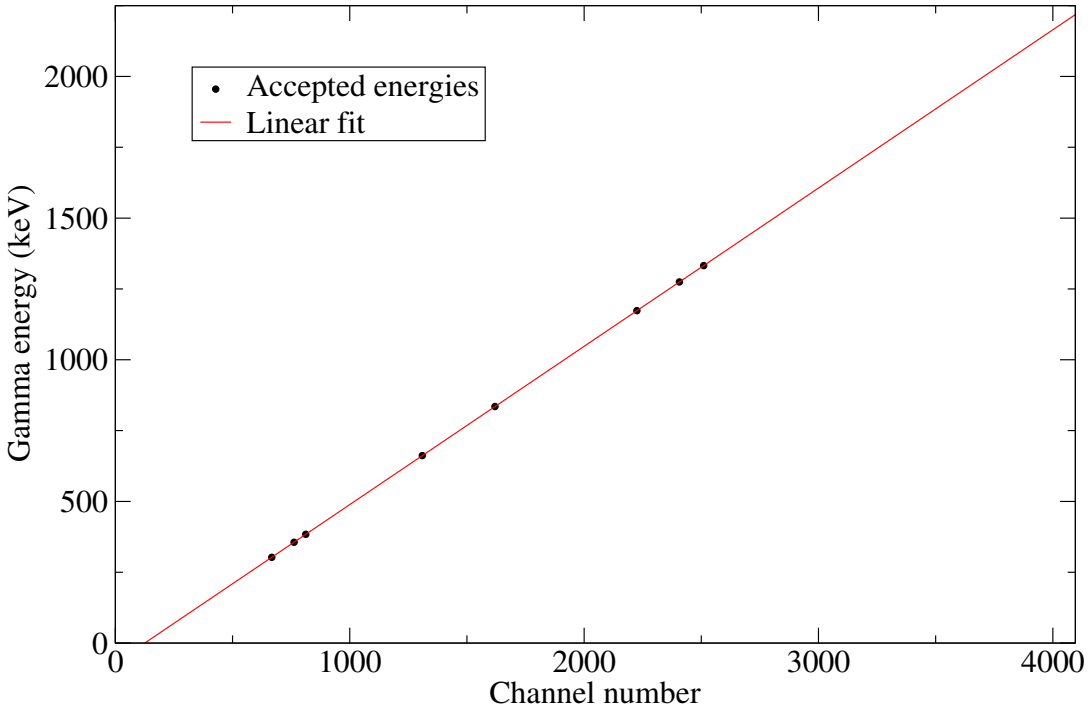

Figure 5.3: Energy calibration fit for clover detector.

Source	Channel number	E_γ^{acc} (keV)	E_γ^{fit} (keV)	$E_\gamma^{acc} - E_\gamma^{fit}$ (keV)
^{133}Ba	667.35	302.85	302.85	-0.004
^{133}Ba	762.48	356.01	356.00	0.007
^{133}Ba	812.29	383.85	383.83	0.017
^{137}Cs	1309.61	661.66	661.68	-0.023
^{54}Mn	1619.57	834.85	834.86	-0.008
^{60}Co	2225.21	1173.23	1173.23	-0.002
^{22}Na	2406.55	1274.54	1274.55	-0.007
^{60}Co	2510.24	1332.49	1332.47	0.015

Table 5.1: Standard source peaks used for energy calibration in clover detectors.

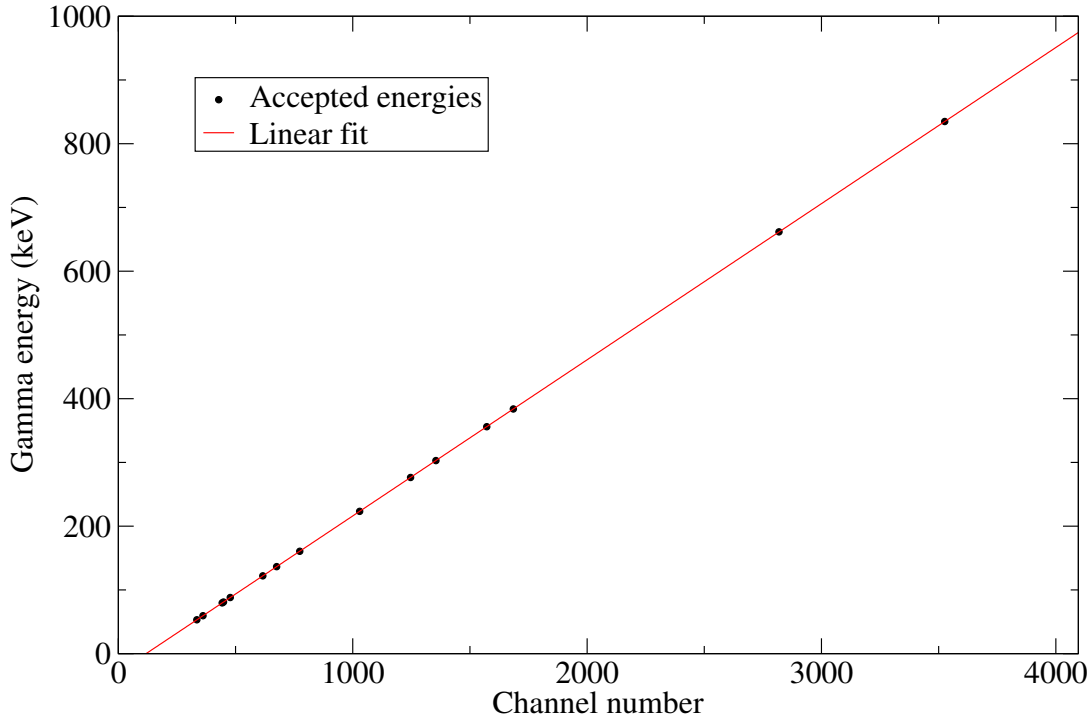

Figure 5.4: Energy calibration fit for planar detector.

Source	Channel number	E_γ^{acc} (keV)	E_γ^{fit} (keV)	$E_\gamma^{acc} - E_\gamma^{fit}$ (keV)
^{133}Ba	334.93	53.16	53.10	0.059
^{241}Am	361.02	59.54	59.49	0.047
^{133}Ba	443.02	79.61	79.53	0.029
^{133}Ba	448.63	81.00	80.95	0.046
^{109}Cd	477.39	88.03	88.00	0.029
^{57}Co	616.37	122.06	122.05	0.012
^{57}Co	675.21	136.47	136.46	0.008
^{133}Ba	773.87	160.61	160.63	-0.019
^{133}Ba	1029.58	223.24	223.27	-0.031
^{133}Ba	1246.72	276.4	276.47	-0.065
^{133}Ba	1354.82	302.85	302.95	-0.098
^{133}Ba	1571.84	356.01	356.11	-0.101
^{133}Ba	1685.31	383.85	383.91	-0.059
^{137}Cs	2818.68	661.66	661.55	0.107
^{54}Mn	3525.96	834.85	834.82	0.032

Table 5.2: Standard source peaks used for energy calibration in planar detectors.

γ rays induced by fast neutrons scattering off the uranium target into detector or shielding material. Therefore, special care must be taken to identify these detector- and shielding-associated events. Two different techniques were employed to map these peaks. First, spectra obtained for ^{235}U and ^{238}U were compared for the same detector, configuration, and neutron energy. Because the two uranium targets are similar in mass and size, the neutron flux scattered from the targets into the detectors should be similar. Due to the different level scheme of the two target nuclei, however, γ rays emitted from the target should stand out when the two spectra are compared. These peaks were compared with the accepted energies of γ rays emitted from materials known to be present in the detectors and shields (^{70,72,74}Ge, ^{209}Bi, ^{27}Al, etc.). An example comparison of these spectra for incident neutron energy $E_n = 10$ MeV is given in Figure 5.5. Second, spectra were analyzed for "empty target" runs where the beam was on but no target was present. Due to the absence of the heavy uranium scatterer, neutron fluxes into the detector were considerably lower, resulting only from neutrons scattering from air or possibly escaping through small cracks in the shielding wall. Figure 5.6 shows an example "empty target" spectrum obtained from a clover detector for incident neutron energy $E_n = 12$ MeV. A partial list of identified peaks are listed in Table 5.3. No significant peaks resulting from target or shielding material appeared in the low γ-ray energy region measured by the planar detectors ($E_\gamma \approx 50 - 300$ keV).

5.4 Peak Yields

In order to obtain γ-ray yields, peaks were fit in Tv using a Gaussian parametrization with an energy-dependent width. This width parameter was obtained by a linear fit to measured widths from strong γ-ray peaks stemming from natural background radiation. Individual width calibrations were performed for each detector at each

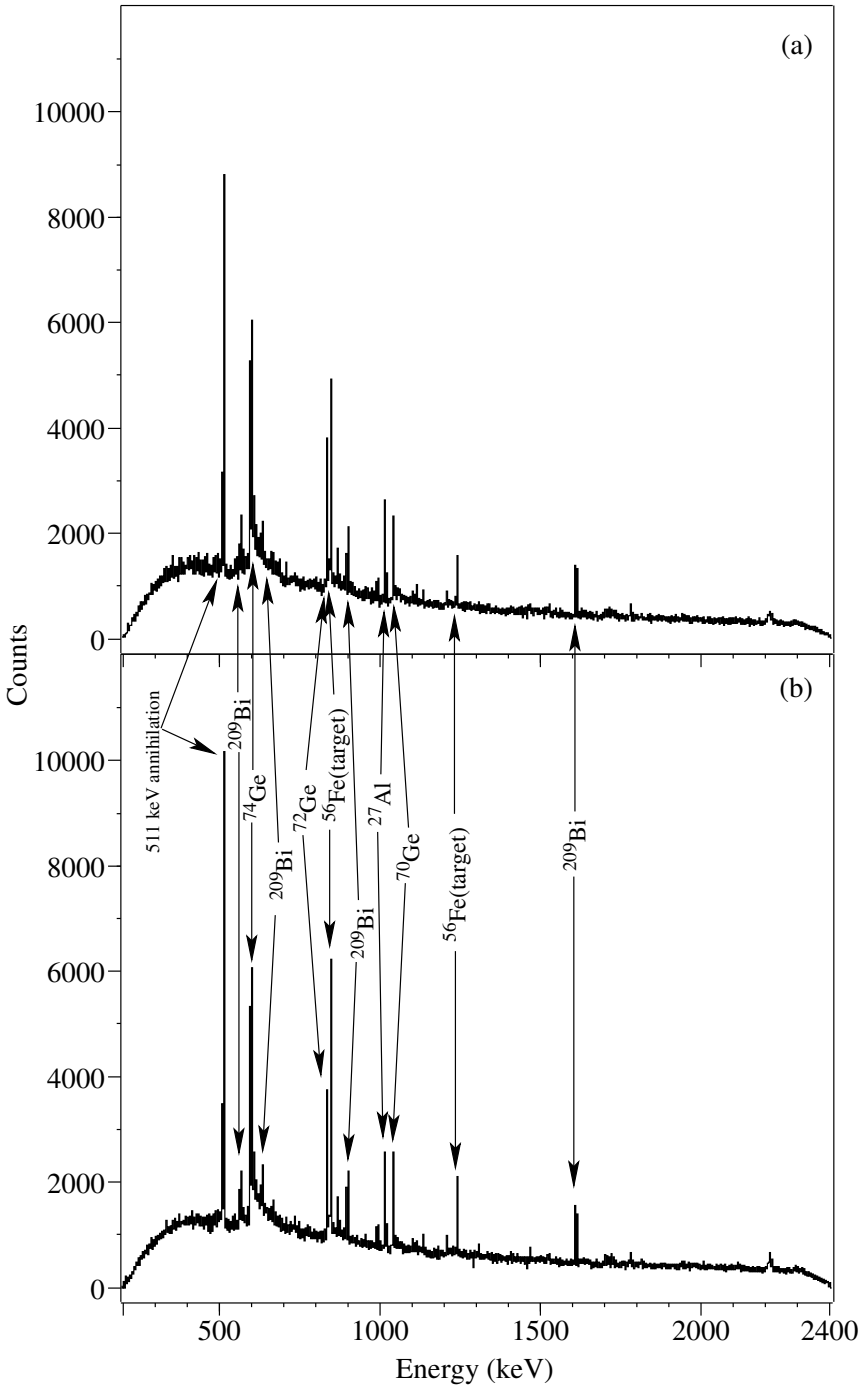

Figure 5.5: Beam-correlated spectra for (a) ^{235}U and (b) ^{238}U for $E_n = 10$ MeV. Prominant peaks found in both spectra are identified by parent nucleus.

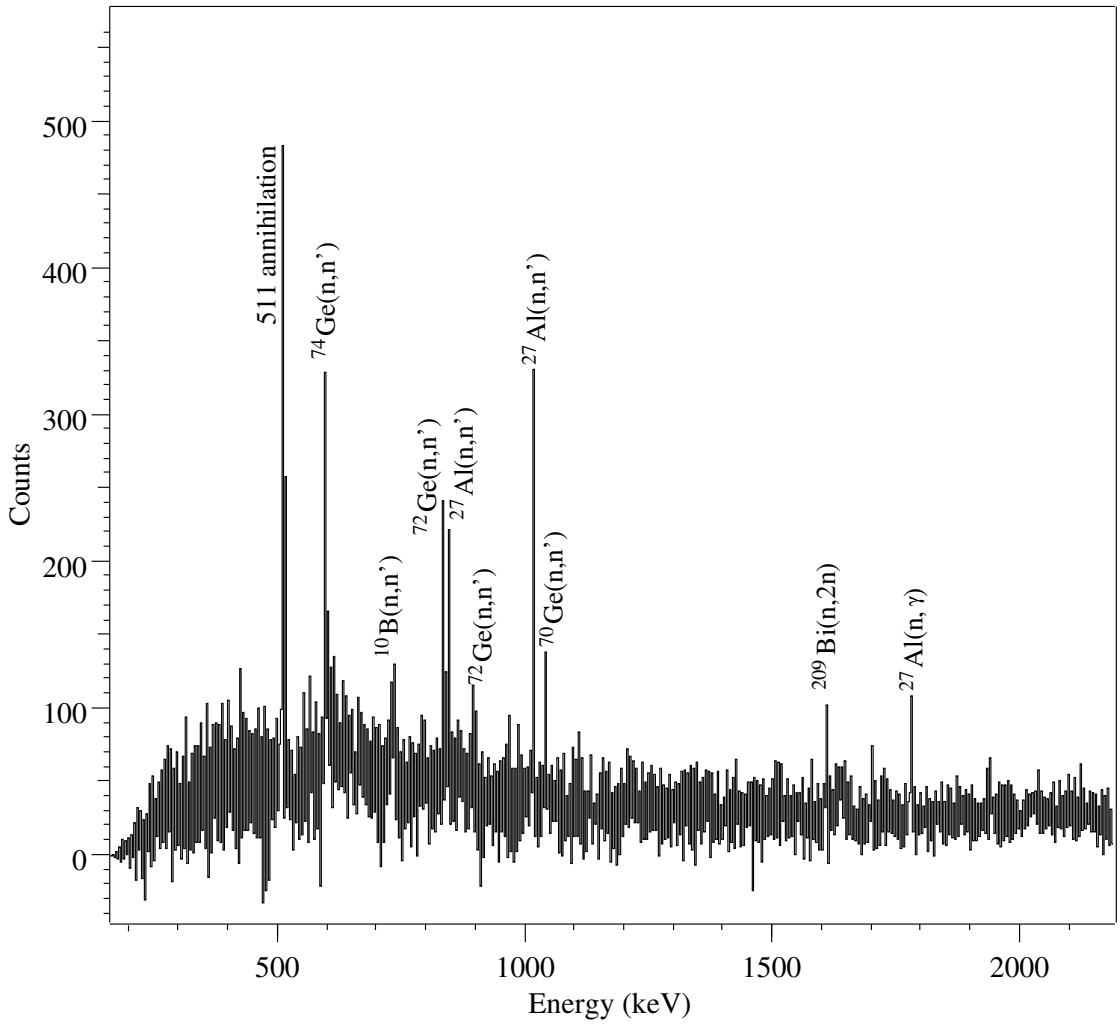

Figure 5.6: Beam-correlated clover spectrum for "empty target" runs for $E_n = 12$ MeV. Beam time was ~ 60 h.

E_γ (keV)	Reaction	E_γ (keV)	Reaction
538.41	^{209}Bi$(n,2n)^{208}$Bi	886.40	^{209}Bi$(n,2n)^{208}$Bi
562.93	^{76}Ge$(n,n')^{76}$Ge	894.26	^{72}Ge$(n,n')^{72}$Ge
565.23	^{209}Bi$(n,2n)^{208}$Bi	896.00	^{209}Bi$(n,2n)^{208}$Bi
569.70	^{207}Pb$(n,n')^{207}$Pb	984.64	^{27}Al$(n,p)^{27}$Mg
595.85	^{74}Ge$(n,n')^{74}$Ge	1006.23	^{209}Bi$(n,2n)^{208}$Bi
601.49	^{209}Bi$(n,2n)^{208}$Bi	1014.42	^{27}Al$(n,n')^{27}$Al
650.60	^{209}Bi$(n,2n)^{208}$Bi	1033.31	^{209}Bi$(n,2n)^{208}$Bi
718.35	^{10}B$(n,n')^{10}$B	1039.49	^{70}Ge$(n,n')^{70}$Ge
803.06	^{206}Pb$(n,n')^{206}$Pb	1094.90	^{209}Bi$(n,2n)^{208}$Bi
823.25	^{209}Bi$(n,2n)^{208}$Bi	1204.21	^{74}Ge$(n,n')^{74}$Ge
834.01	^{72}Ge$(n,n')^{72}$Ge	1609.10	^{209}Bi$(n,2n)^{208}$Bi
843.74	^{27}Al$(n,n')^{27}$Al	1697.94	^{27}Al$(n,p)^{27}$Mg
867.90	^{74}Ge$(n,n')^{74}$Ge	1778.85	^{27}Al$(n,p\beta^-)^{28}$Si
874.41	^{27}Al$(n,\alpha)^{24}$Na	1808.66	^{27}Al$(n,d)^{26}$Mg

Table 5.3: Identified peaks resulting from neutron-induced reactions in detector and shielding material.

incident neutron energy in order to compensate for small variations in energy resolution. Typical Gaussian width parameters are plotted for clover and planar detectors in Figures 5.7 and 5.8 respectively. Background is fit using an nth order polynomial, usually with $n \leq 2$.

5.5 Partial Cross Section Extraction

Once γ-ray peaks were properly identified and yields obtained, partial cross sections could be extracted. The angle-integrated partial cross section is given by

$$\sigma(E_\gamma) = N_\gamma(E_\gamma,\theta)\frac{(1+\alpha)\cdot C_{att}}{\epsilon \cdot N_{target}\cdot \Phi \cdot t \cdot C_{dead}\cdot W(\theta)}, \tag{5.3}$$

where $N_\gamma(E_\gamma,\theta)$ is the peak yield for a γ ray with energy E_γ in a detector positioned at angle θ, α is the internal conversion coefficient, C_{att} is a correction factor accounting for attenuation of the γ ray in the target, $W(\theta)$ is the angular distribution of γ-ray emission defined in Section 2.5.2, ϵ is the absolute efficiency of the detector,

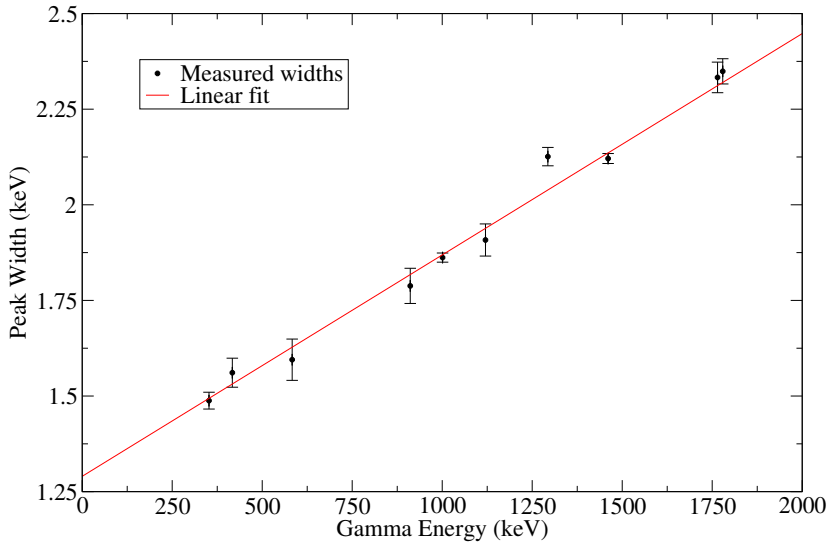

Figure 5.7: Linear fit to measured peak widths for clover detector.

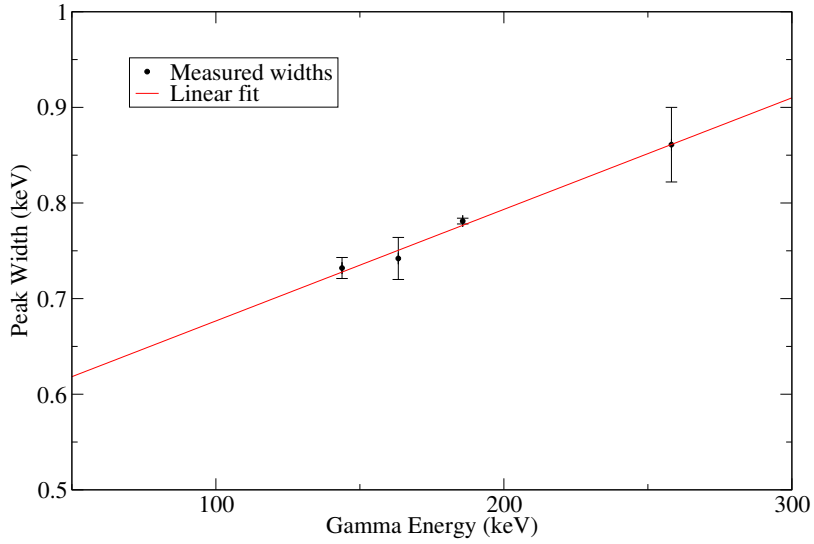

Figure 5.8: Linear fit to measured peak widths for planar detector.

N_{target} is the number of target atoms, t is time of measurement, and C_{dead} is the deadtime-correction factor. Internal conversion coefficients were obtained from the BrIcc internal conversion coefficient database [64]. Other correction factors will be discussed in the following sections.

5.5.1 Detector Efficiency

The absolute efficiency of a γ-ray detector is the ratio of the number of photons recorded in the detector to the number of photons emitted by the source (as opposed to intrinsic efficiency, which is the ratio of photons recorded to the number of photons incident on the detector). Absolute efficiencies for clover and planar detectors were measured using gamma standard calibration sources of about 1 μCi strength with peaks of well-known energy and simulated using the MCNPX Monte-Carlo radiation transport code [65]. Detector efficiencies were measured and modeled for each incident neutron energy in order to account for variations in detector configuration. A sample MCNPX input file is given in Appendix B.1. Measured and modeled absolute efficiencies are shown for a clover and planar detector in Figures 5.9 and 5.10, respectively.

5.5.2 Target Attenuation Correction

Cross sections were corrected for attenuation of γ rays in the target material using MCNPX simulations. The attenuation correction factor is simply the ratio of the number of γ rays emitted from the target nuclei to the number of γ rays that actually escaped the target. That is,

$$C_{att} = \frac{N_{\gamma}^{emitted}}{N_{\gamma}^{escaped}}. \tag{5.4}$$

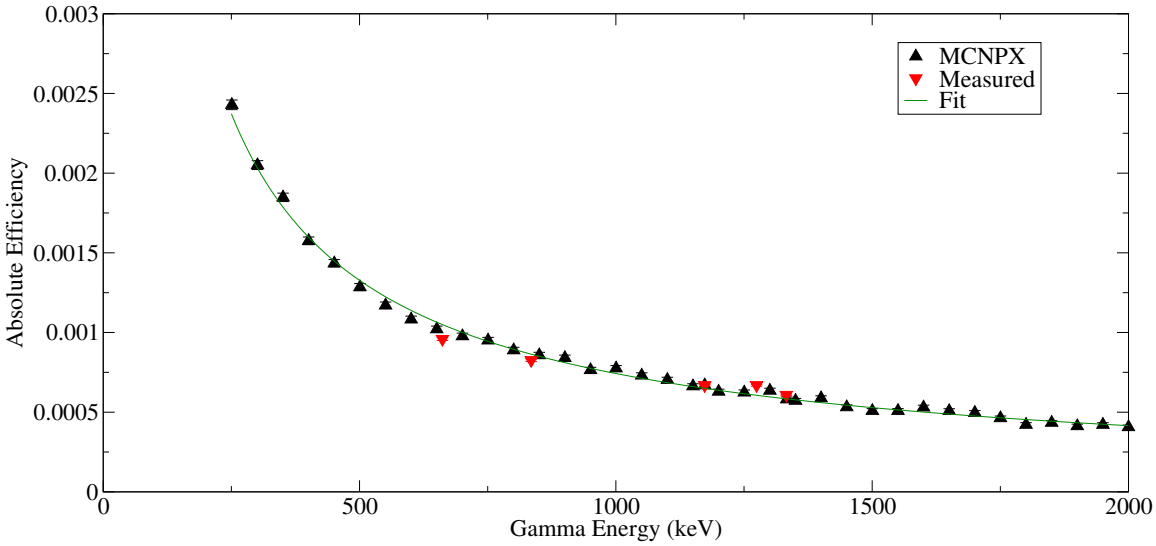

Figure 5.9: Simulated and measured absolute efficiency of full energy peaks for single crystal of a clover detector located 16.0 cm from target position. Data for 250 keV $\leq E_\gamma \leq$ 2 MeV is fit to a power law: $\epsilon(E) = A * E^B$. Efficiency measured using ^{137}Cs, ^{54}Mn, ^{22}Na, and ^{60}Co.

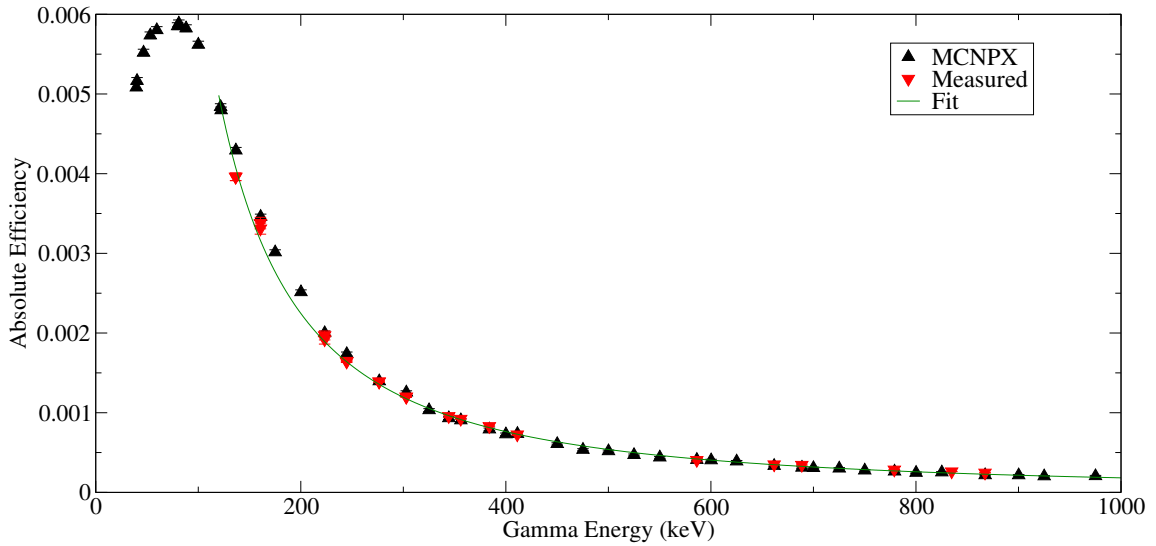

Figure 5.10: Simulated and measured absolute efficiency of full energy peaks for a planar detector located 10.1 cm from target position. Data for 120 keV $\leq E_\gamma \leq$ 1 MeV is fit to a power law: $\epsilon(E) = A * E^B$. Efficiency measured using ^{133}Ba, ^{152}Eu, ^{137}Cs, ^{54}Mn, ^{22}Na, and ^{60}Co.

In order to calculate $N_\gamma^{escaped}$, the uranium/iron target was modeled as an isotropically emitting source of γ rays. $N_\gamma^{emitted}$ was simulated by modeling an identical target except with the composition and density of air. The ratio of the simulated yields from these two cases gave the attenuation correction. Sample MCNPX input files for an uranium and associated air target are given in Appendix B.2.

5.5.3 Deadtime Correction

The deadtime-correction factor C_{dead} accounts for the probability that an event is not recorded due to the system being "busy". The deadtime-correction factor was calculated by taking the ratio of the number of "master gate" events described in Section 4.5 to the number of "master gate live" events. Average deadtimes were calculated to be ∼10-15%.

5.5.4 Angular Distribution Correction

Because of the limited number of detectors used in these measurements, angular distributions could not be accurately obtained simply by fitting the data. Instead, angular distributions were calculated by combining the theoretical framework described in Section 2.5.2 with spin-state orientation parameters obtained from the AVALANCHE code. Optical-model and nuclear level-density parameter inputs for AVALANCHE were obtained from the Reference Input Parameter Library [56].

5.5.5 Flux

Neutron flux was calculated from the measured yields for the 846.77 keV γ ray stemming from the $2^+ \rightarrow 0^+$ transition in ^{56}Fe. Rearranging Equation 5.3, one can solve for the flux:

$$\Phi = \frac{N_\gamma(E_\gamma, \theta)}{\sigma_{Fe}(E_\gamma)} \left(\frac{(1+\alpha) \cdot C_{att}}{\epsilon \cdot N_{target} \cdot t \cdot C_{dead} \cdot W(\theta)} \right). \tag{5.5}$$

Angle-integrated $^{56}\mathrm{Fe}(n, n'\gamma)$ partial cross sections for each incident neutron energy were obtained from the data measured by Nelson *et al.* [66]. Partial cross sections for the 846.77 keV transition are plotted in Figure 5.11. The data was fit to a piecewise

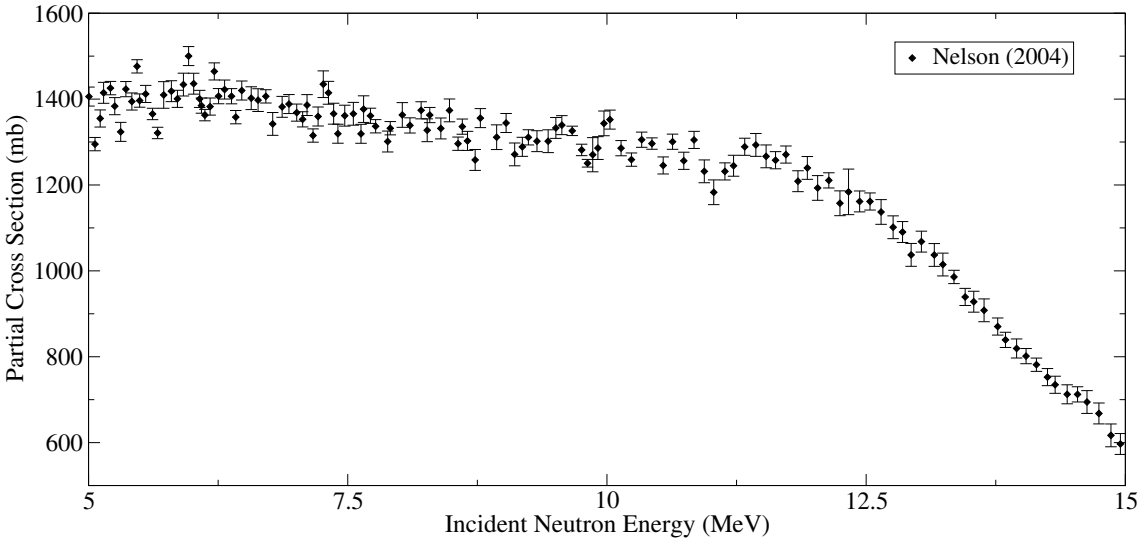

Figure 5.11: Partial cross section for 846.77 keV transition in $^{56}\mathrm{Fe}$ measured by Nelson *et al.* [66].

linear function:

$$\begin{aligned} \sigma &= -23.5707E_n + 1527.46, \quad 5 \text{ MeV} \leq E_n \leq 12 \text{ MeV} \\ \sigma &= -219.854E_n + 3897.35, \quad 12 \text{ MeV} < E_n \leq 15 \text{ MeV}. \end{aligned} \tag{5.6}$$

The average deviation of this fit from measured data was 0.25%; the maximum deviation was 8.03%, which was taken to be the uncertainty of the fit.

Chapter 6

Results

Eleven transitions were observed and partial γ-ray cross sections extracted for ^{235,238}U: seven $^{238}\mathrm{U}(n, n'\gamma)$, two $^{238}\mathrm{U}(n, 2n\gamma)$, and two $^{235}\mathrm{U}(n, 2n\gamma)$ transitions. A list of the observed transitions is given is Table 6.1. Results for calculated angular distributions, measured flux, and extracted cross sections are given in the following sections.

6.1 Angular Distribution

Prior to calculating the angular distribution of γ-ray emission for the observed transitions in uranium, a "proof of concept" test was performed to compare calculated angular distributions for the 846.77 keV γ ray emitted from ^{56}Fe to measured distributions. Measurements were performed using three clover detectors positioned equidistant from a 27.421 g cylindrical ^{nat}Fe target (height: 2.48 cm; diameter: 1.42 cm). Two separate angular configurations were measured, with one clover detector remaining stationary for normalization purposes. By treating individual clover crystals as separate detectors, each clover detector was capable of producing two separate measurements each of two different angles. Measured angular distributions were fit to a sum of Legendre polynomials:

$$W(\theta) = 1 + A \cdot P_2(\cos(\theta)) + B \cdot P_4(\cos(\theta)). \tag{6.1}$$

Measured distributions, Legendre polynomial fits, and AVALANCHE calculations for incident neutron energies of $E_n = 8, 12$ MeV are shown in Figures 6.1 and 6.2, respectively. The maximum deviation of the AVALANCHE curve from the Legendre polynomial fit was 2.62% for $E_n = 8$ MeV and 2.48% for $E_n = 12$ MeV. The average

E_γ (keV)	Reaction	Transition
158.8	$^{238}\mathrm{U}(n,n'\gamma)$	$6^+ \rightarrow 4^+$
211.0	$^{238}\mathrm{U}(n,n'\gamma)$	$8^+ \rightarrow 6^+$
519.5	$^{238}\mathrm{U}(n,n'\gamma)$	$5^- \rightarrow 6^+$
583.6	$^{238}\mathrm{U}(n,n'\gamma)$	$3^- \rightarrow 4^+$
635.2	$^{238}\mathrm{U}(n,n'\gamma)$	$1^- \rightarrow 2^+$
687.0	$^{238}\mathrm{U}(n,n'\gamma)$	$3^- \rightarrow 2^+$
1060.3	$^{238}\mathrm{U}(n,n'\gamma)$	$2^+ \rightarrow 0^+$
121.2	$^{238}\mathrm{U}(n,2n\gamma)$	$\frac{11}{2}^+ \rightarrow \frac{7}{2}^+$
148.6	$^{238}\mathrm{U}(n,2n\gamma)$	$\frac{5}{2}^+ \rightarrow \frac{3}{2}^+$
152.7	$^{235}\mathrm{U}(n,2n\gamma)$	$6^+ \rightarrow 4^+$
244.2	$^{235}\mathrm{U}(n,2n\gamma)$	$10^+ \rightarrow 8^+$

Table 6.1: Observed transitions for which partial γ-ray cross sections were extracted.

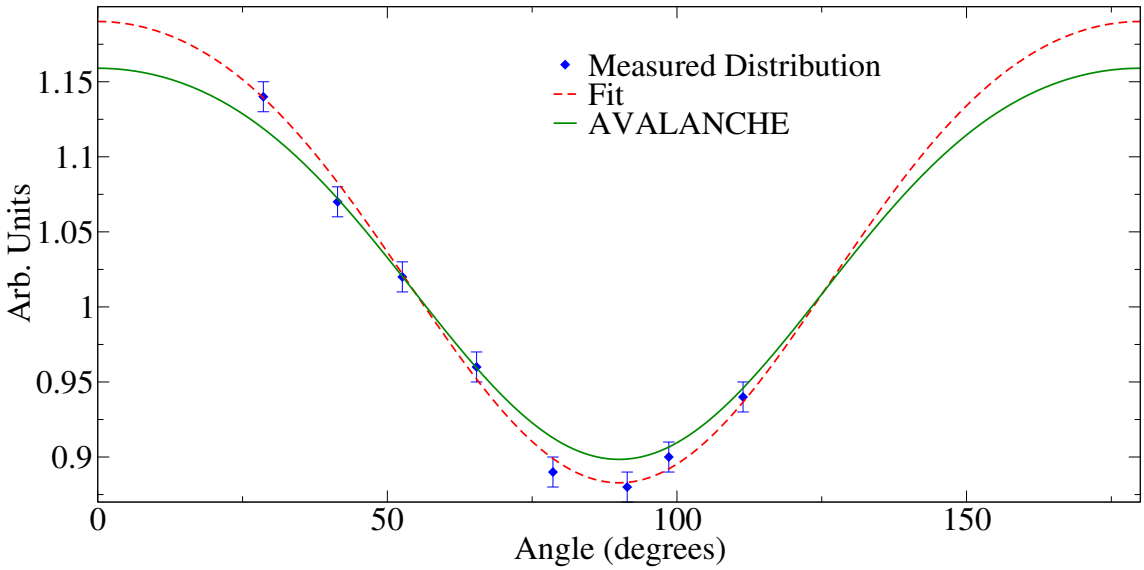

Figure 6.1: Comparison between measured angular distribution, Legendre polynomial fit to data, and AVALANCHE calculations for $2^+ \rightarrow 0^+$ transition in ^{56}Fe for $E_n = 8$ MeV. Angle shown is in the lab frame.

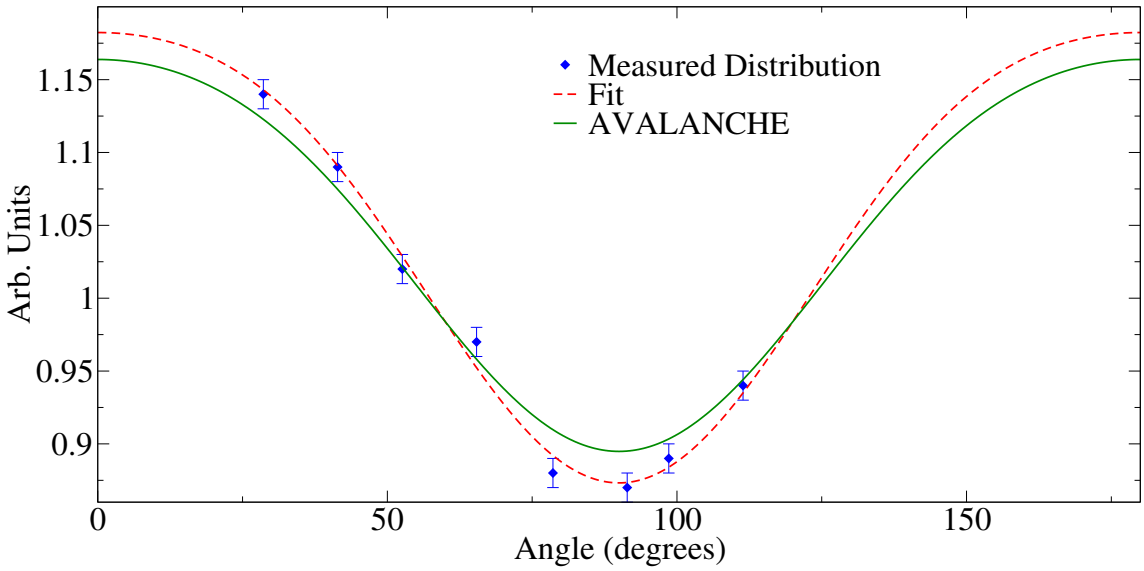

Figure 6.2: Comparison between measured angular distribution, Legendre polynomial fit to data, and AVALANCHE calculations for $2^+ \rightarrow 0^+$ transition in ^{56}Fe for $E_n = 12$ MeV. Angle shown is in the lab frame.

absolute deviation for both incident neutron energies was 1.45%.

Gamma-ray emission angular distributions were then calculated for the observed transitions in ^{235,238}U. The coefficients of the Legendre expansion of the distribution are given in Table 6.2. For transitions with multipolarity $L = 1$, B was taken to be zero.

6.2 Flux

The flux of incident neutrons on target was determined from the yield of 846.77 keV peak resulting from the $2^+ \rightarrow 0^+$ transition in ^{56}Fe using Equation 5.5. Individual flux determinations were made from each detector, and the statistical uncertainty in each measured flux was calculated by the following:

$$\frac{\Delta\Phi_{stat}}{\Phi} = \sqrt{\left(\frac{\Delta N_\gamma}{N_\gamma}\right)^2 + \left(\frac{\Delta C_{att}}{C_{att}}\right)^2}, \tag{6.2}$$

E_γ(keV)	Coeff.	$E_n = 5$ MeV	$E_n = 6$ MeV	$E_n = 8$ MeV	$E_n = 10$ MeV
158.8	A	0.317782	0.307282	0.293948	0.283132
	B	-0.0909159	-0.0822978	-0.0728291	-0.0640136
211.0	A	0.329927	0.323317	0.316064	0.30453
	B	-0.102841	-0.0965956	-0.0897396	-0.0791023
519.5	A	-0.125171	-0.11925	-0.11043	-0.106565
583.6	A	-0.0741293	-0.0698221	-0.0579483	-0.057123
635.2	A	-0.00923538	-0.00812128	-0.00544079	-0.00554917
687.0	A	-0.180761	-0.167573	-0.139076	-0.137095
1060.3	A	0.211024	0.194611	0.141668	0.142684
	B	-0.0274945	-0.0250256	-0.0133422	-0.0131196
121.2	A	—	—	—	0.299323
	B	—	—	—	-0.0773106
148.6	A	—	—	—	-0.121403
152.7	A	—	—	0.277712	0.261978
	B	—	—	-0.0305979	-0.0332246
244.2	A	—	—	0.334955	0.325457
	B	—	—	-0.102583	-0.0933891
E_γ(keV)	Coeff.	$E_n = 11$ MeV	$E_n = 12$ MeV	$E_n = 14$ MeV	
158.8	A	—	0.270793	0.265954	
	B	—	-0.0561742	-0.0538285	
211.0	A	—	0.296674	0.293606	
	B	—	-0.0727626	-0.0709311	
519.5	A	—	-0.10065	-0.0983813	
583.6	A	—	-0.0518752	-0.0501712	
635.2	A	—	-0.00477958	-0.00458915	
687.0	A	—	-0.124501	-0.120411	
1060.3	A	—	0.125377	0.12043	
	B	—	-0.00968664	-0.00914022	
121.2	A	—	—	0.260566	
	B	—	—	-0.0523628	
148.6	A	—	—	-0.0831735	
152.7	A	0.261978	0.250617	0.24082	
	B	-0.0332246	-0.0322764	-0.0336919	
244.2	A	0.323779	0.319627	0.314245	
	B	-0.0917058	-0.885083	-0.0845552	

Table 6.2: Calculated Legendre polynomial expansion coefficients for angular distribution of γ rays emitted from uranium targets.

^{235}U			^{238}U		
E_n (MeV)	Φ_{av} ($cm^{-2}s^{-1}$)	$\Delta\Phi_{stat}$ ($cm^{-2}s^{-1}$)	E_n (MeV)	Φ_{av} ($cm^{-2}s^{-1}$)	$\Delta\Phi_{stat}$ ($cm^{-2}s^{-1}$)
8	7.859×10^3	4.578×10^1	5	4.932×10^3	1.165×10^2
10	1.117×10^4	8.074×10^1	6	5.295×10^3	4.301×10^1
11	8.093×10^3	6.246×10^1	8	1.335×10^4	7.035×10^1
12	1.509×10^4	1.187×10^2	10	1.139×10^4	1.153×10^2
14	9.864×10^3	2.589×10^1	12	1.045×10^4	1.328×10^2
			14	1.746×10^4	1.161×10^2

Table 6.3: Measured neutron fluxes and statistical uncertainties determined from 846.77 keV transition in ^{56}Fe.

where N_γ and C_{att} are, respectively, the yield of the ^{56}Fe γ-ray peak and the simulated attenuation correction. An average flux value and associated statistical uncertainty for each incident neutron energy was calculated by

$$\Phi_{av} = \sum_n \frac{\Phi_n}{(\Delta\Phi_{stat,n})^2} \Bigg/ \sum_n \frac{1}{(\Delta\Phi_{stat,n})^2} \tag{6.3}$$

$$\Delta\Phi_{av} = 1 \Bigg/ \sum_n \frac{1}{(\Delta\Phi_{stat,n})^2} \, . \tag{6.4}$$

Neutron fluxes and statistical uncertainties for each incident neutron energy are given in Table 6.3. The systematic uncertainty was calculated separately in the following manner:

$$\frac{\Delta\Phi_{sys}}{\Phi_{av}} = \sqrt{\left(\frac{\Delta\sigma_{Fe}}{\sigma_{Fe}}\right)^2 + \left(\frac{\Delta\alpha}{\alpha}\right)^2 + \left(\frac{\Delta\epsilon}{\epsilon}\right)^2 + \left(\frac{\Delta m_{Fe}}{m_{Fe}}\right)^2}, \tag{6.5}$$

where σ_{Fe}, α, ϵ, and m_{Fe} are the transition cross section, internal conversion coefficient, detector efficiency, and iron target mass. Systematic uncertainties were calculated to be $\sim 8.2\%$ for measurements using ^{235}U/^{56}Fe target and $\sim 8.1\%$ for measurements using the ^{238}U/^{56}Fe target.

6.3 Total Reaction-Channel Cross Sections

GNASH and TALYS model calculations for total reaction-channel cross sections for $^{238}\mathrm{U}(n,n')^{238}\mathrm{U}$, $^{238}\mathrm{U}(n,2n)^{237}\mathrm{U}$, and $^{235}\mathrm{U}(n,2n)^{234}\mathrm{U}$ are shown in Figures 6.3, 6.4, and 6.5 compared to existing data. In addition to a standard GNASH calculation, a second calculation (referred to as GNASH-FKK in this work) is compared where spin distribution effects for multistep direct preequilbrium reactions are calculated externally using the theory of Feshbach, Kerman, and Koonin and included in the GNASH calculation [67]. In these calculations, multistep compound preequilibrium reactions are assumed to have the same spin distribution for the residual nucleus in the case of compound reactions. In all cases, the model calculations are in good agreement with the total reaction-channel cross section data. The associated partial cross sections given by these calculations are compared to our data in Sections 6.4, 6.5, and 6.6.

6.4 Partial Cross Sections: $^{238}\mathrm{U}(n,n'\gamma)^{238}\mathrm{U}$

Seven partial cross sections were deterimed for $^{238}\mathrm{U}(n,n'\gamma)^{238}\mathrm{U}$. A partial level scheme for $^{238}\mathrm{U}$ is given in Figure 6.6. Cross sections are compared with existing data and model calculations from GNASH and TALYS. Level density parameters used in the GNASH model calculations are given in Table 6.4; parameters used in TALYS are implemented through an internal reference library based on the Reference Input Parameter Library [56] or calculated from phenomenological expressions. These parameters are defined in Section 2.2.

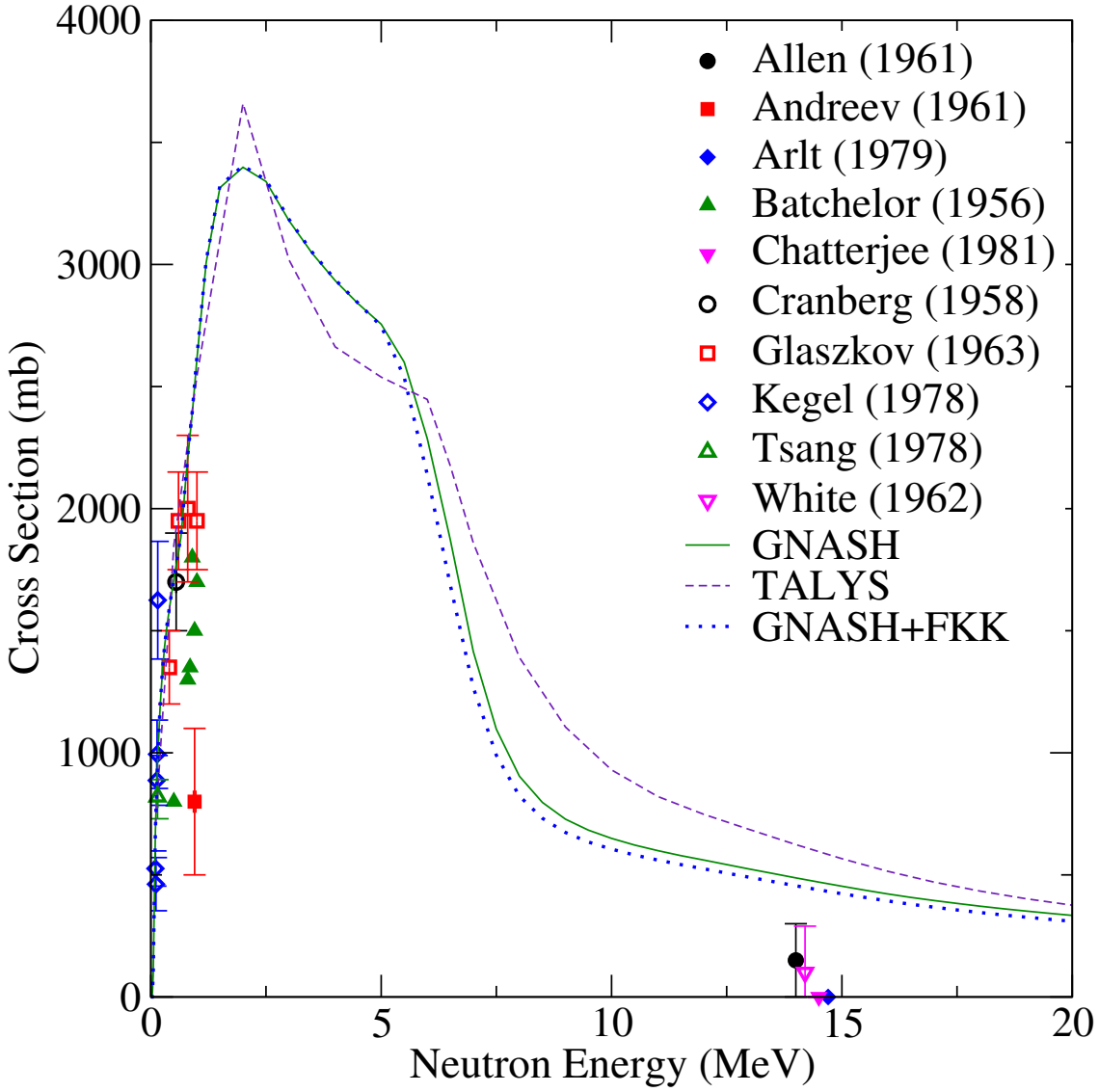

Figure 6.3: $^{238}\mathrm{U}(n,n')^{238}\mathrm{U}$ total reaction-channel cross-section data compared with model calculations.

^{239}U		^{238}U		^{237}U	
Parameter	GNASH	Parameter	GNASH	Parameter	GNASH
a	29.089	a	27.359	a	29.765
T (MeV)	0.367	T (MeV)	0.389	T (MeV)	0.401
E_c (MeV)	0.3727	E_c (MeV)	1.1126	E_c (MeV)	0.5406
Δ	0.470	Δ	0.950	Δ	0.740

Table 6.4: Level density parameters used in GNASH calculation of $^{238}\mathrm{U}(n,n'\gamma)^{238}\mathrm{U}$ and $^{238}\mathrm{U}(n,2n\gamma)^{237}\mathrm{U}$.

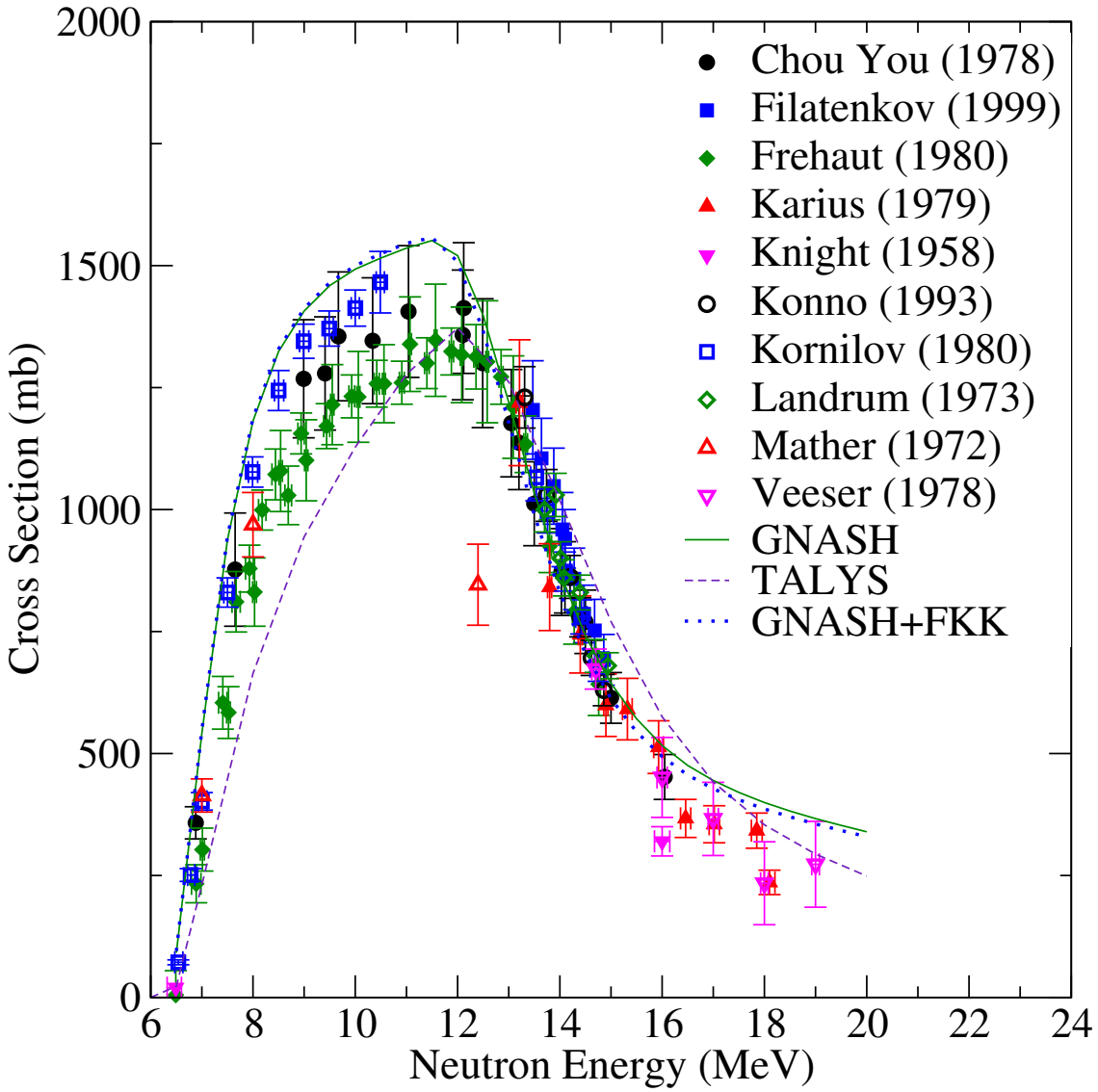

Figure 6.4: $^{238}\mathrm{U}(n,2n)^{237}\mathrm{U}$ total reaction-channel cross-section data compared with model calculations.

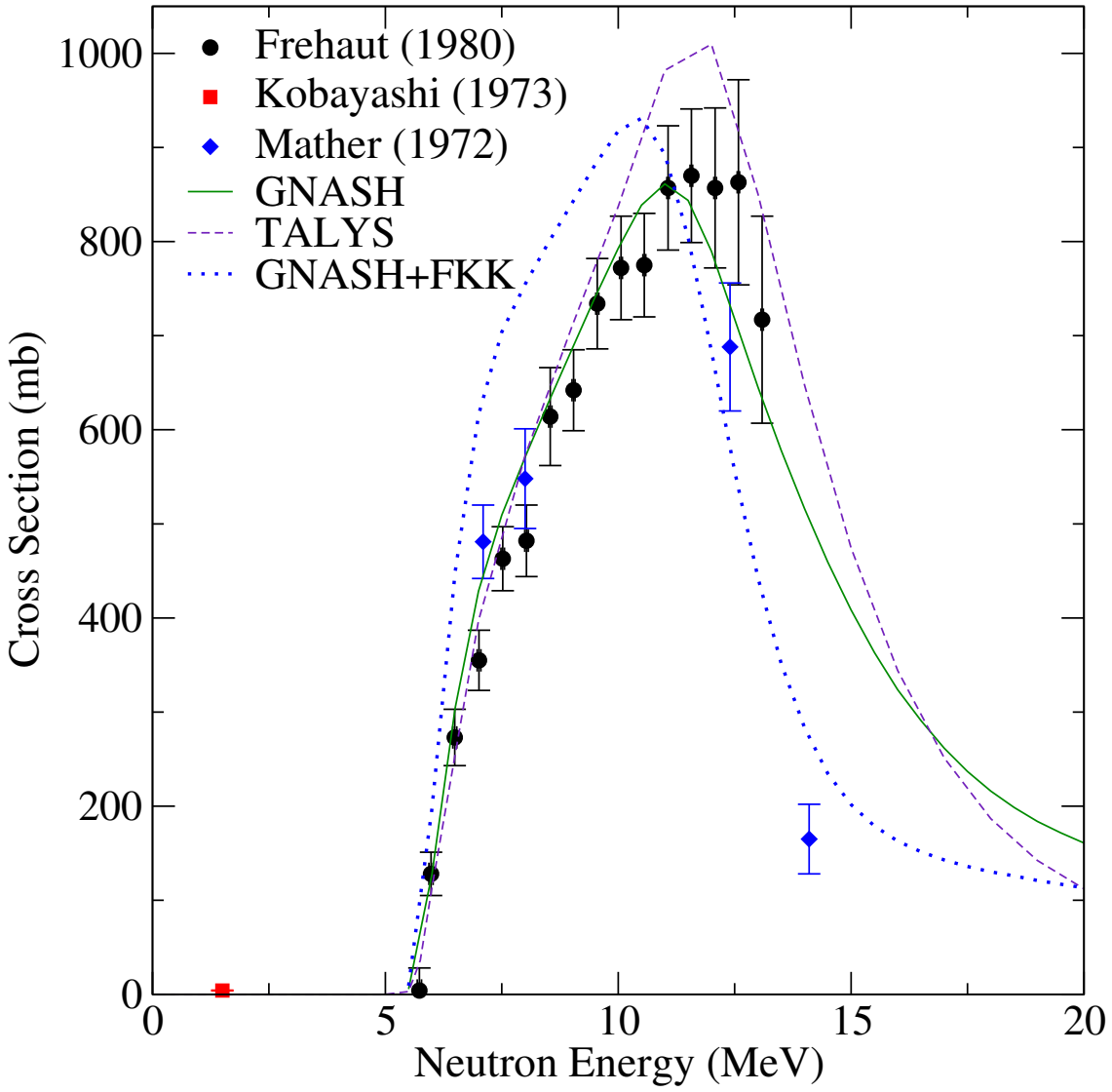

Figure 6.5: $^{235}\mathrm{U}(n,2n)^{234}\mathrm{U}$ total reaction-channel cross-section data compared with model calculations.

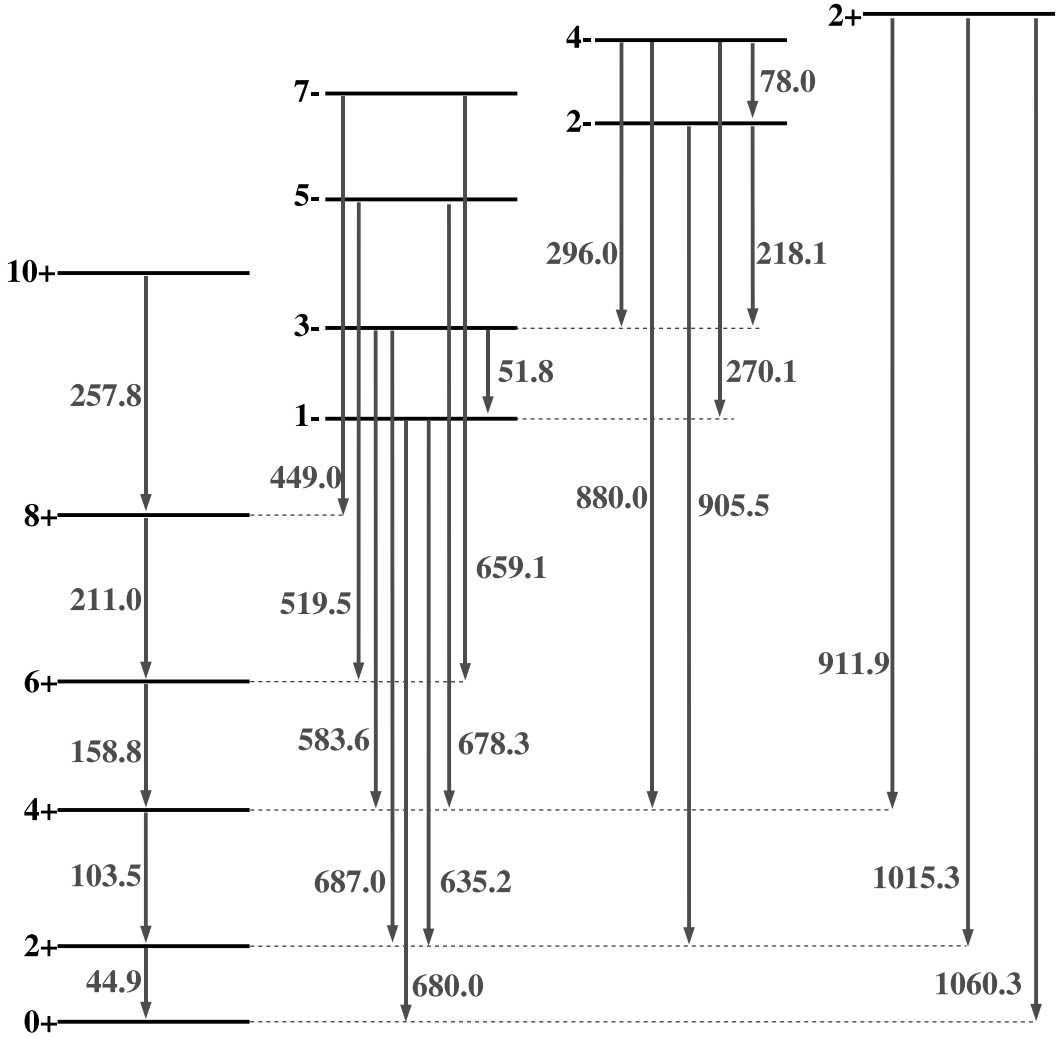

Figure 6.6: Partial level scheme for ^{238}U. Gamma-ray energies are in keV.

6.4.1 44.9 keV ($2^+ \rightarrow 0^+$) and 103.5 keV ($4^+ \rightarrow 2^+$) transitions

Transitions from lowest-lying levels are expected to carry a large fraction of the total reaction-channel cross section due to the combination of direct level population from the reaction and indirect population due to decays of higher states into the level. However, measurement of these cross sections are very challenging due to their relatively low γ-ray energy, resulting in large internal conversion coefficients and γ-ray attenuation in the target. For the 44.9 keV ($2^+ \rightarrow 0^+$) and 103.5 keV ($4^+ \rightarrow 2^+$) transitions, internal conversion coefficients were α=611 and α=11.36, corresponding to 99.84% and 91.90% internal conversion, respectively. Measurement of the 103.5 keV peak is further complicated by the proximity of peaks stemming from uranium K X-rays. In the end, accurate cross sections were not determined for these two lowest-level transitions.

6.4.2 158.8 keV ($6^+ \rightarrow 4^+$) transition

Measured partial cross sections for the 158.8 keV ($6^+ \rightarrow 4^+$) transition were determined for incident neutron energies E_n =5, 6, 10, 12, and 14 MeV. Results are given in Figure 6.7. Our cross section is in good agreement at lower energies with that measured by Fotiades *et al.* using the continuous (white) energy neutron beam from the spallation source at Los Alamos National Laboratory [68]; however, for $E_n \geq$ 10 MeV, our measured cross section resultss are lower than the previously measured values by $\sim$ 25%. Cross sections predicted by both GNASH and TALYS are in good agreement with the data, while the FKK-corrected GNASH calculation underpredicts the cross section above $\sim$ 5 MeV.

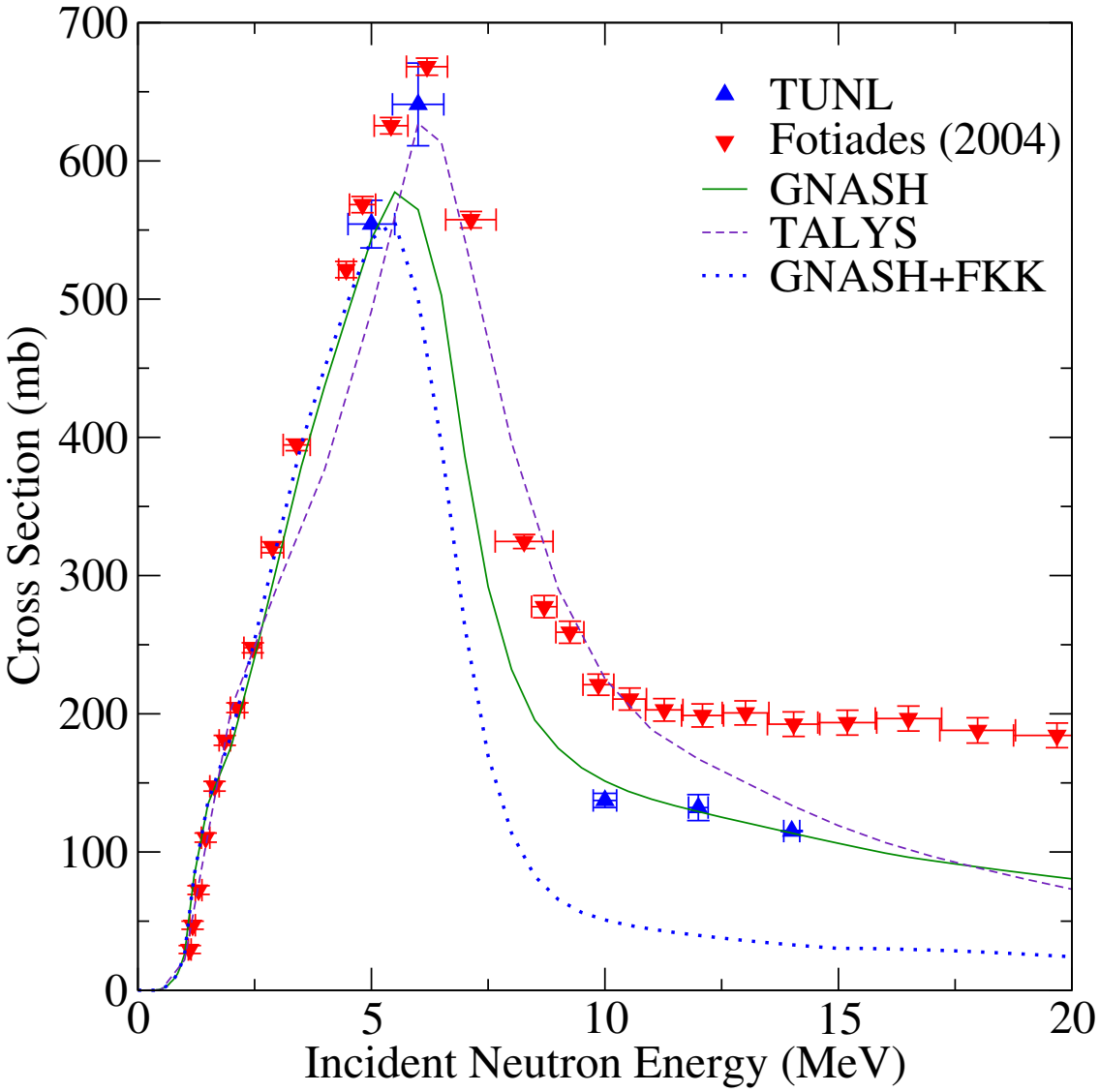

Figure 6.7: $^{238}\mathrm{U}(n,n'\gamma)^{238}\mathrm{U}$ cross section for the 158.8 keV ($6^+ \rightarrow 4^+$) transition. Comparision with existing cross-section data and model calculations are shown. Error bars given in plot are due to statistical uncertainties only.

6.4.3 211.0 keV ($8^+ \rightarrow 6^+$) transition

Measured partial cross sections for the 211.0 keV ($8^+ \rightarrow 6^+$) transition were determined for incident neutron energies E_n =5, 6, 10, and 14 MeV. Results are given in Figure 6.8. Similar to the 158.8 keV transition, our cross section is in good agreement at lower energies with that measured by Fotiades *et al.* but shows slightly smaller values for $E_n \geq 10$ MeV. Both GNASH and TALYS calculations overpredict the cross section above ~ 8 MeV due to the incorrect preequilbirium spin distribution assumed by the exciton model. The FKK-corrected GNASH calculation is in good agreement with the data.

6.4.4 635.2 keV ($1^- \rightarrow 2^+$) transition

Measured partial cross sections for the 635.2 keV ($1^- \rightarrow 2^+$) transition were determined for incident neutron energies E_n =5, 6, 8, 10, and 14 MeV. Results are given in Figure 6.9. In this case, the partial cross section was measured previously by Voss *et al.* [70] and Olsen *et al.* [69] in addition to Fotiades *et al.* Cross sections measured in this work are in good agreement with both the Olsen and Fotiades data at low energies though, interestingly, the Fotiades data gives lower cross section values for $E_n \geq 8$ MeV. Cross sections measured by Voss are much lower than the other data sets for $E_n \gtrsim 2$ MeV. The GNASH calculation underpredicts the cross section while TALYS and FKK-corrected GNASH calculation are generally in good agreement.

A second γ-ray transition can be observed from the 1^- level with $E_\gamma = 680.0$ keV; however, due to the proximity of a γ-ray peak stemming from the 678.3 keV ($5^- \rightarrow 4^+$) transition, individual peaks could not be resolved, and an accurate cross section was not extracted.

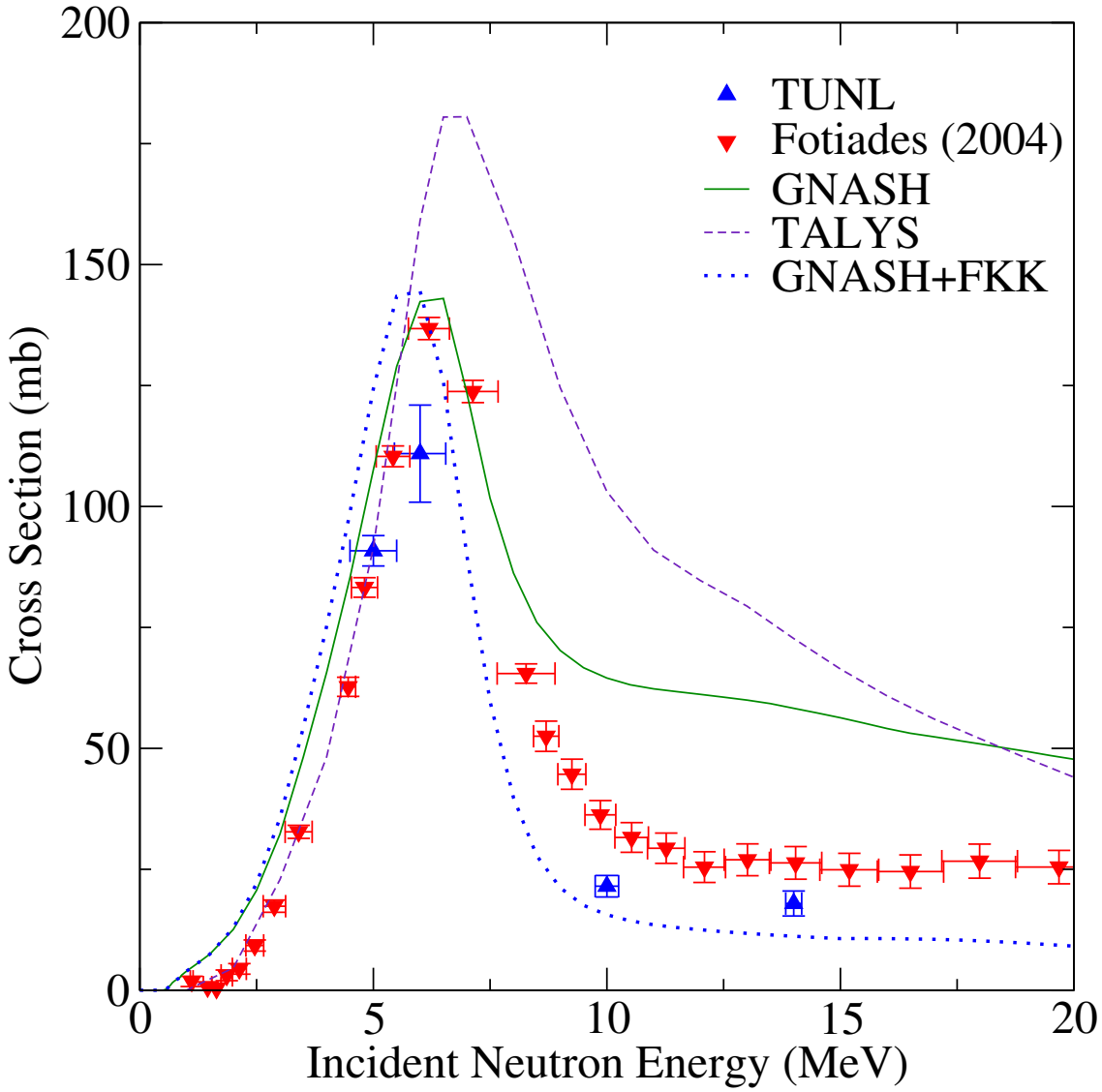

Figure 6.8: $^{238}\mathrm{U}(n,n'\gamma)^{238}\mathrm{U}$ cross section for the 211.0 keV ($8^+ \rightarrow 6^+$) transition. Comparision with existing cross section and model calculations are shown. Error bars given in plot are due to statistical uncertainties only.

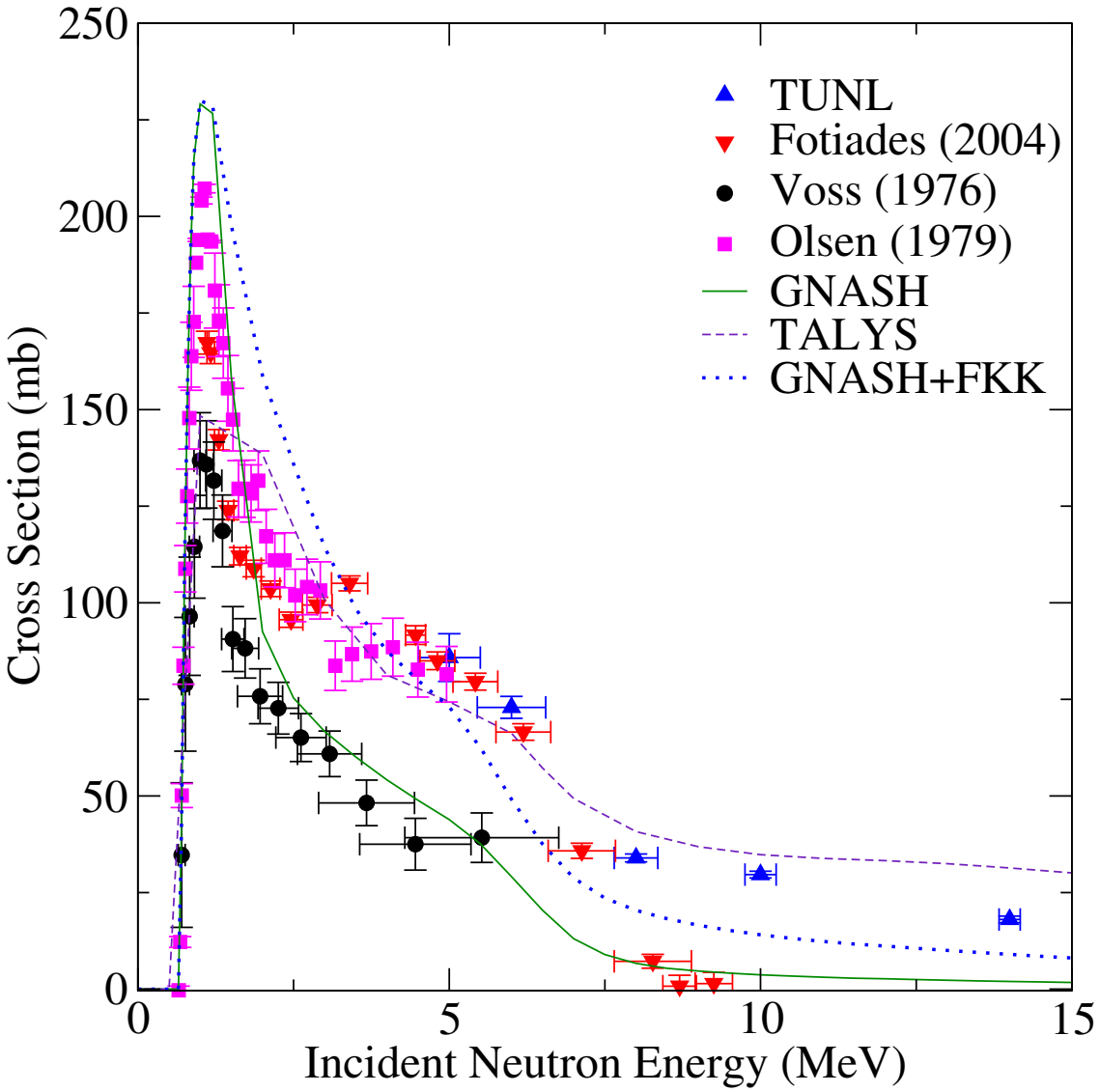

Figure 6.9: $^{238}\mathrm{U}(n,n'\gamma)^{238}\mathrm{U}$ cross section for the 635.2 keV ($1^- \rightarrow 2^+$) transition. Comparision with existing cross section and model calculations are shown. Error bars given in plot are due to statistical uncertainties only.

6.4.5 687.0 keV ($3^- \rightarrow 2^+$) transition

Two partial cross sections were measured for transitions from the 3^- level. Measured partial cross sections for the 687.0 keV ($3^- \rightarrow 2^+$) transition were determined for incident neutron energies E_n =5, 6, 8, 10, and 14 MeV. Results are given in Figure 6.10. Our results are again in good agreement with the Olsen data and, for $E_n \geq 8$ MeV, with the Fotiades data. Cross sections measured by Voss are again much lower than the other data sets for $E_n \gtrsim 2$ MeV.

6.4.6 583.6 keV ($3^- \rightarrow 4^+$) transition

Measured partial cross sections for the second transition from the 3^- level, E_γ = 583.6 keV ($3^- \rightarrow 4^+$), were determined for incident neutron energies E_n =5, 6, 8, and 10 MeV. Results are given in Figure 6.11. Our cross section results are in good agreement with those given by Olsen and represent the only measurement of this cross section for $E_n \geq 5$ MeV.

6.4.7 519.5 keV ($5^- \rightarrow 6^+$) transition

Measured partial cross sections for the 519.5 keV ($5^- \rightarrow 6^+$) transition were determined for incident neutron energies E_n =5, 6, 8, and 10 MeV. Results are given in Figure 6.12. Our cross section results are in good agreement with those given by Olsen and represent the only measurement of this cross section for $E_n \geq 5$ MeV.

6.4.8 1060.3 keV ($2^+ \rightarrow 0^+$) transition

Measured partial cross sections for the 1060.3 keV ($2^+ \rightarrow 0^+$) transition were determined for incident neutron energies E_n =5, 6, 8, and 10 MeV. Results are given in Figure 6.13. Our results are again in good agreement with the Olsen data and, for $E_n \geq 8$ MeV, with the Fotiades data. Cross sections measured by Voss are again

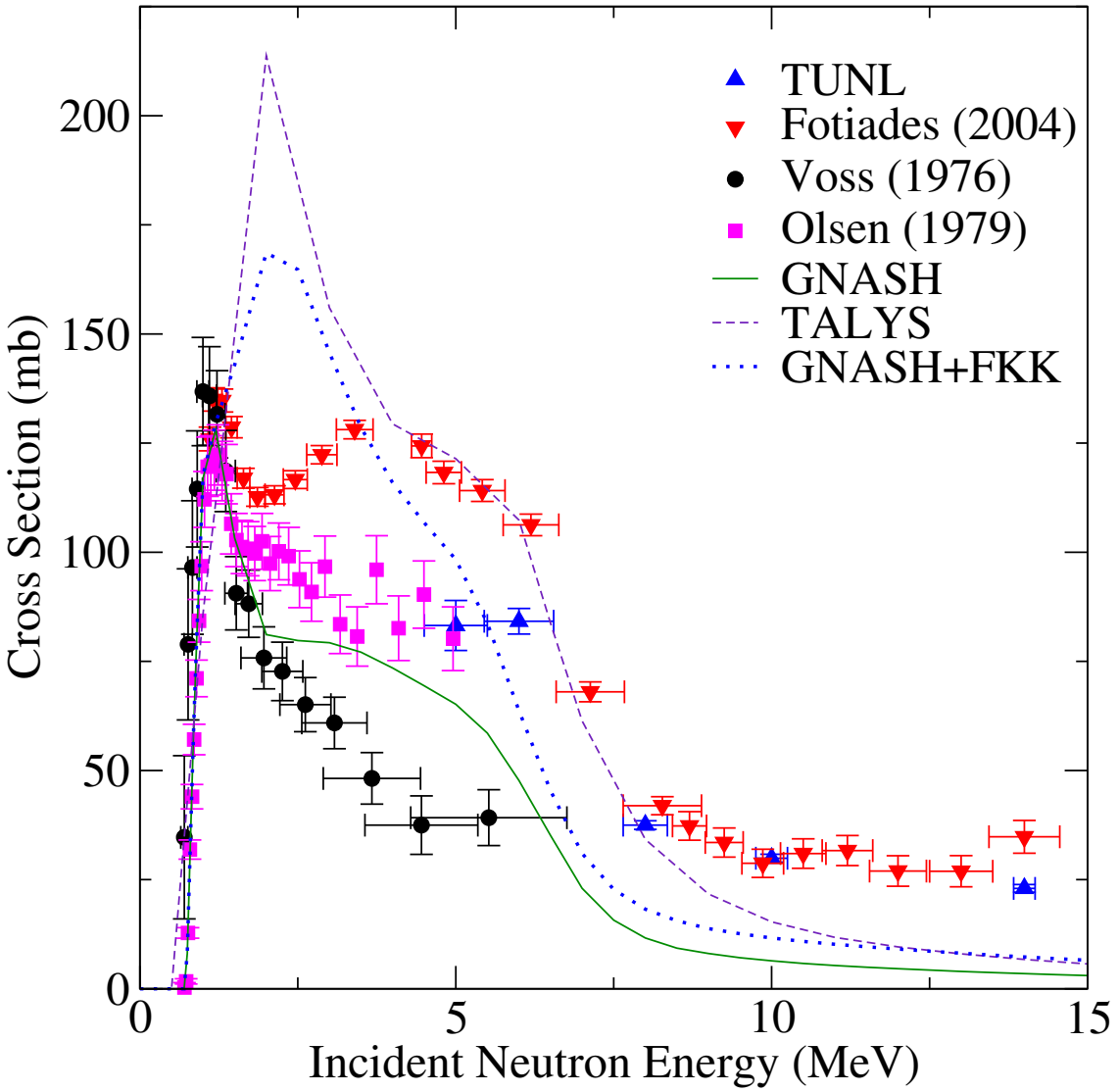

Figure 6.10: $^{238}\mathrm{U}(n,n'\gamma)^{238}\mathrm{U}$ cross section for the 687.0 keV ($3^- \rightarrow 4^+$) transition. Comparision with existing cross-section data and model calculations are shown. Error bars given in plot are due to statistical uncertainties only.

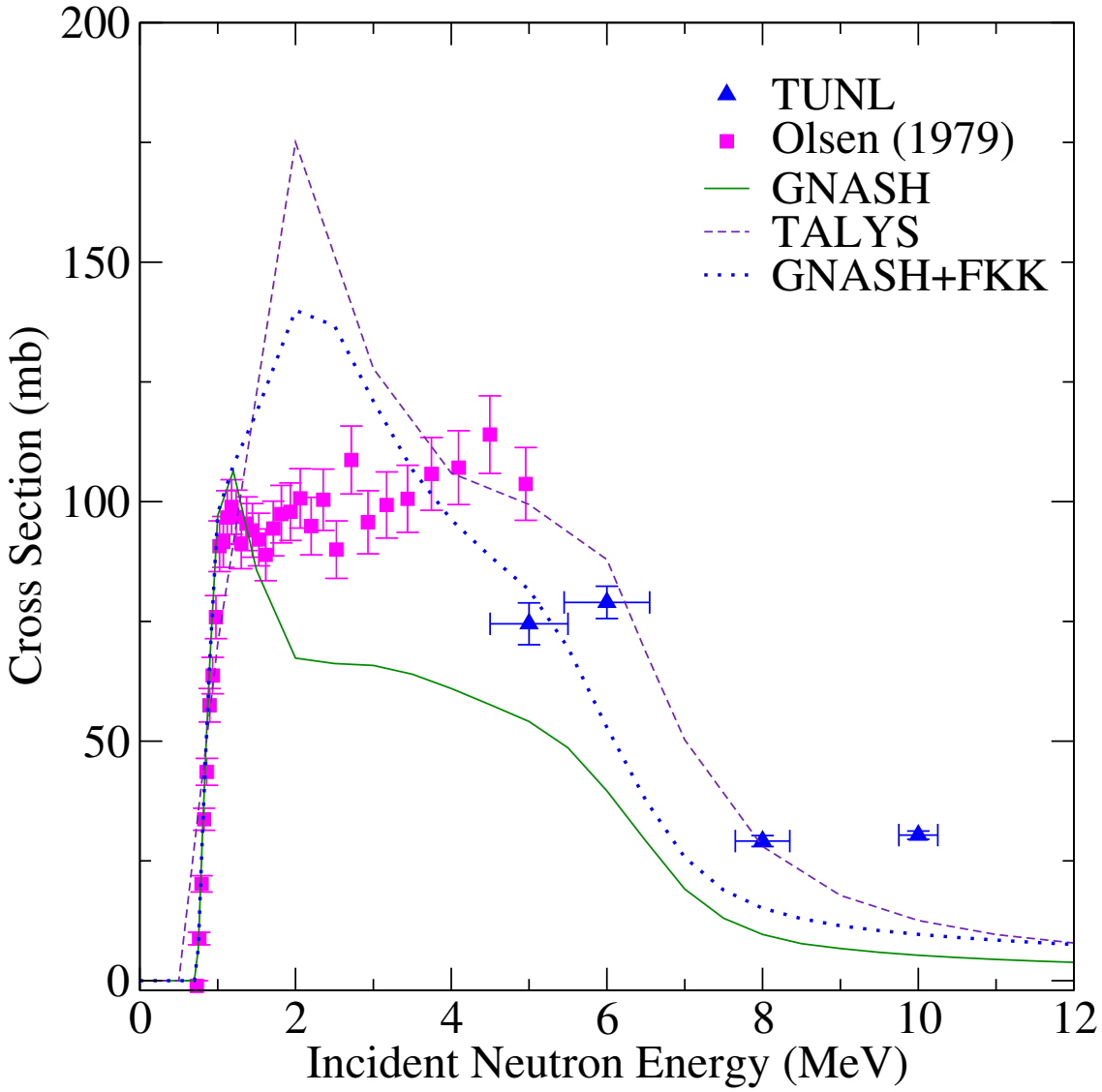

Figure 6.11: $^{238}\mathrm{U}(n,n'\gamma)^{238}\mathrm{U}$ cross section for the 583.6 keV ($3^- \rightarrow 4^+$) transition. Comparision with existing cross-section data and model calculations are shown. Error bars given in plot are due to statistical uncertainties only.

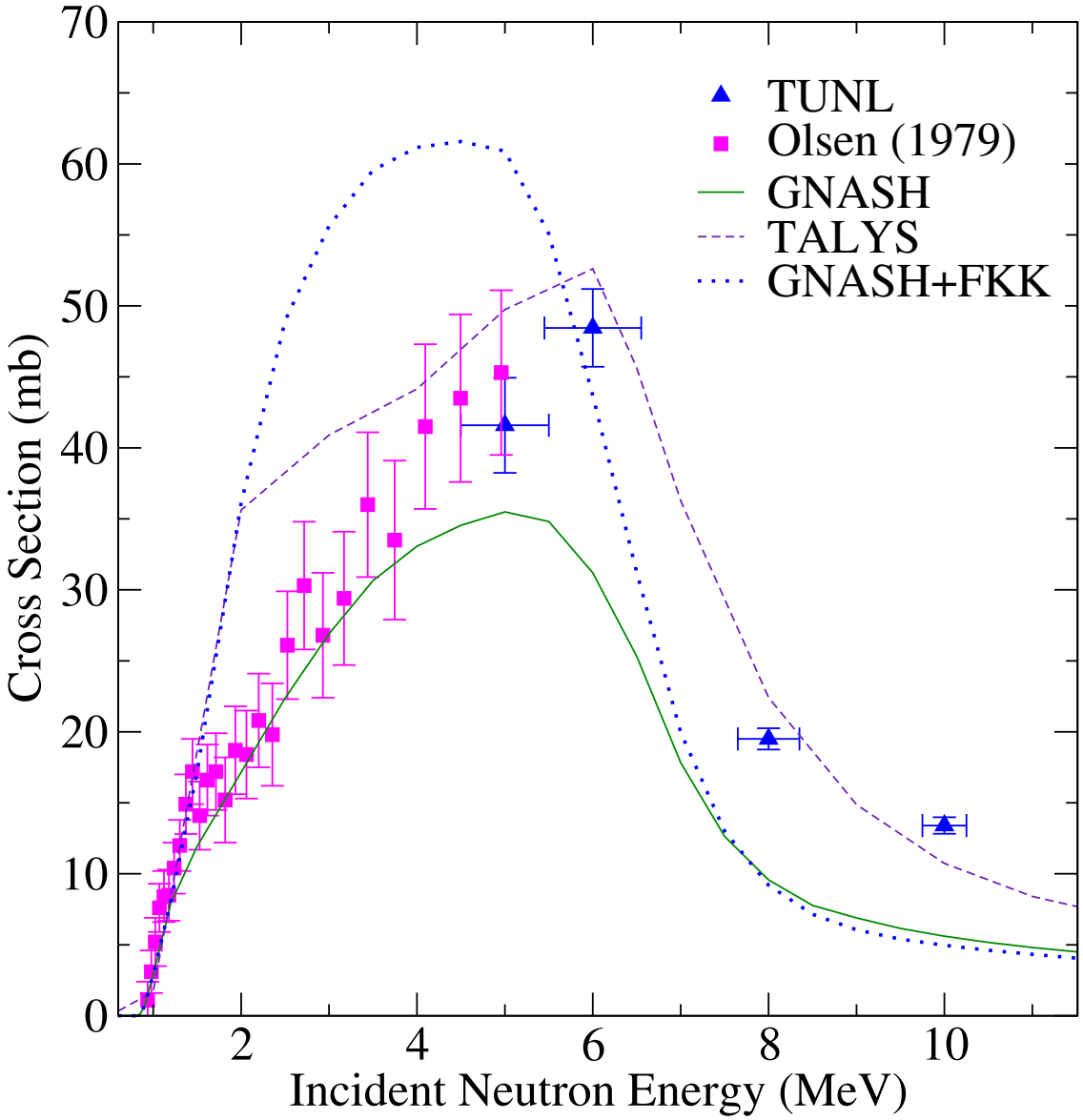

Figure 6.12: $^{238}\mathrm{U}(n,n'\gamma)^{238}\mathrm{U}$ cross section for the 519.5 keV ($5^- \rightarrow 6^+$) transition. Comparision with existing cross-section data and model calculations are shown. Error bars given in plot are due to statistical uncertainties only.

much lower than the other data sets for $E_n \gtrsim 2$ MeV. Model calculations by GNASH, both standard and FKK-corrected, predict values much lower than those given by any experimental data set; calculations at this high excitation energy were not available from TALYS.

A second γ-ray transition is expected from the 2^+ level with $E_\gamma = 1015.3$ keV; however, due to the proximity of a 1014.42 keV γ-ray peak stemming from $^{27}\mathrm{Al}(n,n')^{27}\mathrm{Al}$ reaction, the peak was obscured and accurate cross section data could not be extracted.

6.5 Partial Cross Sections: $^{238}\mathrm{U}(n,2n\gamma)^{237}\mathrm{U}$

Two partial cross sections were deterimed for $^{238}\mathrm{U}(n,2n\gamma)^{237}\mathrm{U}$. A partial level scheme for $^{237}\mathrm{U}$ is given in Figure 6.14. Cross sections are compared with existing data and model calculations from GNASH and TALYS. Level density parameters used in the GNASH model calculations are given in Table 6.4; parameters used in TALYS are implemented through an internal reference library based on the Reference Input Parameter Library [56] or calculated from phenomenological expressions.

6.5.1 The lowest-lying level transitions

As with $^{238}\mathrm{U}(n,n'\gamma)^{238}\mathrm{U}$, measurement of the lowest-lying level transitions for $^{238}\mathrm{U}(n,2n\gamma)^{237}\mathrm{U}$ is a challenge due to internal conversion, γ-ray attenuation in the target, and large X-ray backgrounds. Table 6.5 gives the internal conversion coefficents for the five lowest-lying level transitions in $^{237}\mathrm{U}$. As a result, accurate partial cross sections could not be determined for these transtions.

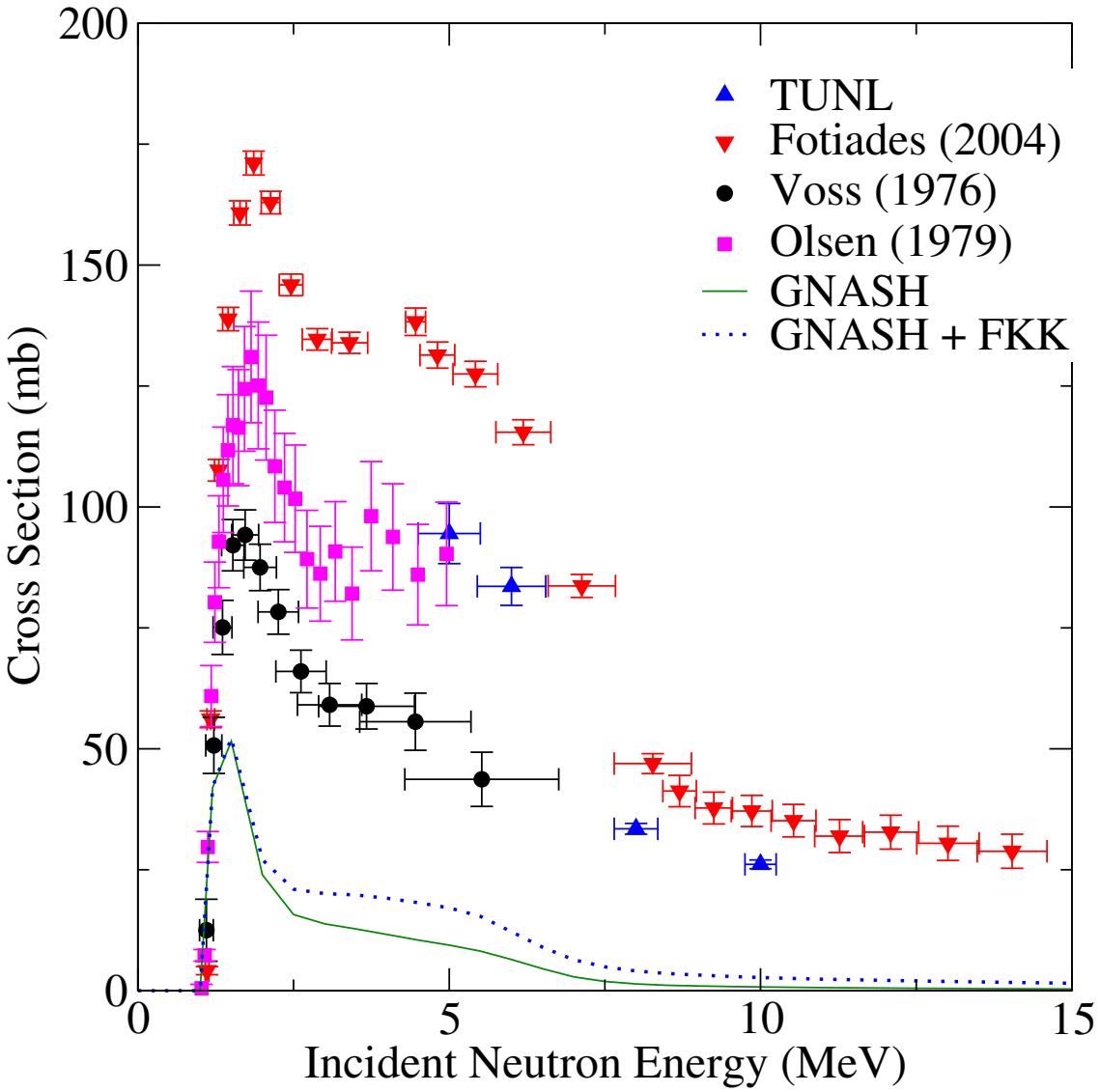

Figure 6.13: $^{238}\mathrm{U}(n,n'\gamma)^{238}\mathrm{U}$ cross section for the 1060.3 keV ($2^+ \rightarrow 0^+$) transition. Comparision with existing cross-section data and model calculations are shown. Error bars given in plot are due to statistical uncertainties only.

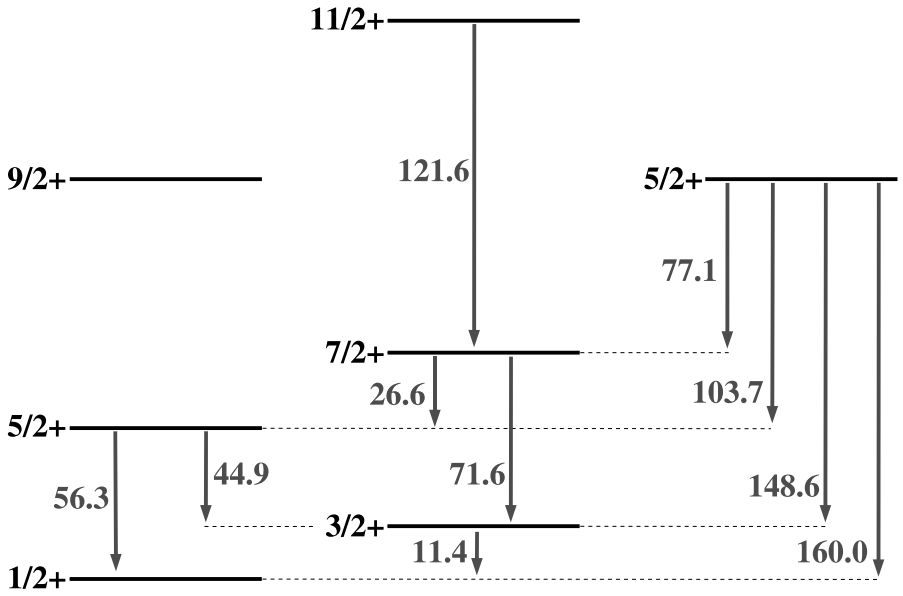

Figure 6.14: Partial level scheme for ^{237}U. Gamma-ray energies are in keV.

E_γ (keV)	Transition	ICC	% Converted
11.4	$\frac{3}{2}^+ \rightarrow \frac{1}{2}^+$	688	99.9
56.3	$\frac{5}{2}^+ \rightarrow \frac{1}{2}^+$	204	99.5
44.9	$\frac{5}{2}^+ \rightarrow \frac{3}{2}^+$	47.9	98.0
71.6	$\frac{7}{2}^+ \rightarrow \frac{3}{2}^+$	64.5	98.5
26.6	$\frac{7}{2}^+ \rightarrow \frac{5}{2}^+$	224	99.6

Table 6.5: Internal conversion of transitions in lowest-lying levels in ^{237}U. With the exception of the 44.9 keV transition, multipolarities are assumed based on spins and parities of the initial and final levels of the transition.

6.5.2 148.6 keV ($\frac{5}{2}^+ \rightarrow \frac{3}{2}^+$) transition

Measured partial cross sections for the 148.6 keV ($\frac{5}{2}^+ \rightarrow \frac{3}{2}^+$) transition were determined for incident neutron energies E_n =10 and 14 MeV. Results are given in Figure 6.15. Unlike those measured for $^{238}\mathrm{U}(n,n'\gamma)^{238}\mathrm{U}$, there is considerable disagreement between the cross sections measured in this work and those given by Fotiades *et al.* Specifically, the Fotiades data is larger by a factor of 3.5. The reason for this discrepancy is unknown; however, the previous data is somewhat suspect due to nearly 100 mb cross sections being measured below the $(n,2n)$ reaction threshold (E_n = 6.18 MeV). GNASH calculations generally agree with the Fotiades data, while TALYS greatly overestimates the cross section, likely due to the incorrect preequilibrium spin distribution for this higher-spin state.

6.5.3 121.2 keV ($\frac{11}{2}^+ \rightarrow \frac{7}{2}^+$) transition

Measured partial cross sections for the 121.2 keV ($\frac{11}{2}^+ \rightarrow \frac{7}{2}^+$) transition were determined for incident neutron energies E_n =10 and 14 MeV. Results are given in Figure 6.16. As with the 148.6 keV ($\frac{5}{2}^+ \rightarrow \frac{3}{2}^+$) transition, the previous data, which again measured sizable cross sections below reaction threshold, is larger than the current measurements by a factor of 3.5. In this case, however, both the GNASH and TALYS calculations predict values much smaller than either data set.

6.6 Partial Cross Sections: $^{235}\mathrm{U}(n,2n\gamma)^{234}\mathrm{U}$

Two partial cross sections were deterimed for $^{235}\mathrm{U}(n,2n\gamma)^{234}\mathrm{U}$. A partial level scheme for $^{234}\mathrm{U}$ is given in Figure 6.17. Cross sections are compared with existing data and model calculations from GNASH and TALYS. Level density parameters used in the GNASH model calculations are given in Table 6.6; parameters used in TALYS

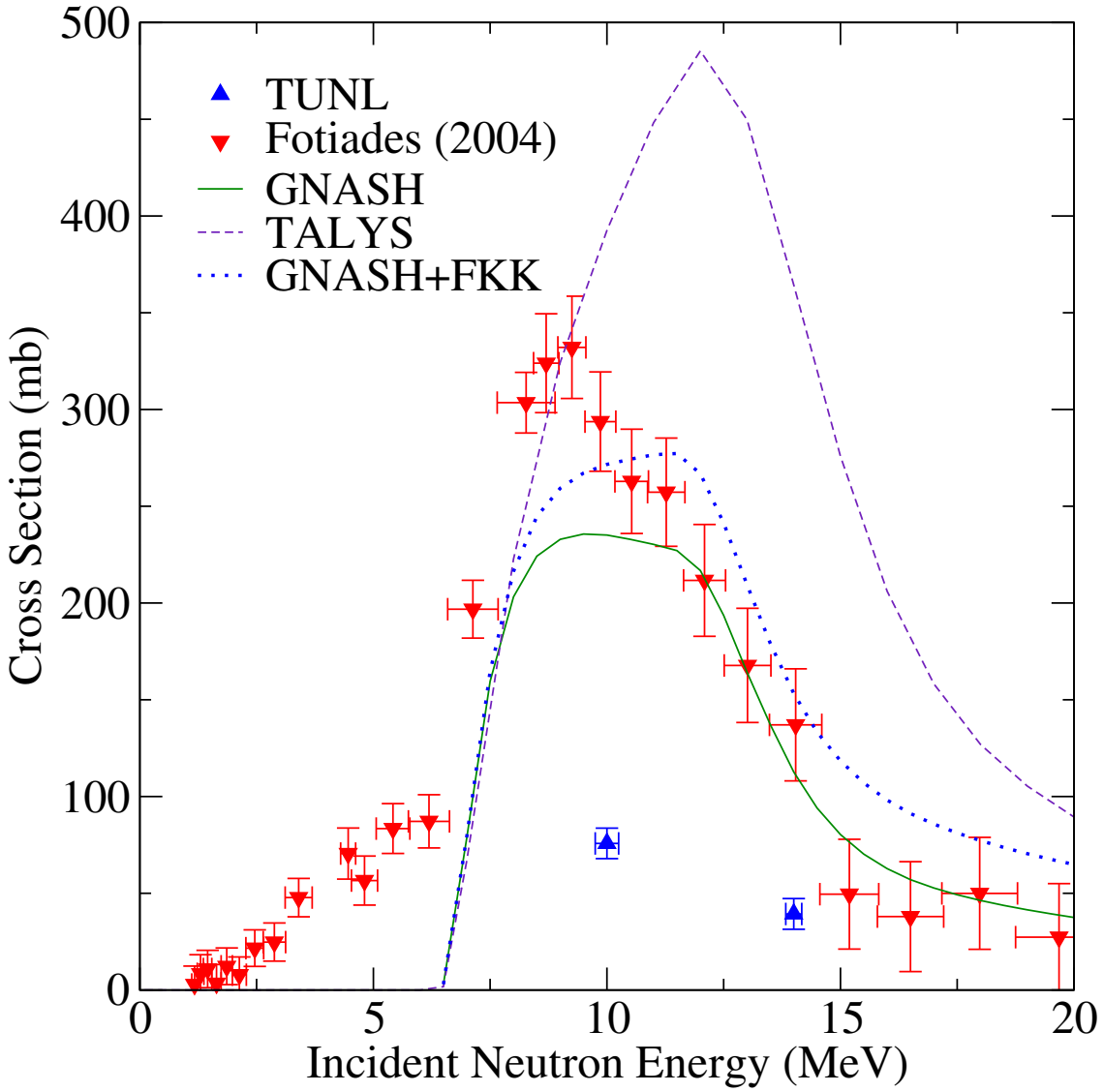

Figure 6.15: $^{238}\mathrm{U}(n,2n\gamma)^{237}\mathrm{U}$ cross section for the 148.6 keV ($\frac{5}{2}^{+} \rightarrow \frac{3}{2}^{+}$) transition. Comparision with existing cross-section data and model calculations are shown. Error bars given in plot are due to statistical uncertainties only.

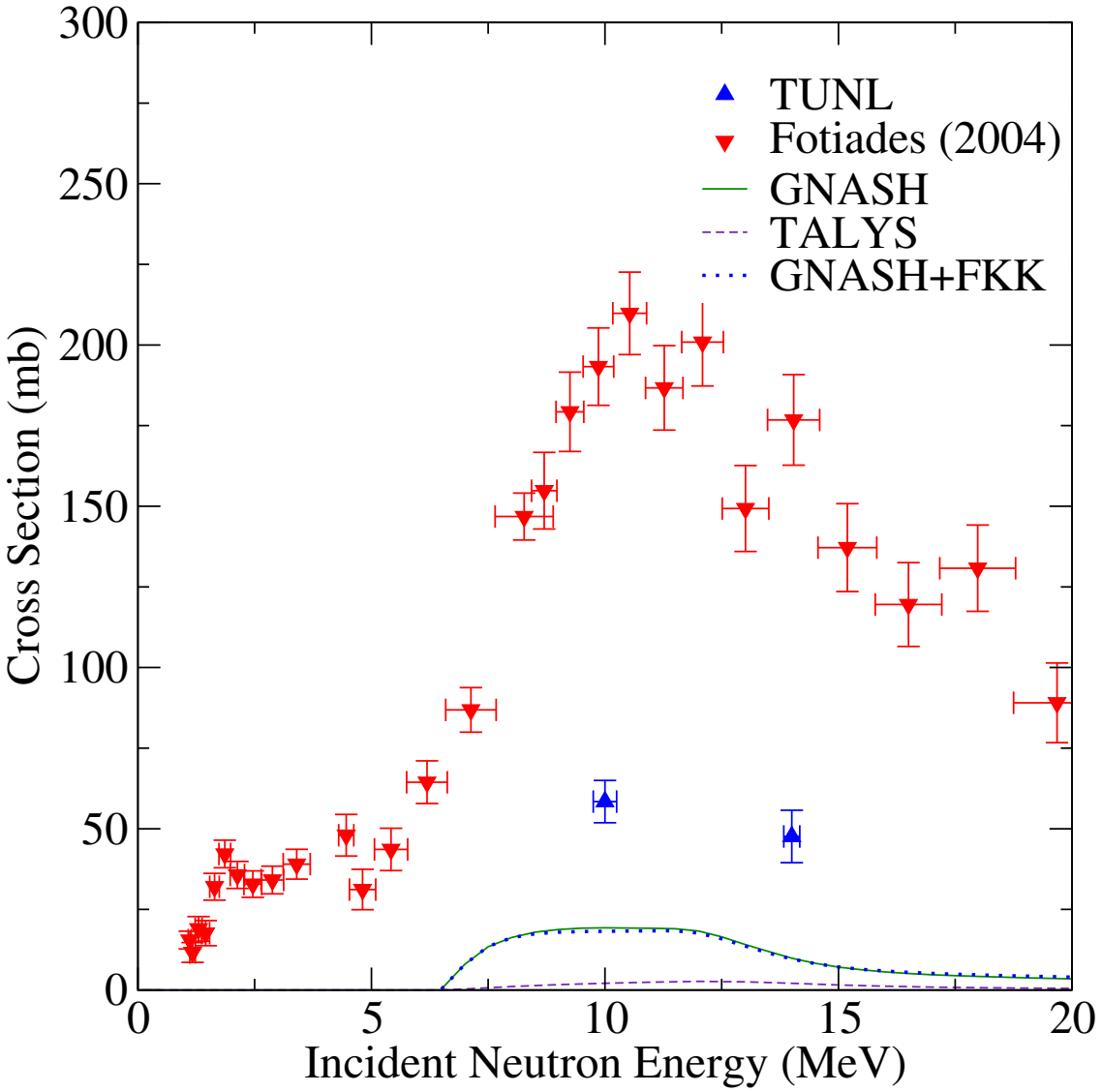

Figure 6.16: $^{238}\mathrm{U}(n, 2n\gamma)^{237}\mathrm{U}$ cross section for the 121.2 keV ($\frac{11}{2}^{+} \rightarrow \frac{7}{2}^{+}$) transition. Comparision with existing cross-section data and model calculations are shown. Error bars given in plot are due to statistical uncertainties only.

are implemented through an internal reference library based on the Reference Input Parameter Library [56] or calculated from phenomenological expressions. These parameters are defined in Section 2.2.

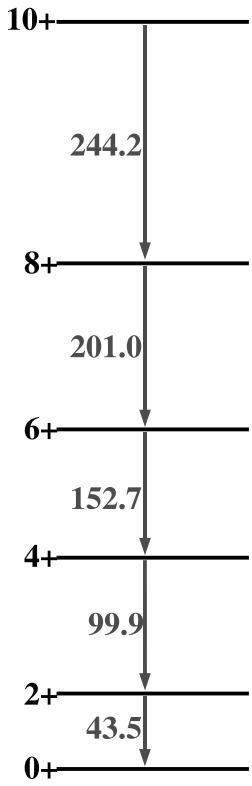

Figure 6.17: Partial level scheme for ^{234}U. Gamma-ray energies are in keV.

6.6.1 43.5 keV ($2^+ \rightarrow 0^+$) and 99.9 keV ($4^+ \rightarrow 2^+$) transitions

As in the case of the $2^+ \rightarrow 0^+$ and $4^+ \rightarrow 2^+$ transitions in ^{238}U, extraction of cross sections for the 43.5 keV ($2^+ \rightarrow 0^+$) and 99.9 keV ($4^+ \rightarrow 2^+$) transitions in ^{234}U is hindered by large internal conversion coefficients (713 and 13.4, respectively), attenuation within the target, and background from X-rays.

^{236}U Parameter	GNASH	^{235}U Parameter	GNASH	^{234}U Parameter	GNASH
a	28.298	a	28.308	a	29.000
T (MeV)	0.391	T (MeV)	0.387	T (MeV)	0.392
E_c (MeV)	1.1718	E_c (MeV)	0.5000	E_c (MeV)	1.3417
Δ	1.140	Δ	0.250	Δ	1.200

Table 6.6: Level density parameters used in GNASH calculation of ^{235}U$(n, 2n\gamma)^{234}$U.

6.6.2 152.7 keV $(6^+ \rightarrow 4^+)$ transition

Measured partial cross sections for the 152.7 keV $(6^+ \rightarrow 4^+)$ transition were determined for incident neutron energies E_n =8, 10, 11, 12, and 14 MeV. Results are given in Figure 6.18. Our results are in excellent agreement with those measured by McNabb *et al.* using the spallation neutron source at Los Alamos National Laboratory [71] and with those calculated by GNASH. TALYS overpredicts the cross section about its peak while the FKK-corrected GNASH calculation gives values that are lower than the data for $E_n > 10$ MeV.

6.6.3 244.2 keV $(10^+ \rightarrow 8^+)$ transition

The next expected transition, 201.0 keV $(8^+ \rightarrow 6^+)$, is obscured by a strong γ-ray peak resulting from α-decay of the ^{235}U target. An example spectrum in this energy region is shown in Figure 6.19. Therefore, the next availible transition is found at 244.2 keV. Measured partial cross sections for this $10^+ \rightarrow 8^+$ transition were determined for incident neutron energies E_n =8, 10, 11, 12, and 14 MeV. Results are given in Figure 6.20. This measurement represents the only reported data of this cross section. Both GNASH and TALYS calculations significantly overestimate the cross section above E_n = 11 MeV due to the incorrect preequilibrium spin distribution while the FKK-corrected GNASH calculation gives values slightly lower than the data.

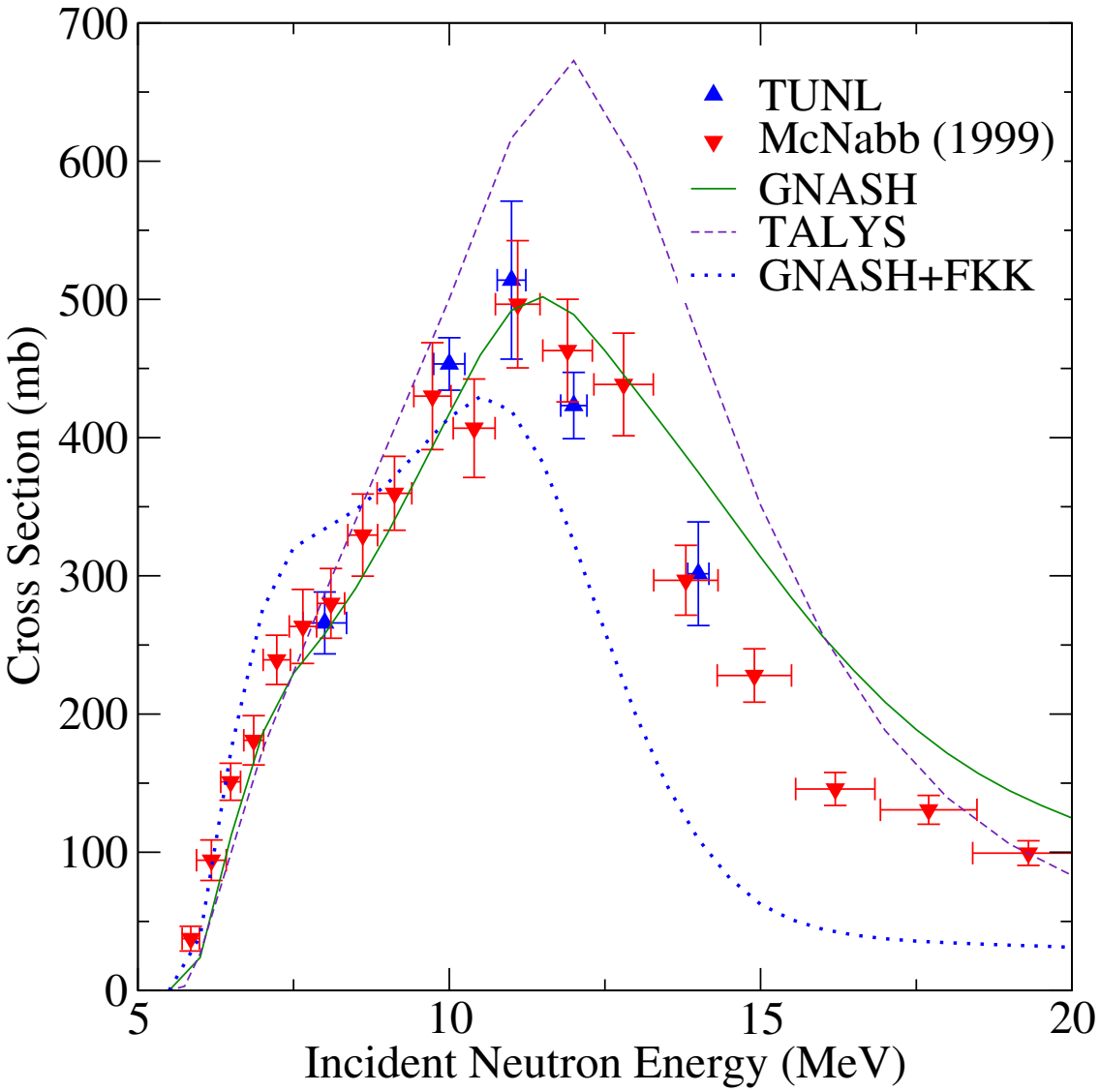

Figure 6.18: $^{235}\mathrm{U}(n, 2n\gamma)^{234}\mathrm{U}$ cross section for the 152.7 keV ($6^+ \rightarrow 4^+$) transition. Comparision with existing cross-section data and model calculations are shown. Error bars given in plot are due to statistical uncertainties only.

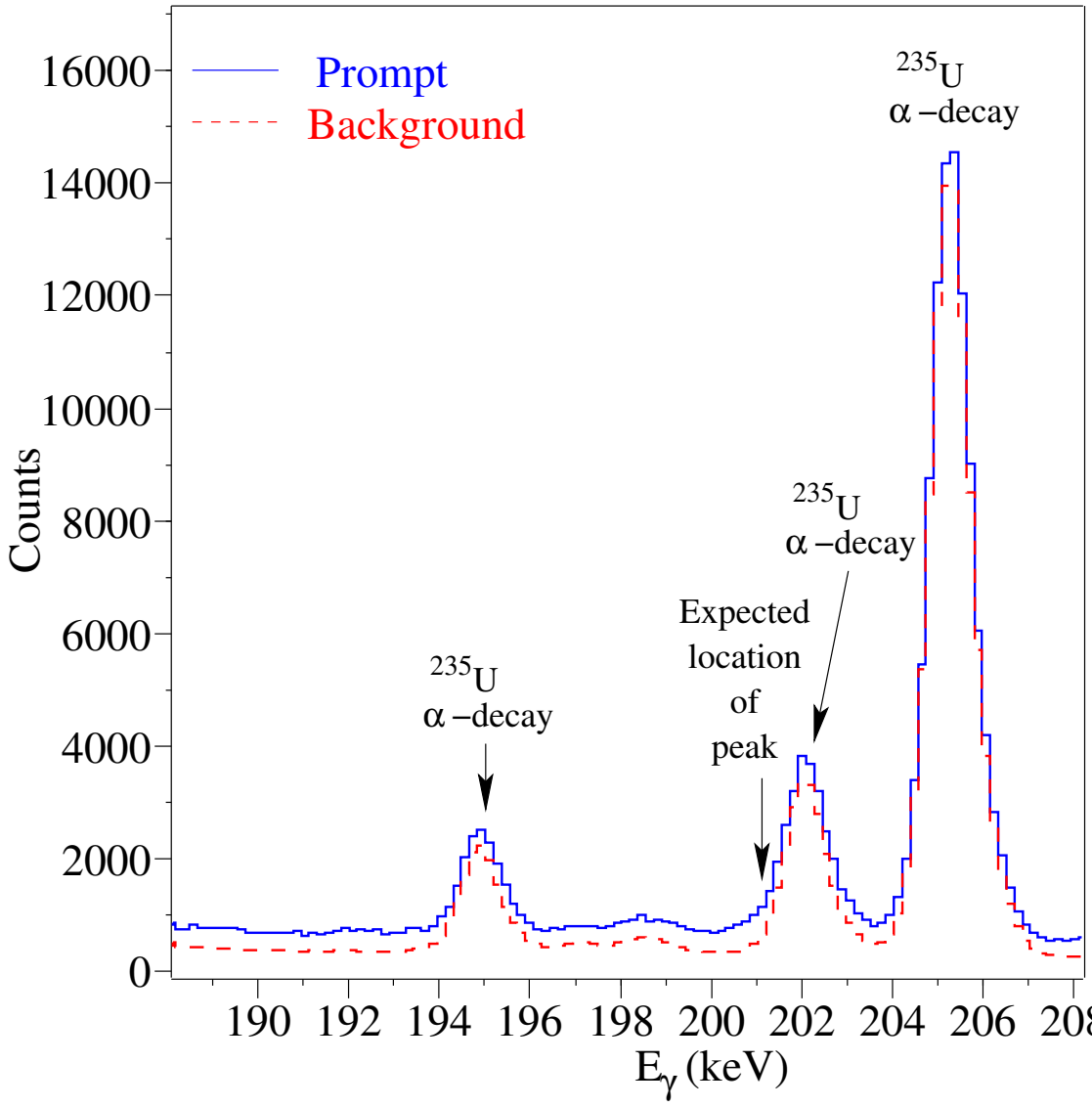

Figure 6.19: Planar detector gamma-energy spectra with prompt and background timing cuts for ^{235}U at E_n =12 MeV. The 201.0 keV ($8^+ \rightarrow 6^+$) transition is obscured by a strong peak resulting from α-decay of the ^{235}U target.

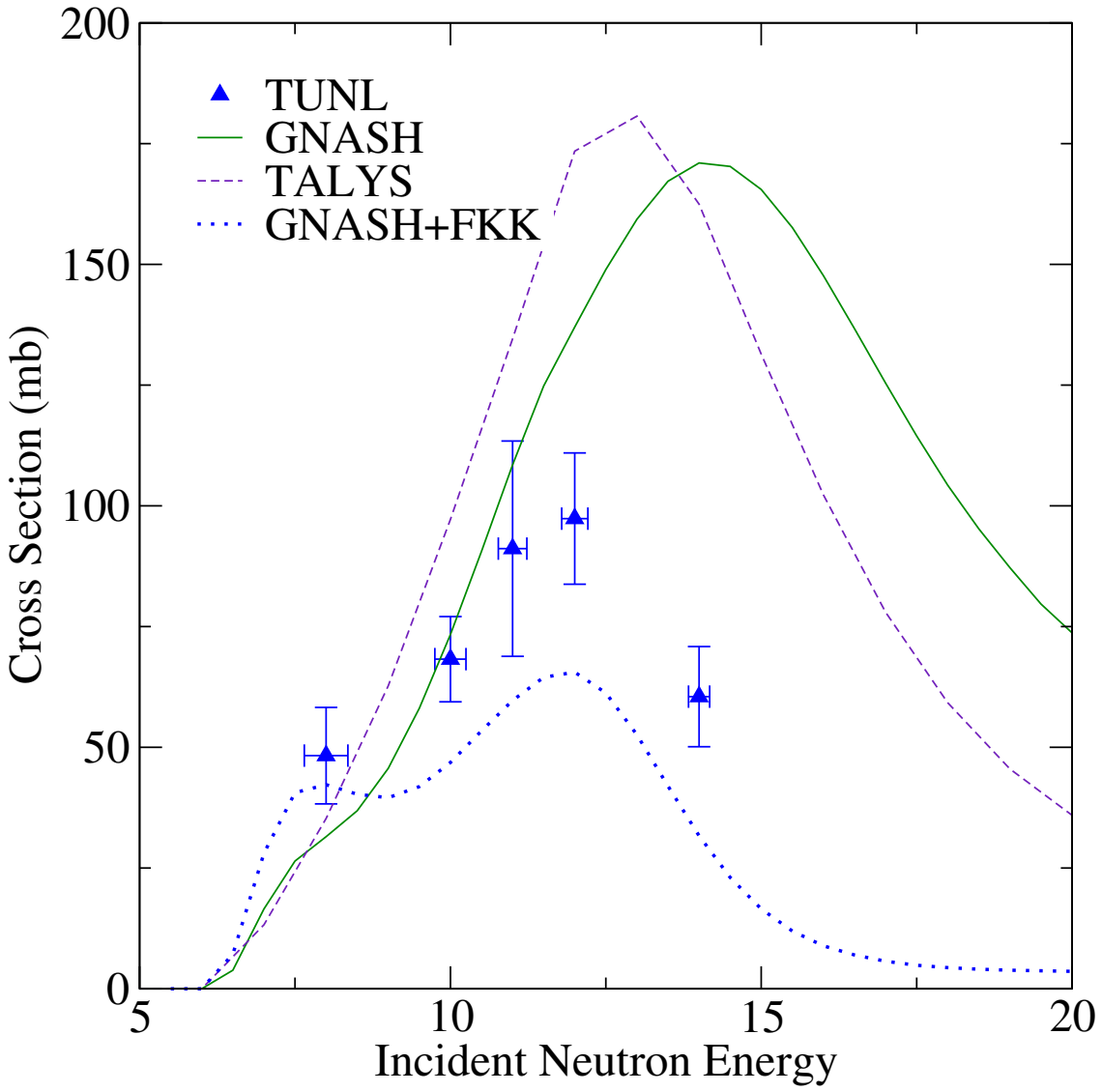

Figure 6.20: $^{235}\mathrm{U}(n, 2n\gamma)^{234}\mathrm{U}$ cross section for the 244.2 keV ($10^+ \rightarrow 8^+$) transition. Comparision with model calculations are shown. Error bars given in plot are due to statistical uncertainties only.

Value	^{238}U Uncertainty	^{235}U Uncertainty
m_U	$< 1\%$	1%
Φ	8.2%	8.1%
α	1.4%	1.4%
ϵ	2.2%	2.2%
Total	8.6%	8.6%

Table 6.7: Systematic uncertainties in the determination of cross sections.

6.7 Systematic Uncertainties

Systematic uncertainties for the partial cross section measurements are given in Table 6.7. Total systematic uncertainties are calculated by

$$\frac{\Delta\sigma_{sys}}{\sigma} = \sqrt{\left(\frac{\Delta\Phi}{\Phi}\right)^2 + \left(\frac{\Delta\alpha}{\alpha}\right)^2 + \left(\frac{\Delta\epsilon}{\epsilon}\right)^2 + \left(\frac{\Delta m_U}{m_U}\right)^2}, \tag{6.6}$$

where Φ is the neutron flux, α is the internal conversion coefficient of the measured transition, ϵ is the absolute efficiency of the detector, and m_U is the mass of the uranium target. Transitions measured had no beam-correlated or sample-correlated background interference of significance.

6.8 Beam Time Devoted

About 1100 hours of neutron beam time was devoted to these measurements. Table 6.8 gives a breakdown of the approximate amount of beam time used for each part of these measurements (excluding detector and electronics setup, beam profile scans, etc.).

Target	E_n (MeV)	Beam Time (h)
^{235}U	8	290
	10	165
	11	50
	12	55
	14	75
^{238}U	5	30
	6	45
	8	50
	10	115
	12	30
	14	75
Empty	12	60
^{56}Fe	8	15
	12	15

Table 6.8: Breakdown of beam time used in these measurements.

Chapter 7

Conclusion

Neutron-induced partial γ-ray cross sections have been measured for ^{238}U$(n, n'\gamma)^{238}$U, ^{238}U$(n, 2n\gamma)^{237}$U, and ^{235}U$(n, 2n\gamma)^{234}$U using high purity germanium clover and planar detectors and a pulsed, monoenergetic neutron beam at Triangle Universities Nuclear Laboratory. Partial cross sections were determined as a function of incident neutron energy for E_n between 5 and 14 MeV. Cross sections were extracted from γ-ray yields, and corrections for detector efficiency, internal conversion, attenuation of the the γ-rays in the target, angular distribution, and deadtime were accounted for. Neutron flux was determined from the concurrent measurement of γ-ray yields from the 846.77 keV ($2^+ \rightarrow 0^+$) transition in ^{56}Fe.

In total, partial cross sections for eleven separate transition were measured for incident neutron energies between 5 and 14 MeV. Results are generally in good agreement with existing data with the exception of cross sections for the two measured ^{238}U$(n, 2n\gamma)^{237}$U transitions. Experimental data was compared with GNASH and TALYS model calculations and were generally found to be in good agreement. Cross sections for transitions from levels with relatively high spin – e.g. the 244.2 keV ($10^+ \rightarrow 8^+$) transition in ^{234}U – clearly show the need for statistical models to incorporate the effect of multistep direct preequilibrium spin distributions in order to accurately calculate cross sections for higher incident neutron energies. Further tuning of the statitical codes is suggested in order to more accurately reproduce the measured partial cross sections in order to better understand the behavior of the total reaction-channel cross sections in regions where little or no data exists.

Appendix A

Sample Model Code Inputs

A.1 GNASH

A.1.1 ^{235}U input

```
n+U-235 sensivity calculations for AFCI
gn9cp8 04/10/06
   1   0   0   3   1   1   0   0   1   0   0   0   0   0   1
   0   0   0   0   0 126   1   0   0   0   0   0   1   0   0   0   0   0   0
   5   1   2   1   0   0   1   0   0   1   1   1   0   0   2   0   0   1
   2   0   5   5
1.000     92235.000 0.100     0         0         0         0         0
    0.0888    -1.000     0.000     0.000     0.000     0.000
  60   0   0
     0.010     0.030     0.050     0.100     0.150     0.200     0.250     0.300
     0.350     0.400     0.450     0.500     0.550     0.600     0.650     0.700
     0.750     0.800     0.850     0.900     1.000     1.200     1.500     2.000
     2.500     3.000     3.500     4.000     4.500     5.000     5.500     6.000
     6.500     7.000     7.500     8.000     8.500     9.000     9.500    10.000
    10.500    11.000    11.500    12.000    12.500    13.000    13.500    14.000
    14.500    15.000    15.500    16.000    16.500    17.000    17.500    18.000
    18.500    19.000    19.500    20.000
92236.0   3.0       0.0       0.0       0.352
0.0       0.0          28.2984       0.0     0.000  -100.000  -100.000     0.000
-0.0601587 0.3914840   4.18941     0.000     1.140     0.000
1.0       0.0          28.3080      30.0     0.500  -100.000  -100.000     4.000
-0.8150270 0.3866360   3.28809     0.000     0.250     0.000
99.0      0.0          28.2984      15.0     1.000  -100.000  -100.000     0.000
-0.0601587 0.3914840   4.18941     0.000     1.140     0.000
92235.0   3.0       1.0       2.0       0.035
0.0       0.0          28.3080      30.0     0.500  -100.000  -100.000     0.000
-0.8150270 0.3866360   3.28809     0.000     0.250     0.000
1.0       0.0          29.0000       0.0     0.000     0.000     0.000     4.000
```

```
 0.0000000 0.0000000   0.00000     0.000     1.200     0.000
99.0       0.0         28.3080       0.0     0.000     0.000     0.000     0.000
 0.0000000 0.0000000   0.00000     0.000     0.630     0.000
92234.0    3.0       2.0       2.0       0.000
0.0        0.0         29.0000       0.0     0.000     0.000     0.000     0.000
 0.0000000 0.0000000   0.00000     0.000     1.200     0.000
1.0        0.0         29.0000       0.0     0.000     0.000     0.000     4.000
 0.0000000 0.0000000   0.00000     0.000     0.400     0.000
99.0       0.0         29.0000       0.0     0.000     0.000     0.000     0.000
 0.0000000 0.0000000   0.00000     0.000     1.200     0.000
92233.0    3.0       3.0       2.0       0.000
0.0        0.0         29.0000       0.0     0.000     0.000     0.000     0.000
 0.0000000 0.0000000   0.00000     0.000     0.400     0.000
1.0        0.0          0.0000       0.0     0.000     0.000     0.000     4.000
 0.0000000 0.0000000   0.00000     0.000     0.000     0.000
99.0       0.0         29.0000       0.0     0.000     0.000     0.000     0.000
 0.0000000 0.0000000   0.00000     0.000     1.600     0.000
92232.0    2.0       4.0       2.0       0.000
0.0        0.0         29.0000       0.0     0.000     0.000     0.000     0.000
 0.0000000 0.0000000   0.00000     0.000     1.290     0.000
99.0       0.0         29.0000       0.0     0.000     0.000     0.000     0.000
 0.0000000 0.0000000   0.00000     0.000     1.290     0.000
        e1       1.0       0.0
    10.900     2.450    14.100     4.000     1.250     0.000     0.000     0.000
     0.300     0.000     0.250     0.000     0.000     0.000     0.000     0.000
     1.600    18.150     0.000     0.000     0.000     0.000     0.000     0.000
     5.570     5.490
     0.900     0.500
     2.150     2.150
    30.000
     0.000       0.0
     0.024       2.0
     0.080       4.0
     0.168       6.0
     0.288       8.0
     0.440      10.0
     0.150      -1.0
     0.174      -3.0
```

```
  0.230       -5.0
  0.318       -7.0
  0.438       -9.0
  0.180        2.0
  0.204        3.0
  0.236        4.0
  0.276        5.0
  0.324        6.0
  0.380        7.0
  0.444        8.0
  0.516        9.0
  0.596       10.0
  0.450       -1.0
  0.466       -2.0
  0.490       -3.0
  0.522       -4.0
  0.562       -5.0
  0.610       -6.0
  0.666       -7.0
  0.730       -8.0
  0.802       -9.0
  0.880      -10.0
  5.560     5.460
  0.850     0.550
  2.500     2.000
 -1.000
5
  0.000       5.5
  0.031      -2.5
  0.089       0.5
  0.114       0.5
  0.128       1.5
5
  0.000       5.5
  0.001       0.5
  0.011      -2.5
  0.020       1.5
  0.128      -3.5
```

```
  5.150     5.050
  0.700     0.500
  1.000     1.000
 -1.000
4
  0.000       0.0       1.0
  0.200      -0.0      -1.0
  0.600       2.0
  1.000      -1.0
4
  0.000       0.0       1.0
  0.200      -0.0      -1.0
  0.600       2.0
  1.000      -1.0
  5.370     5.170
  0.850     0.550
  5.000     2.000
 -1.000
2
  0.000       2.5
  0.010      -2.5
2
  0.000       2.5
  0.010      -2.5
  5.700     5.200
  1.100     0.900
  5.000     2.000
 -1.000
4
  0.000       0.0       1.0
  0.300      -0.0      -1.0
  0.700       2.0
  0.900      -1.0
4
  0.000       0.0       1.0
  0.300      -0.0      -1.0
  0.700       2.0
  0.900      -1.0
```

A.1.2 ^{238}U input

```
n+U-238 sensivity calculations for AFCI
GN9CP8 -- Jun 26, 2006 -- 11:40
   1   0   0   3   1   1   0   0   1   0   0   0   0   0   1
   0   0   0   0   0 103   1   1   0   0   1   0   1   0   1   0   0   0   0
   5   3   3   1   0   0   1   0   0   1   0   1   0   0   1   0   0   1
   2   0   4   5
1.000     92238.000 0.100     0         0         0         0         0
    0.0888    -1.000     1.000     0.000     0.000     0.000
  61   0   0
     0.001     0.010     0.030     0.050     0.100     0.150     0.200     0.250
     0.300     0.350     0.400     0.450     0.500     0.550     0.600     0.650
     0.700     0.750     0.800     0.850     0.900     1.000     1.200     1.500
     2.000     2.500     3.000     3.500     4.000     4.500     5.000     5.500
     6.000     6.500     7.000     7.500     8.000     8.500     9.000     9.500
    10.000    10.500    11.000    11.500    12.000    12.500    13.000    13.500
    14.000    14.500    15.000    15.500    16.000    16.500    17.000    17.500
    18.000    18.500    19.000    19.500    20.000
92239.0   3.0       0.0       0.0       -0.00697
0.0       12.0        -20.9000      0.0    0.0000     0.000     0.000     0.000
 0.0000000 0.0000000   0.00000     0.000     0.000     0.000
1.0       0.0         -3.5000      23.0    1.1126     0.000     0.000     4.000
 0.0000000 0.0000000   0.00000     0.000     0.000     0.000
99.0      0.0         29.0880      18.0    0.3000     0.000     0.000     0.000
 0.0000000 0.0000000   0.00000     0.000     0.640     0.300
92238.0   3.0       1.0       2.0       0.00000
0.0       0.0         -3.5000      23.0    1.1126     0.000     0.000     0.000
 0.0000000 0.0000000   0.00000     0.000     0.000     0.000
1.0       26.0        -14.7000      0.0    0.0000     0.000     0.000     4.000
 0.0000000 0.0000000   0.00000     0.000     0.000     0.000
99.0      0.0         27.3640       8.0    0.5000     0.000     0.000     0.000
 0.0000000 0.0000000   0.00000     0.000     1.000     0.500
92237.0   3.0       2.0       2.0       0.00000
0.0       26.0        -14.7000      0.0    0.0000     0.000     0.000     0.000
 0.0000000 0.0000000   0.00000     0.000     0.000     0.000
1.0       26.0         -0.4400      0.0    0.0000     0.000     0.000     4.000
 0.0000000 0.0000000   0.00000     0.000     0.000     0.000
```

```
99.0       0.0           29.7660       24.0     0.3000      0.000      0.000      0.000
 0.0000000 0.0000000    0.00000      0.000      0.740      0.300
92236.0    3.0        3.0        2.0        0.00000
0.0        26.0          -0.4400        0.0     0.0000      0.000      0.000      0.000
 0.0000000 0.0000000    0.00000      0.000      0.000      0.000
1.0        26.0         -10.6000        0.0     0.0000      0.000      0.000      4.000
 0.0000000 0.0000000    0.00000      0.000      0.000      0.000
99.0       0.0           28.5320        9.0     0.5000      0.000      0.000      0.000
 0.0000000 0.0000000    0.00000      0.000      1.140      0.500
92235.0    1.0        4.0        2.0        0.00000
0.0        26.0         -10.6000        0.0     0.0000      0.000      0.000      0.000
 0.0000000 0.0000000    0.00000      0.000      0.000      0.000
        e1        1.0        0.0
        m1        1.0        0.0
        e2        1.0        0.0
    10.770     2.370    13.800     5.130     1.476     0.000     0.000     0.000
     0.311     0.000     0.000     0.000     0.000     0.000     0.000     0.000
     1.200    17.680     0.000     0.000     0.000     0.000     0.000     0.000
     6.000     5.300
     0.550     0.550
     5.000     2.000
    -1.000
  14
     0.000       1.5
     0.000       0.5
     0.038      -3.5
     0.045      -2.5
     0.114       0.5
     0.127       5.5
     0.260      -2.5
     0.375       0.5
     0.386      -3.5
     0.519       1.5
     0.524      -1.5
     0.702      -0.5
     0.810       2.5
     0.853      -1.5
  11
```

```
  0.000       1.5
  0.004      -3.5
  0.009       0.5
  0.033       5.5
  0.260      -2.5
  0.283      -2.5
  0.392       4.5
  0.509       0.5
  0.515       0.5
  0.600      -3.5
  0.753      -1.5
  6.123     5.923
  1.100     0.750
  5.000     2.000
 -1.000
 4
  0.000       0.0       1.0
  0.300       0.0      -1.0
  0.700       2.0
  0.900      -1.0
 4
  0.000       0.0       1.0
  0.300       0.0      -1.0
  0.700       2.0
  0.900      -1.0
  5.690     5.520
  0.750     0.550
  5.000     2.000
 -1.000
14
  0.000       0.5
  0.000       1.5
  0.047      -3.5
  0.054      -2.5
  0.114       5.5
  0.128       0.5
  0.243      -2.5
  0.356       0.5
```

```
    0.407      -3.5
    0.503      -1.5
    0.542       1.5
    0.727      -0.5
    0.787       2.5
    0.878      -1.5
 11
    0.000       0.5
    0.007       5.5
    0.009       1.5
    0.026      -3.5
    0.183      -2.5
    0.302       4.5
    0.372      -2.5
    0.413       0.5
    0.618       0.5
    0.647      -1.5
    0.706      -3.5
    5.910     5.910
    1.100     0.750
    5.000     2.000
   -1.000
  4
    0.000       0.0       1.0
    0.300       0.0      -1.0
    0.500       2.0
    0.900      -1.0
  4
    0.000       0.0       1.0
    0.300       0.0      -1.0
    0.500       2.0
    0.900      -1.0
```

A.2 TALYS

A.2.1 ^{235}U input

```
projectile n
```

```
element u
mass 235
energy range
channels y
outgamdis y
outdensity y
outfission y
outomp y
fisbar 92 236 5.470
fisbar 92 236 5.390 2
fishw 92 236 0.900
fishw 92 236 0.500 2
fisbar 92 235 5.270
fisbar 92 235 5.190 2
fishw 92 235 0.900
fishw 92 235 0.500 2
fisbar 92 234 5.270
fisbar 92 234 5.190 2
fishw 92 234 0.900
fishw 92 234 0.500 2
axtype 92 236 3
axtype 92 236 2 2
axtype 92 235 3
axtype 92 235 2 2
axtype 92 234 3
axtype 92 234 2 2
preeqmode 4
```

A.2.2 ^{238}U input

```
projectile n
element u
mass 238
energy range
channels y
outgamdis y
```

```
outdensity y
outfission y
outomp y
preeqmode 4
fisbar 92 239 5.7
fisbar 92 239 5.0 2
fishw 92 239 0.900
fishw 92 239 0.500 2
fisbar 92 238 5.6
fisbar 92 238 4.6 2
fishw 92 238 0.500
fishw 92 238 0.500 2
fisbar 92 237 5.4
fisbar 92 237 4.7 2
fishw 92 237 0.900
fishw 92 237 0.500 2
```

A.3 AVALANCHE

A.3.1 AVA_FUS

```
      INPUT FILE FOR PROGRAM "AVA_FUS" FOR ( n+235U at 10.MeV )
 target     : mass number, spin, parity, mass excess (in MeV)
                235.       3.5    1           40.9205
 projectile : ...........  ....  ......  .....................
                  1.       0.5    2            8.0713
 projectile kinetic energy in LAB (in MeV)
                                        10.
 binding energy of the projectile in the compound nucleus (MeV)
                                                                 6.54545
 number of en.bins, en.step(MeV), energy initial-value(MeV)
         120            .50                  0.
 number of spin values, spin initial-value
         19                  0.0
 number of transmission coefficients to be read
         28
 transmission coefficients for L=0..27
```

```
      6.0783e-01
      7.8100e-01
      6.1632e-01
      7.6434e-01
      6.3744e-01
      7.6959e-01
      7.0393e-01
      6.9574e-01
      8.1455e-01
      5.9586e-01
      9.2115e-01
      4.7196e-01
      8.9739e-01
      1.6406e-01
      1.3355e-01
      2.6610e-01
      3.9415e-02
      7.7073e-03
      6.9070e-04
      2.1093e-02
      9.5053e-04
      7.0619e-05
      7.4584e-06
      7.8278e-05
      7.7232e-06
      7.9477e-07
      0.0000e+00
      8.0248e-07
 output file name
236U_entry_10.dat
```

A.3.2 AVA_CAS

```
        INPUT FILE FOR "AVA_CAS" FOR THE 236U NUCLEUS
Number of decay channels
                        2
Emitted particles     Mass    Charge    Spin   Ipar    Bind.en.(MeV)
                       0.       0.       0.     0         0.
```

```
                      1.       0.       .5     2         6.5455
Initial nucleus       Mass     Charge
                      236.     92.
Number of energy bins ...... Energy step ...... Initial energy
                     120                .50                   0.
Number of spins
                     19
The lowest spin in various final nuclei
                                        0.0
                                        3.5
Photon Strength Function Option ... E1 .... M1 .... E2
                                    3       0       0
Gamma-channel : SP strengths (1/MeV**3)... E1 ........... M1
                                         8.68e-8         1.82e-8
               E1 and M1 Giant Resonance Parameters
Number of resonance peaks ..............  E1 ..........  M1
                                         2              1
E1 :     Res.cross sect.(b) ... Res.energy(MeV) ..... Damp.Width(MeV)
              .2710                  10.92                2.550
              .4150                  13.78                4.880
M1 :     ...................     ...............       ...............
              .004                    6.63                4.0
Fermi liquid sum-rule parameter
                                 .7
Single particle E2 strength (1/MeV**5)  statistical   collective
                                         3.e-11        300.e-11
Width of collective E2 band (MeV)
                                  4.
Pairing energy (MeV)          GS mass shell correction (MeV)
                    1.180                             -4.22
                    0.690                             -4.11
CTF :  spin window en.limit(MeV) temper.(MeV) en.shift(MeV) sp.cutoff
       0.0   20.0       1.47          0.442      -0.271        4.11
       0.5   20.5       0.97          0.428      -0.926        4.52
Files with entry-feeding-flow and entry-orientation-coefficients
               1
```

```
236U_entry.dat
File with transmission coefficients
236U_tc.dat
Files with quasicont.edges and dis.levels (blank = ECONT=0, no dis.lev.)
236U_dl.dat
235U_dl.dat
Output files
236U_total.dat
235U_entry.dat
```

Appendix B

MCNPX Input Files

B.1 Detector Efficiency

```
Planar Detector
c  Tony Hutcheson
c  May 23, 2007
c
c ------------------------------ Cell Definitions ------------------------------
1   2   -2.6989   -1 2 3 4                                          $ Al Endcap
2   4   -1.848    -3                                               $ Be Window
3   5   -1.4      -5 6                                           $ Mylar Lining
4   2   -2.6989   -6 7 8                                        $ Al Collimator
5   6   -2.34     -9                                            $ Boron Contact
6   3   -5.323    -10                                              $ Ge Crystal
7   7   -0.534    -11                                              $ Li Contact
8   0             -4:(-2 5):-8:(-7 9 10 11)                          $ Vaccuum
10  8   -1.38     -12                                  $ Plastic Source Capsule
90  0              99                                                 $ Void
99  1   -0.00129   #1 #2 #3 #4 #5 #6 #7 #8 #10 #90

c --------------------------- Surface Definitions ----------------------------
1  1 rcc   0.00 0.00 0.000   0.00 0.00 6.000   3.500          $ Al Endcap Outer
2  1 rcc   0.00 0.00 0.127   0.00 0.00 5.746   3.373          $ Al Endcap Inner
3  1 rcc   0.00 0.00 0.000   0.00 0.00 0.025   2.550                $ Be Window
4  1 rcc   0.00 0.00 0.025   0.00 0.00 0.102   1.900           $ Window Opening
5  1 rcc   0.00 0.00 0.6245  0.00 0.00 5.2485  2.7525            $ Mylar Lining
6  1 rcc   0.00 0.00 0.627   0.00 0.00 5.246   2.750      $ Al Collimator Outer
7  1 rcc   0.00 0.00 0.827   0.00 0.00 5.046   2.550      $ Al Collimator Inner
8  1 rcc   0.00 0.00 0.627   0.00 0.00 0.200   1.800       $ Collimator Opening
9  1 rcc   0.00 0.00 0.827   0.00 0.00 0.00003 2.550            $ Boron Contact
```

```
10 1 rcc   0.00 0.00 0.82703 0.00 0.00 1.300   1.800              $ Ge Crystal
11 1 rcc   0.00 0.00 2.12703 0.00 0.00 0.060   1.800              $ Li Contact
12 2 rcc   0.0 0.00 -0.3175    0.0 0.0 0.635   1.27     $ Calib. Source Capsule
99   so    150

c ------------------------------ Material List --------------------------------
c   Material #1 (Air)
M1    7000.04p    0.75527   GAS=1   &
      8000.04p    0.23178   GAS=1   &
     18000.04p    0.01283   GAS=1   &
      6000.04p    0.00012   GAS=1
c   Material #2 (Aluminum)
M2   13000.04p   1.0
c   Material #3 (Germanium)
M3   32000.04p   1.0
c   Material #4 (Beryllium)
M4    4000.04p   1.0
c   Material #5 (Mylar)
M5    1000.04p   0.067
      6000.04p   0.400
      8000.04p   0.533
c   Material #6 (Boron)
M6    5000.04p   1.0
c   Material #7 (Lithium)
M7    3000.04p   1.0
c   Material #8  (Plastic)
M8    1000.04p   0.50              &
      6000.04p   0.33              &
     17000.04p   0.17
c
imp:p,e 1 1 1 1 1 1 1 1 1 0 1
mode p e
c
*TR1  0.000 0.000 10.100   0 90 90   90 0 90   90 90 0
*TR2  0.000 0.129 -0.483   0 90 90   90 0 90   90 90 0
```

```
c
c ---------------------------------- Source Definition ------------------------
c                                    (5mm diameter source)
sdef   par=p   erg=D1   pos=0 0.129 -0.483  axs=0 0 1  rad=D2
SI1 L  0.03952 0.04012 0.04658 0.05316 0.05954 0.07961 0.08100 0.08803        &
       0.10000 0.12178 0.12206 0.13647 0.16061 0.17500 0.20000 0.22324        &
       0.24470 0.27640 0.30285 0.32500 0.34428 0.35601 0.38385 0.40000        &
       0.41112 0.45000 0.47500 0.50000 0.52500 0.55000 0.58626 0.60000        &
       0.62500 0.66166 0.68867 0.70000 0.72500 0.75000 0.77890 0.80000        &
       0.82500 0.86737 0.90000 0.92500 0.97500
SP1 D  1 1 1 1 1 1 1 1 1 1 1 1 1 1 1 1 1 1 1 1 1 1 1 1 1 1 1 1 1 1 1 1 1  &
       1 1 1 1 1 1 1 1 1 1
SI2    0.25
c
F8:P  6
E8  0.0 4096I 1.000
CTME 600
```

B.2 Attenuation in Target

B.2.1 Uranium Target

```
235U Measurement Simulation
c  Tony Hutcheson
c  September 18, 2007
c
c ------------------------------ Cell Definitions ------------------------------
1   2   -2.6989   (-1 5 3 4):(-2 6 4):(-7 3 4)         TRCL=1        $ Al Walls
2   4   -7.13     (-10:-11) 8 9                        TRCL=1             $ BGO
3   1   -0.00129  (-5 10 11):(-6 11):(-8 7):(-9 7)     TRCL=1     $ Inner Space
4   3   -5.323     -21 -25 31                          TRCL=1          $ Ge 2Q2
5   3   -5.323     -22 -26 32                          TRCL=1          $ Ge 2Q3
6   3   -5.323     -23 -27 33                          TRCL=1          $ Ge 2Q4
7   3   -5.323     -24 -28 34                          TRCL=1          $ Ge 2Q1
8   2   -2.6989    -30 29                              TRCL=1          $ Al Cap
9   2   -2.6989   (-31 35):(-32 36):(-33 37):(-34 38)  TRCL=1        $ Al Inner
```

```
10  0   (-25 21):(-26 22):(-27 23):(-28 24):(-29 25 26 27 28):-35:-36:-37:-38 &
                                                        TRCL=1   $ Inner Vaccuum
11  LIKE 1 BUT                                          TRCL=2
12  LIKE 2 BUT                                          TRCL=2
13  LIKE 3 BUT                                          TRCL=2
14  LIKE 4 BUT                                          TRCL=2
15  LIKE 5 BUT                                          TRCL=2
16  LIKE 6 BUT                                          TRCL=2
17  LIKE 7 BUT                                          TRCL=2
18  LIKE 8 BUT                                          TRCL=2
19  LIKE 9 BUT                                          TRCL=2
20  LIKE 10 BUT                                         TRCL=2
21  2   -2.6989    -41 42 43 44                         TRCL=3       $ Al Endcap
22  5   -1.848     -43                                  TRCL=3       $ Be Window
23  6   -1.4       -45 46                               TRCL=3    $ Mylar Lining
24  2   -2.6989    -46 47 48                            TRCL=3   $ Al Collimator
25  7   -2.34      -49                                  TRCL=3   $ Boron Contact
26  3   -5.323     -50                                  TRCL=3      $ Ge Crystal
27  8   -0.534     -51                                  TRCL=3      $ Li Contact
28  0              -44:(-42 45):-48:(-47 49 50 51)      TRCL=3         $ Vaccuum
31  LIKE 21 BUT                                         TRCL=4
32  LIKE 22 BUT                                         TRCL=4
33  LIKE 23 BUT                                         TRCL=4
34  LIKE 24 BUT                                         TRCL=4
35  LIKE 25 BUT                                         TRCL=4
36  LIKE 26 BUT                                         TRCL=4
37  LIKE 27 BUT                                         TRCL=4
38  LIKE 28 BUT                                         TRCL=4
50  9   -7.86      -60                                              $ Fe Target
51  10  -19        -61                                               $ U Target
90  0               90                                                  $ Void
99  1   -0.00129   #1  #2  #3  #4  #5  #6  #7  #8  #9  #10                  &
                   #11 #12 #13 #14 #15 #16 #17 #18 #19 #20                 &
                   #21 #22 #23 #24 #25 #26 #27 #28                         &
                   #31 #32 #33 #34 #35 #36 #37 #38 #50 #51 #90           $ Air

c --------------------------- Surface Definitions -----------------------------
```

```
1    arb   5.950  5.950 0.000   5.950 -5.950 0.000   -5.950 -5.950 0.000      &
          -5.950  5.950 0.000   10.60  10.60 12.77    10.60 -10.60 12.77      &
          -10.60 -10.60 12.77  -10.60  10.60 12.77                            &
           1234 5678 1265 4378 1584 2673                          $ Al Walls #1
2    box   10.60  10.60 12.77  -21.20  0.000 0.000    0.000 -21.20 0.000      &
           0.000  0.000 12.93                                     $ Al Walls #2
3    box   4.25 4.25 0.00   -8.50 0 0   0 -8.50 0   0 0 1.00  $ Inner Hollow #1
4    box   5.10 5.10 1.00   -10.2 0 0   0 -10.2 0   0 0 24.7  $ Inner Hollow #2
5    arb   6.045  6.045 0.700   6.045 -6.045 0.700   -6.045 -6.045 0.700      &
          -6.045  6.045 0.700   10.45  10.45 12.77    10.45 -10.45 12.77      &
          -10.45 -10.45 12.77  -10.45  10.45 12.77                            &
           1234 5678 1265 4378 1584 2673                        $ Inner Wall #1
6    box   10.45 10.45 12.77   -20.9 0 0   0 -20.9 0   0 0 12.85              &
                                                              $ Inner Wall #2
7    box   5.18  5.18 0.700  -10.36 0 0   0 -10.36 0   0 0 24.92              &
                                                              $ Inner Wall #3
8    arb   5.18  5.18 0.700   5.18 -5.18 0.70  -5.18 -5.18 0.70               &
          -5.18  5.18 0.700   5.25 5.25 2.173   5.25 -5.25 2.173              &
          -5.25 -5.25 2.173  -5.25 5.25 2.173   1234 5678 1265 4378 1584 2673
                                                               $ Inner BGO #1
9    arb   5.25  5.25 2.173   5.25 -5.25 2.173 -5.25 -5.25 2.173              &
          -5.25  5.25 2.173   7.14  7.14 25.62  7.14 -7.14 25.62              &
          -7.14 -7.14 25.62  -7.14  7.14 25.62  1234 5678 1265 4378 1584 2673 &
                                                               $ Inner BGO #2
10   arb   5.975  5.975 0.70    5.975 -5.975 0.70   -5.975 -5.975 0.70        &
          -5.975  5.975 0.70    7.450  7.450 4.76    7.450 -7.450 4.76        &
          -7.450 -7.450 4.76   -7.450  7.450 4.76                            &
           1234 5678 1265 4378 1584 2673                        $ Outer BGO #1
11   arb   7.450  7.450 4.76    7.450 -7.450 4.76   -7.450 -7.450 4.76        &
          -7.450  7.450 4.76    9.128  9.128 25.62   9.128 -9.128 25.62       &
          -9.128 -9.128 25.62  -9.128  9.128 25.62                            &
           1234 5678 1265 4378 1584 2673                        $ Outer BGO #2
21   rcc   2.26  2.26 4.40   0.00 0.00 8.00   2.50                      $ Ge Q1
22   rcc  -2.26  2.26 4.40   0.00 0.00 8.00   2.50                      $ Ge Q2
23   rcc  -2.26 -2.26 4.40   0.00 0.00 8.00   2.50                      $ Ge Q3
24   rcc   2.26 -2.26 4.40   0.00 0.00 8.00   2.50                      $ Ge Q4
25   box   0.03  0.03 4.40   4.50 0.00 0.00   0.00   4.50 0.00   0.00 0.00 8.00
```

```
26   box  -0.03  0.03 4.40  -4.50 0.00 0.00   0.00   4.50 0.00   0.00 0.00 8.00
27   box  -0.03 -0.03 4.40  -4.50 0.00 0.00   0.00  -4.50 0.00   0.00 0.00 8.00
28   box   0.03 -0.03 4.40   4.50 0.00 0.00   0.00  -4.50 0.00   0.00 0.00 8.00
29   box  -4.90 -4.90 3.75   9.80 0.00 0.00   0.00   9.80 0.00   0.00 0.00 8.65
30   box  -5.05 -5.05 3.60   10.1 0.00 0.00   0.00   10.1 0.00   0.00 0.00 8.95
31   rcc   2.26  2.26 5.90   0.00 0.00 6.50   0.50           $ Au Outer Surface
32   rcc  -2.26  2.26 5.90   0.00 0.00 6.50   0.50           $ Au Outer Surface
33   rcc  -2.26 -2.26 5.90   0.00 0.00 6.50   0.50           $ Au Outer Surface
34   rcc   2.26 -2.26 5.90   0.00 0.00 6.50   0.50           $ Au Outer Surface
35   rcc   2.26  2.26 5.95   0.00 0.00 6.45   0.45           $ Au Inner Surface
36   rcc  -2.26  2.26 5.95   0.00 0.00 6.45   0.45           $ Au Inner Surface
37   rcc  -2.26 -2.26 5.95   0.00 0.00 6.45   0.45           $ Au Inner Surface
38   rcc   2.26 -2.26 5.95   0.00 0.00 6.45   0.45           $ Au Inner Surface
41   rcc   0.00 0.00 0.000   0.00 0.00 6.000   3.500          $ Al Endcap Outer
42   rcc   0.00 0.00 0.127   0.00 0.00 5.746   3.373          $ Al Endcap Inner
43   rcc   0.00 0.00 0.000   0.00 0.00 0.025   2.550                $ Be Window
44   rcc   0.00 0.00 0.025   0.00 0.00 0.102   1.900           $ Window Opening
45   rcc   0.00 0.00 0.6245  0.00 0.00 5.2485  2.7525            $ Mylar Lining
46   rcc   0.00 0.00 0.627   0.00 0.00 5.246   2.750      $ Al Collimator Outer
47   rcc   0.00 0.00 0.827   0.00 0.00 5.046   2.550      $ Al Collimator Inner
48   rcc   0.00 0.00 0.627   0.00 0.00 0.200   1.800       $ Collimator Opening
49   rcc   0.00 0.00 0.827   0.00 0.00 0.00003 2.550            $ Boron Contact
50   rcc   0.00 0.00 0.82703 0.00 0.00 1.300   1.800               $ Ge Crystal
51   rcc   0.00 0.00 2.12703 0.00 0.00 0.060   1.800               $ Li Contact
60 5 box   1.2825 1.275 0   -2.565 0 0  0 -2.55 0   0 0 0.01        $ Fe Target
61 5 box   1.30 1.30 0.00   -2.60 0 0   0 -2.60 0   0 0 -0.012       $ U Target
90   so    50

c ------------------------------ Material List --------------------------------
c   Material #1 (Air)
M1    7000.04p    0.75527   GAS=1   &
      8000.04p    0.23178   GAS=1   &
     18000.04p    0.01283   GAS=1   &
      6000.04p    0.00012   GAS=1
c   Material #2 (Aluminum)
```

```
M2   13000.04p    1.0
c   Material #3 (Germanium)
M3   32000.04p   1.0
c   Material #4 (BGO)
M4    8000.04p    0.63158          &
     32000.04p    0.15789          &
     83000.04p    0.21053
c   Material #5 (Beryllium)
M5    4000.04p   1.0
c   Material #6 (Mylar)
M6    1000.04p   0.067
      6000.04p   0.400
      8000.04p   0.533
c   Material #7 (Boron)
M7    5000.04p   1.0
c   Material #8 (Lithium)
M8    3000.04p   1.0
c   Material #9 (Fe)
M9   26000.04p   1.0
c   Material #10 (Uranium)
M10   92000.04p   1.0
c
*TR1  0.000  8.768   8.768    0 90 90   90  -45 -135   90   45  -45
*TR2  0.000 -8.485  -8.485    0 90 90   90  135   45   90  225  135
*TR3  0.000 -9.756   2.614    0 90 90   90   75  -15   90  165   75
*TR4  0.000  9.154  -4.268    0 90 90   90 -115 -205   90  -25 -115
*TR5  0.000  0.0000  0.0000   0 90 90   90   20  -70   90  110   20
c
imp:p,e 1 1 1 1 1 1 1 1 1 1 1 1 1 1 1 1 1 1 1 1 1 1 1 1 1 1 1 1 1 1 1 &
        1 1 1 0 1
mode p e
c
c ---------------------------------- Source Definition ------------------------
sdef   cel=51   par=p   erg=D1   pos=0 0 0   axs=0 -0.364 1   rad=D2  ext=D3
SI1 L 0.1527 0.2442
```

```
SP1 D 1 1
SI2   2
SI3   -0.02 0.02
c
F8:P 4
E8 0 4096I 1.5
F18:P 5
E18 0 4096I 1.5
F28:P 6
E28 0 4096I 1.5
F38:P 7
E38 0 4096I 1.5
F48:P 14
E48 0 4096I 1.5
F58:P 15
E58 0 4096I 1.5
F68:P 16
E68 0 4096I 1.5
F78:P 17
E78 0 4096I 1.5
F88:P 26
E88 0 4096I 1.5
F98:P 36
E98 0 4096I 1.5
CTME 700
```

B.2.2 Air Target

```
235U Measurement Simulation
c  Tony Hutcheson
c  September 18, 2007
c
c ----------------------------- Cell Definitions ------------------------------
1   2   -2.6989   (-1 5 3 4):(-2 6 4):(-7 3 4)         TRCL=1        $ Al Walls
2   4   -7.13     (-10:-11) 8 9                        TRCL=1             $ BGO
3   1   -0.00129  (-5 10 11):(-6 11):(-8 7):(-9 7)     TRCL=1     $ Inner Space
4   3   -5.323     -21 -25 31                          TRCL=1          $ Ge 2Q2
5   3   -5.323     -22 -26 32                          TRCL=1          $ Ge 2Q3
```

```
6   3   -5.323     -23 -27 33                              TRCL=1          $ Ge 2Q4
7   3   -5.323     -24 -28 34                              TRCL=1          $ Ge 2Q1
8   2   -2.6989    -30 29                                  TRCL=1          $ Al Cap
9   2   -2.6989   (-31 35):(-32 36):(-33 37):(-34 38)      TRCL=1        $ Al Inner
10  0   (-25 21):(-26 22):(-27 23):(-28 24):(-29 25 26 27 28):-35:-36:-37:-38 &
                                                           TRCL=1   $ Inner Vaccuum
11  LIKE 1 BUT                                             TRCL=2
12  LIKE 2 BUT                                             TRCL=2
13  LIKE 3 BUT                                             TRCL=2
14  LIKE 4 BUT                                             TRCL=2
15  LIKE 5 BUT                                             TRCL=2
16  LIKE 6 BUT                                             TRCL=2
17  LIKE 7 BUT                                             TRCL=2
18  LIKE 8 BUT                                             TRCL=2
19  LIKE 9 BUT                                             TRCL=2
20  LIKE 10 BUT                                            TRCL=2
21  2   -2.6989    -41 42 43 44                            TRCL=3       $ Al Endcap
22  5   -1.848     -43                                     TRCL=3       $ Be Window
23  6   -1.4       -45 46                                  TRCL=3    $ Mylar Lining
24  2   -2.6989    -46 47 48                               TRCL=3   $ Al Collimator
25  7   -2.34      -49                                     TRCL=3   $ Boron Contact
26  3   -5.323     -50                                     TRCL=3      $ Ge Crystal
27  8   -0.534     -51                                     TRCL=3      $ Li Contact
28  0              -44:(-42 45):-48:(-47 49 50 51)         TRCL=3         $ Vaccuum
31  LIKE 21 BUT                                            TRCL=4
32  LIKE 22 BUT                                            TRCL=4
33  LIKE 23 BUT                                            TRCL=4
34  LIKE 24 BUT                                            TRCL=4
35  LIKE 25 BUT                                            TRCL=4
36  LIKE 26 BUT                                            TRCL=4
37  LIKE 27 BUT                                            TRCL=4
38  LIKE 28 BUT                                            TRCL=4
50  1   -0.00129   -60                                                  $ Fe Target
51  1   -0.00129   -61                                                   $ U Target
90  0               90                                                       $ Void
99  1   -0.00129   #1  #2  #3  #4  #5  #6  #7  #8  #9  #10                      &
```

```
                  #11 #12 #13 #14 #15 #16 #17 #18 #19 #20                    &
                  #21 #22 #23 #24 #25 #26 #27 #28                            &
                  #31 #32 #33 #34 #35 #36 #37 #38 #50 #51 #90            $ Air

c --------------------------- Surface Definitions -----------------------------
1    arb   5.950  5.950 0.000   5.950 -5.950 0.000   -5.950 -5.950 0.000      &
          -5.950  5.950 0.000   10.60  10.60 12.77    10.60 -10.60 12.77      &
          -10.60 -10.60 12.77  -10.60  10.60 12.77                            &
           1234 5678 1265 4378 1584 2673                          $ Al Walls #1
2    box   10.60  10.60 12.77  -21.20  0.000 0.000    0.000 -21.20 0.000      &
           0.000  0.000 12.93                                     $ Al Walls #2
3    box   4.25 4.25 0.00   -8.50 0 0   0 -8.50 0   0 0 1.00  $ Inner Hollow #1
4    box   5.10 5.10 1.00   -10.2 0 0   0 -10.2 0   0 0 24.7  $ Inner Hollow #2
5    arb   6.045  6.045 0.700   6.045 -6.045 0.700   -6.045 -6.045 0.700      &
          -6.045  6.045 0.700   10.45  10.45 12.77    10.45 -10.45 12.77      &
          -10.45 -10.45 12.77  -10.45  10.45 12.77                            &
           1234 5678 1265 4378 1584 2673                        $ Inner Wall #1
6    box   10.45 10.45 12.77   -20.9 0 0   0 -20.9 0   0 0 12.85              &
                                                              $ Inner Wall #2
7    box   5.18  5.18 0.700  -10.36 0 0   0 -10.36 0   0 0 24.92              &
                                                              $ Inner Wall #3
8    arb   5.18  5.18 0.700   5.18 -5.18 0.70  -5.18 -5.18 0.70               &
          -5.18  5.18 0.700   5.25 5.25 2.173   5.25 -5.25 2.173              &
          -5.25 -5.25 2.173  -5.25 5.25 2.173   1234 5678 1265 4378 1584 2673
                                                               $ Inner BGO #1
9    arb   5.25  5.25 2.173   5.25 -5.25 2.173 -5.25 -5.25 2.173              &
          -5.25  5.25 2.173   7.14  7.14 25.62  7.14 -7.14 25.62              &
          -7.14 -7.14 25.62  -7.14  7.14 25.62  1234 5678 1265 4378 1584 2673 &
                                                               $ Inner BGO #2
10   arb   5.975  5.975 0.70    5.975 -5.975 0.70   -5.975 -5.975 0.70        &
          -5.975  5.975 0.70    7.450  7.450 4.76    7.450 -7.450 4.76        &
          -7.450 -7.450 4.76   -7.450  7.450 4.76                            &
           1234 5678 1265 4378 1584 2673                        $ Outer BGO #1
11   arb   7.450  7.450 4.76    7.450 -7.450 4.76   -7.450 -7.450 4.76        &
          -7.450  7.450 4.76    9.128  9.128 25.62   9.128 -9.128 25.62       &
          -9.128 -9.128 25.62  -9.128  9.128 25.62                            &
           1234 5678 1265 4378 1584 2673                        $ Outer BGO #2
```

```
21   rcc   2.26  2.26 4.40   0.00 0.00 8.00   2.50                    $ Ge Q1
22   rcc  -2.26  2.26 4.40   0.00 0.00 8.00   2.50                    $ Ge Q2
23   rcc  -2.26 -2.26 4.40   0.00 0.00 8.00   2.50                    $ Ge Q3
24   rcc   2.26 -2.26 4.40   0.00 0.00 8.00   2.50                    $ Ge Q4
25   box   0.03  0.03 4.40   4.50 0.00 0.00   0.00   4.50 0.00   0.00 0.00 8.00
26   box  -0.03  0.03 4.40  -4.50 0.00 0.00   0.00   4.50 0.00   0.00 0.00 8.00
27   box  -0.03 -0.03 4.40  -4.50 0.00 0.00   0.00  -4.50 0.00   0.00 0.00 8.00
28   box   0.03 -0.03 4.40   4.50 0.00 0.00   0.00  -4.50 0.00   0.00 0.00 8.00
29   box  -4.90 -4.90 3.75   9.80 0.00 0.00   0.00   9.80 0.00   0.00 0.00 8.65
30   box  -5.05 -5.05 3.60   10.1 0.00 0.00   0.00   10.1 0.00   0.00 0.00 8.95
31   rcc   2.26  2.26 5.90   0.00 0.00 6.50   0.50           $ Au Outer Surface
32   rcc  -2.26  2.26 5.90   0.00 0.00 6.50   0.50           $ Au Outer Surface
33   rcc  -2.26 -2.26 5.90   0.00 0.00 6.50   0.50           $ Au Outer Surface
34   rcc   2.26 -2.26 5.90   0.00 0.00 6.50   0.50           $ Au Outer Surface
35   rcc   2.26  2.26 5.95   0.00 0.00 6.45   0.45           $ Au Inner Surface
36   rcc  -2.26  2.26 5.95   0.00 0.00 6.45   0.45           $ Au Inner Surface
37   rcc  -2.26 -2.26 5.95   0.00 0.00 6.45   0.45           $ Au Inner Surface
38   rcc   2.26 -2.26 5.95   0.00 0.00 6.45   0.45           $ Au Inner Surface
41   rcc   0.00 0.00 0.000   0.00 0.00 6.000   3.500          $ Al Endcap Outer
42   rcc   0.00 0.00 0.127   0.00 0.00 5.746   3.373          $ Al Endcap Inner
43   rcc   0.00 0.00 0.000   0.00 0.00 0.025   2.550               $ Be Window
44   rcc   0.00 0.00 0.025   0.00 0.00 0.102   1.900           $ Window Opening
45   rcc   0.00 0.00 0.6245  0.00 0.00 5.2485  2.7525            $ Mylar Lining
46   rcc   0.00 0.00 0.627   0.00 0.00 5.246   2.750      $ Al Collimator Outer
47   rcc   0.00 0.00 0.827   0.00 0.00 5.046   2.550      $ Al Collimator Inner
48   rcc   0.00 0.00 0.627   0.00 0.00 0.200   1.800       $ Collimator Opening
49   rcc   0.00 0.00 0.827   0.00 0.00 0.00003 2.550            $ Boron Contact
50   rcc   0.00 0.00 0.82703 0.00 0.00 1.300   1.800               $ Ge Crystal
51   rcc   0.00 0.00 2.12703 0.00 0.00 0.060   1.800               $ Li Contact
60 5 box   1.2825 1.275 0   -2.565 0 0  0 -2.55 0   0 0 0.01        $ Fe Target
61 5 box   1.30 1.30 0.00   -2.60 0 0   0 -2.60 0   0 0 -0.012       $ U Target
90   so    50

c ------------------------------ Material List --------------------------------
c   Material #1 (Air)
```

```
M1    7000.04p    0.75527   GAS=1   &
      8000.04p    0.23178   GAS=1   &
     18000.04p    0.01283   GAS=1   &
      6000.04p    0.00012   GAS=1
c   Material #2 (Aluminum)
M2   13000.04p    1.0
c   Material #3 (Germanium)
M3   32000.04p   1.0
c   Material #4 (BGO)
M4    8000.04p    0.63158           &
     32000.04p    0.15789           &
     83000.04p    0.21053
c   Material #5 (Beryllium)
M5    4000.04p   1.0
c   Material #6 (Mylar)
M6    1000.04p   0.067
      6000.04p   0.400
      8000.04p   0.533
c   Material #7 (Boron)
M7    5000.04p   1.0
c   Material #8 (Lithium)
M8    3000.04p   1.0
c   Material #9 (Fe)
M9   26000.04p   1.0
c   Material #10 (Uranium)
M10   92000.04p   1.0
c
*TR1  0.000  8.768   8.768    0 90 90   90  -45 -135   90   45  -45
*TR2  0.000 -8.485  -8.485    0 90 90   90  135   45   90  225  135
*TR3  0.000 -9.756   2.614    0 90 90   90   75  -15   90  165   75
*TR4  0.000  9.154  -4.268    0 90 90   90 -115 -205   90  -25 -115
*TR5  0.000  0.0000  0.0000   0 90 90   90   20  -70   90  110   20
c
imp:p,e 1 1 1 1 1 1 1 1 1 1 1 1 1 1 1 1 1 1 1 1 1 1 1 1 1 1 1 1 1 1 1 &
        1 1 1 0 1
```

```
mode p e
c
c ---------------------------------- Source Definition ------------------------
sdef   cel=51   par=p   erg=D1   pos=0 0 0   axs=0 -0.364 1   rad=D2  ext=D3
SI1 L 0.1527 0.2442
SP1 D 1 1
SI2   2
SI3   -0.02 0.02
c
F8:P 4
E8 0 4096I 1.5
F18:P 5
E18 0 4096I 1.5
F28:P 6
E28 0 4096I 1.5
F38:P 7
E38 0 4096I 1.5
F48:P 14
E48 0 4096I 1.5
F58:P 15
E58 0 4096I 1.5
F68:P 16
E68 0 4096I 1.5
F78:P 17
E78 0 4096I 1.5
F88:P 26
E88 0 4096I 1.5
F98:P 36
E98 0 4096I 1.5
CTME 700
```

Bibliography

[1] K.W. Allen, P. Bomyer, and J.L. Perkin. *The Interaction of 14 MeV Neutrons with Uranium*. Journal of Nuclear Energy A/B **14**(1961), 100.

[2] V.N. Andreev. *Inelastic Scattering of Neutrons of the Fission Spectrum and Neutrons with an Energy of 0.9 MeV in U2 and Pu239*. Neitronnaya Fizika, Moskva (1961), 287.

[3] R. Arlt, G. Musiol, and D. Hoffman. *Excitation of U-238M Spontaneously Fissionable Isomer by 14 MeV Neutrons*. IAEA Symposium on Physics and Chemistry of Fission, Juelich (1979), B15.

[4] R. Batchelor. *238U Inelastic Cross Section Measurement*. Proceedings of the Physical Society (London) **A69**(1956), 214.

[5] A. Chatterjee, A.L. Athouges, S. Kailas, and M. K. Mehta. *Delayed Fission for the U-238(n,n)U-238-M1 Reaction at 14.5 MeV Neutron Energy*. Physical Review **C23**(1981), 1629.

[6] L. Cranberg and J.S. Levin. *Inelastic Neutron Scattering by U-238*. Physical Review **109**(1958), 2063.

[7] N.P. Glaszkov. *Spectra and Cross Sections of the Neutron Inelastic Scattering in the Energy Range of 0.4-1.2 MeV on the Nuclei U, Th, Hg, W, Sb, Cd, Mo, Nb, Fe*. Atomnaya Energiya **14**(1963), 400.

[8] G.H.R. Kegel, L.E. Beghian, G.P. Couchell, et al. *Neutron Scattering on Heavy Deformed Nuclei*. US DOE Nuclear Data Committee Reports No. 12 (1978), 151.

[9] F.Y. Tsang and R.M. Brugger. *The Differential Scattering Cross Section of U-238 at 144 keV*. Nuclear Science and Engineering **65**(1978), 70.

[10] P.H. White. *The Value of Eta for U-238 with Neutrons of Energy between 12 MeV and 19 MeV*. Journal of Nuclear Energy A/B **16**(1962), 261.

[11] J. Frehaut, A. Bertin, and R. Bois. *Measurement of the U-235(n,2n) Cross Section between Threshold and 13 MeV*. Nuclear Science and Engineering **74**(1980), 29.

[12] K. Kobayashi, T. Hashimoto, and I. Kimura. *Measurement of Average Cross Section for U233(n,2n)U232 Reaction*. Journal of Nuclear Science and Technology, Tokyo **10**(1973), 668.

[13] D.S. Mather, P.F. Bampton, R.E. Coles, G. James, and P.J. Nind. *Measurement of (n,2n) Cross Sections for Incidend Energies between 6 and 14 MeV*. AWRE Aldermaston Reports No. 72/72 (1972).

[14] ChouYou-Pu. *Measurement of U-238(n,2n) Cross Sections*. Institute of Atomic Energy, Beijing Reports No. 77091 (1978).

[15] A.A. Filatenkov, S.V. Chuvaev, V.N. Aksenov, et al. *Systematic Measurement of Activation Cross Sections at Neutron Energies from 13.4 to 14.9 MeV*. Khlopin Radium Institute, Leningrad Reports No. 252 (1999).

[16] H. Karius, A. Ackermann, and W. Scobel. *The Pre-Equilibrium Contribution to the (n,2n) Reactions of Th-232 and U-238*. Journal of Physics **G5**(1979), 715.

[17] J.D. Knight, R.K. Smith, and B. Warren. *U238(n,2n)U237 Cross Section from 6 to 10 MeV*. Physical Review **112**(1958), 259.

[18] C. Konno, Y. Ikeda, K. Oishi, K. Kawade, H. Yamamoto, and H. Maekawa. *Activation Cross Section Measurements at Neutron Energy from 13.3 to 14.9 MeV*. JAERI Reports No. 1329 (1993).

[19] N.V. Kornilov, B.V. Zhuravlev, O.A. Salnikov, et al. *Measurement of Cross Sections for the U-238(n,2n) Reaction from 6.5 to 14.8 MeV*. Zentralinstitut für Kernforschung Rossendorf Reports No.410 (1980), 68.

[20] J.H. Landrum, R.J. Nagel, and M. Lindner. *(n,2n) Cross Sections for 238U and 237Np in the Region of 14 MeV*. Physical Review **C8**(1973), 1938.

[21] L.R. Veeser and E.D. Arthur. *Measurement of n-3n Cross Sections for U-235 and U-238*. International Conference on Neutron Physics and Nuclear Data, Harwell (1978), 1054.

[22] R.C. Haight, M. B. Chadwick, and D.J. Vieira. *Fundamental Nuclear Data for Pinning Down the Performance of Nuclear Weapons*. Los Alamos Science **30**(2006), 52.

[23] K.S. Krane. *Introductory Nuclear Physics*. John Wiley & Sons, Inc., 1988.

[24] A. Gilbert and A.G.W. Cameron. *A Composite Nuclear-Level Density Formula with Shell Corrections*. Canadian Journal of Physics **43**(1965), 1446.

[25] N. Bohr and J.A. Wheeler. *The Mechanism of Nuclear Fission*. Physical Review **56**(1939), 426.

[26] D.L. Hill and J.A. Wheeler. *Nuclear Constitution and the Interpretation of Fission Phenomena*. Physical Review **89**(1953), 1102.

[27] P.E. Hodgson, E. Gadioli, and E. Gadioli Erba. *Introductory Nuclear Physics*. Oxford: Clarendon Press, 1997.

[28] H. Feshbach, A. Kerman, and S. Koonin. *The Statistical Theory of Multi-Step Compound and Direct Reactions*. Annals of Physics **125**(1980), 429.

[29] N. Bohr. *Neutron Capture and Nuclear Constitution*. Nature **137**(1936), 344.

[30] W. Hauser and H. Feshbach. *The Inelastic Scattering of Neutrons*. Physical Review **87**(1952), 366.

[31] J.W. Tepel, H.M. Hofmann, and H.A. Weidenmüller. *Hauser-Feshbach Formulas for Medium and Strong Absorption*. Physical Letters **49B**(1974), 1.

[32] H.M. Hofmann, J. Richert, J.W. Tepel, and H.A. Weidenmüller. *Direct Reactions and Hauser-Feshbach Theory*. Annals of Physics **90**(1975), 403.

[33] H.M. Hofmann, T. Mertelmeier, M. Herman, and J.W. Tepel. *Hauser-Feshbach Calculations in the Presence of Weakly Absorbing Channels with Special Reference to the Elastic Enhancement Factor and the Factorization Assumption*. Zeitschrift für Physik A **297**(1980), 153.

[34] P.A. Moldauer. *Theory of Average Neutron Reaction Cross Sections in the Resonance Region*. Physical Review **123**(1961), 968.

[35] C.E. Porter and R.G. Thomas. *Fluctuations of Nuclear Reaction Widths*. Physical Review **104**(1956), 483.

[36] P.A. Moldauer. *Statistics and the Average Cross Section*. Nuclear Physics **A344**(1980), 185.

[37] J.J.M. Verbaarshot, H.A. Weidenmüller, and M.R. Zirnbauer. *Grassmann Integration in Stochastic Quantum Physics: The Case of Compound-Nucleus Scattering*. Physics Reports **129**(1985), 367.

[38] S. Hilaire, C. Lagrange, and A.J. Koning. *Comparisons Between Various Width Fluctuation Correction Factors for Compound Nucleus Reactions*. Annals of Physics **306**(2003), 209.

[39] J.J. Griffin. *Statistical Model of Intermediate Structure*. Physical Review Letters **17**(1966), 478.

[40] V.F. Weisskopf. *Radiative Transition Probabilities in Nuclei*. Physical Review **83**(1951), 1073.

[41] J. Kopecky and M. Uhl. *Test of Gamma-Ray Strength Functions in Nuclear Reaction Model Calculations*. Physical Review **C41**(1990), 1941.

[42] C.M. McCullagh, M.L. Stelts, and R.E. Chrien. *Dipole Radiative Strength Functions From Resonance Neutron Capture*. Physical Review **C23**(1981), 1394.

[43] D.M. Brink. Ph.D. thesis, Oxford University, 1955.

[44] P. Axel. *Electric Dipole Ground-State Transition Width Strength Function and 7-MeV Photon Interactions*. Physical Review **126**(1962), 671.

[45] S.G. Kadmenskij, V.P. Markushev, and V.I. Furmann. Soviet Journal of Nuclear Physics **37**(1983), 277.

[46] H. Olliver, T. Glasmacher, and A.E. Stuchbery. *Angular Distributions of γ Rays with Intermediate-Energy Beams*. Physical Review **C68**,(2003), 044312.

[47] M. Ferentz and N. Rosenzweig. *Table of F Coefficients*. Argonne National Laboratory Report ANL-5324 (1955).

[48] R.M. Diamond, E. Matthias, J.O. Newton, and F.S. Stephens. *Nuclear Alignment in Heavy-Ion Reactions*. Physical Review Letters **16**(1966), 1205.

[49] P.G. Young, E.D. Arthur, and M.B. Chadwick. *Comprehensive nuclear model calculations: Theory and use of the GNASH code*. Proceedings of the Workshop on Nuclear Reaction Data and Nuclear Reactors - Physics, Design, and Safety,Singapore (1999), 227.

[50] A.J. Koning, S. Hilaire, and M.C. Duijvestijn. *TALYS-1.0*. Proceedings of the International Conference on Nuclear Data for Science and Technology, Nice (2008).

[51] P. Cejnar and J. Kern. *Monte Carlo Analysis of $(\alpha, xn\gamma)$-Feeding Intensities in Cd Nuclei*. Nuclear Physics **A561**(1993), 317.

[52] P. Cejnar, S. Drissi, and J. Kern. *Calculation of the Spin Deorientation in $(\alpha, 2n\gamma)$ Reactions*. Nuclear Physics **A602**(1996), 225.

[53] J. Raynal. *ECIS96*. Proceedings of the Specialists' Meeting on the Nucleon Nucleus Optical Model up to 200 MeV, Bruyres-le-Chatel (1997), 159.

[54] C. Kalbach. *PRECO Program for Calculating Preequilibrium Particle Energy Spectra*. Centre d'Etudes Nucléaires de Saclay Rapport Interne DPh-N/BE/74/3 (1974).

[55] A.J. Koning and J.P. Delaroche. *Local and Global Nucleon Optical Models from 1 keV to 200 MeV*. Nuclear Physics **A713**(2003), 231.

[56] Reference Input Paramter Library, http://www-nds.iaea.or.at/RIPL-2/.

[57] S.A. Wender, C.E. Floyd, T.B. Clegg, and W.R. Wylie. *A High Efficiency Bunching System for Polarized Beams*. Nuclear Instruments and Methods **174**(1980), 341.

[58] W.T. Milner. *Double-Drift Beam Bunching Systems*. IEEE Transactions on Nuclear Science **NS-26**(1979), 1445.

[59] M. Drosg. *Unified Absolute Differential Cross Sections for Neutron Production by the Hydrogen Isotopes for Charged-Particle Energies between 6 and 17 MeV.* Nuclear Science and Engineering **67**(1978), 190.

[60] G.F. Knoll. *Radiation Detection and Measurement.* John Wiley & Sons, Inc., 2000.

[61] E.M. Pell. *Ion Drift in an n-p Junction.* Journal of Applied Physics, **31**(1960), 291.

[62] R.M. Keyser and T.W. Raudorf. *Germanium Radiation Detector Manufacturing: Process and Advances.* Nuclear Instruments and Methods in Physics Research **A286**(1990), 357.

[63] J. Theuerkauf, S. Esser, S. Krink, et al. Institute for Nuclear Physics, Cologne, 1993.

[64] T. Kibédi, T.W. Burrows, M.B. Trzhaskovskaya, P.M. Davidson, and C.W. Nestor, Jr. *Evaluation of theoretical conversion coefficients using BrIcc.* Nuclear Instruments and Methods in Physics Research **A589**(2008), 202.

[65] G.W. McKinney, J.W. Durkee, J.S. Hendricks, et al. *MCNPX Overview.* Proceedings of the 2006 HSSW, FNAL, IL, September 6-8, 2006.

[66] R.O.Nelson, N.Fotiades, M.Devlin, et al. *Cross-Section Standards for Neutron-Induced Gamma-Ray Production in the MeV Energy Range.* Conference on Nuclear Data for Science and Technology, Santa Fe **1** (2004), 838.

[67] T. Kawano, T. Ohsawa, M. Baba, and T. Nakagawa. *Effect of the Preequilibrium Process upon Fast Neutron Fission Spectra from* ^{238}U. Physical Review **C63**(2001), 034601.

[68] N. Fotiades, G.D. Johns, R.O. Nelson, et al. *Measurements and Calculations of* $^{238}U(n, xn\gamma)$ *Partial* γ*-Ray Cross Sections.* Physical Review **C69**(2004), 024601.

[69] D.K. Olsen, G.L. Morgan, and J.W. McConnell. *Measurement of 238-U(n,n'*γ*) Cross Section.* Conference on Nuclear Cross Sections for Technology, Knoxville (1979), 677.

[70] F. Voss, S. Cierjacks, D. Erbe, and G. Schmatz. *Gamma-Ray Production Cross Section in Inelastic neutron Scattering on U-238.* Kernforschungszentrum Karlsruhe Reports No. 2379 (1976).

[71] D.P. McNabb, J.A. Becker, D. Archer, et al. *Neutron-Induced Partial Gamma-Ray Cross-Section Measurements with GEANIE at LANSCE/WNR.* Symposium on Capture Gamma Ray Spectroscopy, Santa Fe, NM (1999), 384.

Biography

Anthony Lloyd Hutcheson

Personal

- Born in Augusta, Georgia on December 21, 1978

Education

- B.S. Physics, University of Georgia, Athens, GA, 2000
- A.M Physics, Duke University, Durham, NC, 2002

Publications

- *Measurement of the $^{241}Am(n, 2n)$ Reaction Cross Section from 7.6 MeV to 14.5 MeV*, A.P. Tonchev, C.T. Angell, M. Boswell, A.S. Crowell, B. Fallin, S. Hammond, C.R. Howell, A. Hutcheson, *et al.*, Phys. Rev. C **77**, 054610 (2008).
- *Pulsed and Monoenergetic Beams for Neutron Cross-Section Measurements Using Activation and Scattering Techniques at Triangle Universities Nuclear Laboratory*, A. Hutcheson, *et al.*, Nucl. Instrum. Methods Phys. B **261**, 369 (2007).
- *Low-Energy Photodisintegration of the Deuteron and Big-Bang Nucleosynthesis*, W. Tornow, N.G. Czakon, C.R. Howell, A. Hutcheson, *et al.*, Phys. Lett. B **574**, 8 (2003).
- *Analyzing Power for the Photodisintegration of the Deuteron between E_γ = 2.4 and 4.0 MeV*, W. Tornow, N.G. Czakon, C.R. Howell, A. Hutcheson, *et al.*, Mod. Phys. Lett. A **18**, 282 (2003).